UNIVERISTY OF CALIFORNIA

Los Angeles

Voltage Control of Magnetism in Nanoscale Artificial Multiferroics

A dissertation submitted in partial satisfaction of the requirements for the degree Doctor of Philosophy in Mechanical Engineering

by

Andres Cornel Chavez

2018

ABSTRACT OF THE DISSERTATION

Voltage Control of Magnetism in Nanoscale Artificial Multiferroics

by

Andres Cornel Chavez

Doctor of Philosophy in Mechanical Engineering

University of California, Los Angeles, 2018

Professor Gregory P. Carman, Chair

In this work, voltage control of magnetism in nanoscale artificial multiferroic structures was demonstrated through numerical simulation and measurement. The multiferroic nanostructures studied in this dissertation were modeled using two methods. The first approach relies solely on the Landau-Lifshitz-Gilbert (LLG) equation and incorporates the effects of strain through an effective magnetic field term that only accounts for spatially-uniform strain distributions. The second-modeling technique couples the LLG equation with the elastodynamics and piezoelectric constitutive equations by using an innovative weak-formulation. In contrast to the purely micromagnetic model, the coupled solution can account for nonuniform distributions of strain and magnetization within nanostructures. Here, these simulation tools were used to understand the effects of strain on magnetoelastic nanodots and to investigate new coupling phenomena. Regarding strain effects, the innovative magnetic measurement technique of Scanning Electron Microscopy with Polarization Analysis (SEMPA) was used to observe strain-induced changes from vortex to antiparallel bidomain states in submicron Ni disks. This data was then used to validate the modeling methods of this dissertation. Consequently, the SEMPA study represents an advancement in terms of magnetic characterization and experimental model validation. Following this work, a design that leverages shape anisotropy, magnetic dipole coupling, and strain effects to achieve transitions between artificial antiferromagnetic and artificial ferromagnetic ordering is presented. Specifically, the micromagnetic models demonstrate voltage-induced transitions between these artificial magnetic states, but there are discrepancies with the measured data. To account for this, geometric defects are added to the models, thus dramatically

improving the correlation between experiment and simulation. Importantly, this specific study demonstrates novel device behavior and introduces a modeling method to account for fabrication defects. Next, full 360° deterministic magnetization switching was numerically demonstrated with a design that consists of three dipole-coupled magnetoelastic ellipses patterned on a piezoelectric substrate. In comparison to other deterministic magnetization switching methods, this design reduces the complexity of electrical control and is more easily fabricated. Lastly, a novel design integrating multiferroics with artificial spin ices (ASI) is presented and used to provide the first numerical demonstration of local voltage-control of magnetic monopoles.

The dissertation of Andres Cornel Chavez is approved.

Eric Pei-Yu Chiou

Robert N. Candler

Christopher S. Lynch

Gregory P. Carman, Committee Chair

University of California, Los Angeles

2018

To my mom, chuy, nana, tía aya, the sisters I never asked for, Lucas, the rest of my family, Dr. Youssef, el profe, and porky. From you I always found motivation, inspiration, and the strength to persevere.

Contents

List of Figures

List of Tables

ACKNOWLEDGMENTS

I would first like to thank my family. To my mother, you have served as an inspiration. Despite your humble start as an immigrant field worker, you found a way to get a college education and become a teacher and from you, I learned how to never give up and to never let anyone push me around. I am deeply thankful for all the sacrifices you made and for all the support and love you have given me. To Anne and Erin, you have always been great sources of support when life tried to knock me out. You've always helped me keep things in perspective and without you, I could not have survived through this final stretch. To tía aya and Chuy, there was never a dull moment spending time with you and that type of stress relief is invaluable. To porky, you always saw connections that nobody else did, you created things that I could never fathom, and by being around you some of that creative and innovative spirit rubbed off on me. For that I am forever thankful. To Dr. Youssef, thank you for believing in me and for all the opportunities you gave me. I would not have reached a PhD program without your help. To el Profe, gracias por enseñarme cómo amar a las mathemáticas con todo mi corazón. To Alex, thank you for the love and patience.

I would also like to thank the great friends I made in grad school. To Auni, I can honestly say I would not have made it through this without you. All the falling, the mispoken sentences, headaches, cupcakes, roach flavored tiramisu, the bad life advice, and unforgettable outings made grad school so much fun (believe me for once). To Tony, you never let me get any work done because we either ended up in the hospital or talking about baseball, F1, the philosophy of time, politics, or (the list goes on since you never stopped talking). All jokes A-side, you were the one person I could come to for help with technical matters. I am extremely grateful for all your help. Also, it was always a blast hanging out with you. To Devin, thank you for all the political discussions and for being my coffee buddy. Both were highlights of my day and kept me motivated to push through. To Yu-Ching, thank you for being you (I think you know how much I appreciate that).

To my adviser, Professor Greg Carman, thank you for challenging me every Friday, for your understanding during personal issues I faced, and for teaching me that I belonged at UCLA. Further, I would like to thank the members of my committee, Professors Chris Lynch, Rob Candler, and Eric Chiou for their help and willingness to review my work.

I would like to thank all my labmates at the AML including the retired crew that held Malty-ferroic meetings. It was an absolute pleasure to work with all of you. Further, I would like to thank all the individuals that I have had the great pleasure to collaborate with. From you I learned what it takes to do challenging and meaningful research.

Lastly, this work was supported in part by FAME, one of six centers of STARnet, a Semiconductor Research Corporation program sponsored by MARCO and DARPA. This work was also supported by NSF Nanosystems Engineering Research Center for Translational Applications of Nanoscale Multiferroic Systems (TANMS) Cooperative Agreement Award (No. EEC-1160504).

VITA

Education:

2012 M.S. - Mechanical Engineering
California State University, Northridge

2010 B.S. - Mathematics and Mechanical Engineering
California State University, Northridge

Publications

The work presented in this thesis is based on the following publications and conference presentations

1. A.C. Chavez, A. Barra, and G.P. Carman. "Voltage Control of Magnetic Monopoles in Artificial Spin Ice." Journal of Physics D: Applied Physics 51.23 (2018): 234001.

2. M. Balinskiy, A.C. Chavez., A. Barra, H. Chiang, G.P. Carman, and A. Khitun. "Magnetoelectric Spin Wave Modulator Based on Synthetic Multiferroic Structure." Scientific Reports. Manuscript (2018).

3. D.B. Gopman, P.J. Chen, J.W. Lau, A.C. Chavez, G.P. Carman, P. Finkel, M. Staruch, and R.D. Shull. "Large interfacial magnetostriction in (Co/Ni)4/Pb(Mg1/3Nb2/3)O3-PbTiO3 multiferroic heterostructures." ACS Applied Materials & Interfaces. Manuscript (2018).

4. A. Kundu, A.C. Chavez, S.M. Keller, G.P. Carman, and C.S. Lynch. "360 Degree Deterministic Magnetization Rotation in a Three-Ellipse Magnetoelectric Heterostructure."

Journal of Applied Physics 123.10 (2018): 104105.

5. K.P. Mohanchandra, T. Lee, A.C. Chavez, S.V. Prikhodko, and G.P. Carman. ”Polycrystalline Terfenol-D thin films grown at CMOS compatible temperature.” AIP Advances 8.5 (2018): 056404.

6. Z. Xiao, K.P. Mohanchandra, R. Lo Conte, C.T. Karaba, J.D. Schneider, A.C. Chavez, S. Tiwari, H. Sohn, M.E. Nowakowski, A. Scholl, S.H. Tolbert, J. Bokor, G.P. Carman, and R.N. Candler. ”Enhanced magnetoelectric coupling in a composite multiferroic system via interposing a thin film polymer.” AIP Advances 8.5 (2018): 055907.

7. A.C. Chavez, W.Y. Sun, J. Atulasimha, K.L. Wang, and G.P. Carman. ”Voltage induced artificial ferromagnetic-antiferromagnetic ordering in synthetic multiferroics.” Journal of Applied Physics 122.22 (2017): 224102.

8. I. Gilbert, A.C. Chavez, D.T. Pierce, J. Unguris, W.Y. Sun, C.Y. Liang, and G.P. Carman. “Magnetic Microscopy and Simulation of Strain-Mediated Control of Magnetization in PMN-PT/Ni Nanostructures.” Applied Physics Letters 109.16 (2016): 162404.

9. M. Salehi-Fashami, M. Al-Rashid, W.Y. Sun, P.K. Nordeen, S. Bandyopadhyay, A.C. Chavez, G.P. Carman, and J. Atulasimha. ”Binary information propagation in circular magnetic nanodot arrays using strain induced magnetic anisotropy.” Nanotechnology 27.43 (2016): 43LT01.

1 Introduction

1.1 Background

In 2013 IBM stated that 2.5 exabytes (10^{18} bytes) of data were produced every day and that 90% of the world's data at that time had been created within the previous two years [1, 2]. Projections by leading data analysts suggest that 1.7 MB of new information will be generated every second for every person on the planet by 2020 resulting in an astounding global data accumulation of 44 zettabytes (10^{21} bytes) [3]. Successfully addressing the data storage and data analysis challenges posed by this immense amount of information requires significant increases in data storage capacity and computing power. To meet these growing needs, one avenue manufacturers have pursued is increasing microprocessor power density (i.e., device density) by reducing the size of contemporary CMOS elements. Although this scaling of CMOS transistors has been successful, a growing consensus is that physical limitations will soon be reached when the smallest feature sizes are in the range of 14 nm to 22 nm [4]. At these length scales the power density is nearly 1000 W/cm^2 which is equal to that of a rocket nozzle [5]. Since this scaling paradigm leads to intractable heating problems, alternatives to CMOS have been sought.

Specifically, for next-generation memory and logic devices, the following characteristics are desired: 1) scalability, 2) high-speed, 3) non-volatility, 4) low-power, and 5) random-accessibility [6]. Scalability refers to the capability of reducing device dimensions (i.e., increasing device density) while maintaining acceptable performance. High-speed is desired in terms of read and write operations. Non-volatility signifies the property of a device to store information even when power is removed. The designation of low-power is regarding devices requiring low read and write energies. Random-access is the ability to access an arbitrary element of a sequence in equal time. Magnetic memory/logic devices, which rely on the spin angular momentum of the electron to encode information, are one of the most promising pathways to realize hardware

that possess the five desired properties already discussed.

In this space, one of the most prominent architectures is Magnetoresistive Random-Access Memory (MRAM). The main elements of MRAM are magnetic tunnel junctions (MTJ's) which advantageously offer the possibility to build non-volatile storage elements that can also complete logic operations and integrate with contemporary CMOS circuits [7]. For simplicity, here we will first consider the cornerstone of any MTJ. Namely, the basic trilayer structure shown in Figure 1.1. The simplified device consists of an insulating oxide layer sandwiched between two ferromagnetic layers. The oxide serves as a tunneling barrier and we assume that the bottom magnetic layer is fixed by some intrinsic magnetic anisotropy. Note, that in practice, the magnetization of the fixed (or reference) layer is pinned in a certain direction by exchange coupling to a synthetic antiferromagnetic layer. The resistance state is determined by the magnetic orientation of the free layer. Specifically, a low resistance state is observed when the MTJ is in the parallel configuration of Figure 1.1 and a high resistance state occurs for an antiparallel configuration. This can be understood by recalling the following arguments: 1) the tunneling current is proportional to the product of the electron density of states (DOS) at the Fermi level; 2) the ground-state energy bands, of ferromagnets, near the Fermi level are shifted in energy and yield separate majority and minority bands for electrons with opposite spins; and 3) assuming spin conservation for tunneling electrons, there are two parallel currents of opposite spin (i.e., spin-left or spin-right in this case) [8]. In addition to being non-volatile, MTJ's are scalable, can be read/written at high-speed, are randomly-accessible, and can be read/written at energies lower than typical CMOS devices.

The main technological challenge impeding widespread adoption of MTJ's is the writing method. Regarding this issue, researchers have focused considerable effort on leveraging spin transfer torque (STT) to control (i.e., write) the orientation of the free layer magnetization in an MTJ [9]. This can be accomplished by passing a current through an MTJ that has ferromagnetic layers with unequal thicknesses. When electrons pass through the thick fixed layer, their spins align with the layer's magnetization (i.e., become spin polarized). These electrons then pass

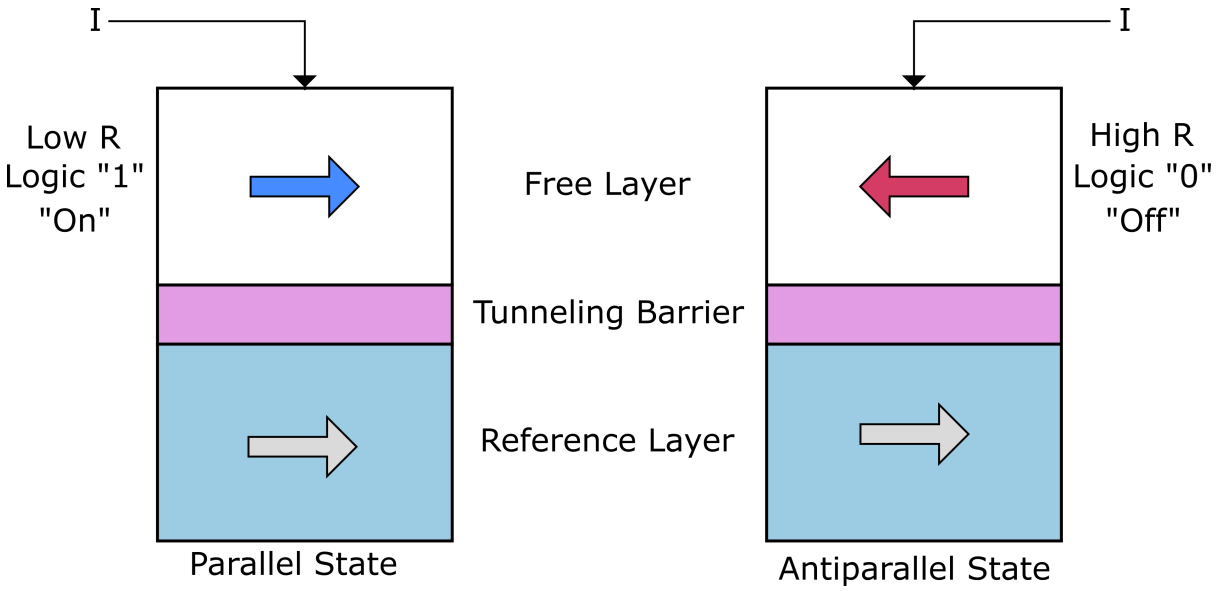

Figure 1.1: Schematic of magnetic tunnel junction stack in a low resistance (left) and high resistance (right) state.

through the thin magnetic layer becoming repolarized within a small transition region. As this occurs, the electrons exert a torque on the magnetization of the thin layer and if the torque is large enough, switching occurs. Otherwise, if the torque is lower than the critical value, the layer magnetization begins to precess around the applied bias magnetic field [7].

Since STT was first introduced, independently, by Slonczewski [10] and Berger [11], the method has been used to successfully switch magnetization in nanodevices [12, 13]. For example, STT switching in magnetic nanopillars was first experimentally observed in 2000 [14]. Another key milestone was reached, when the first demonstration of STT switching in an Al_2O_3 MTJ was achieved in 2004 [15, 16]. Then other major contributions were made when STT was used to switch the magnetization in MgO based tunnel junctions with TMR $>$ 150% [17–19]. Although STT has been widely studied and shown to be a viable writing mechanism for MRAM, its proliferation has been limited by the large current densities needed to achieve switching [13]. Furthermore, the write energies associated with STT-MRAM are much larger when compared to other write mechanisms such as strain-mediated methods [20].

The strain-mediated approach to control magnetism involves multiferroic composites which

couple piezoelectric and magnetoelastic phases. Discovered in 1880 by Pierre and Jacque Curie, piezoelectricity is a property of some materials to develop charge on their surface in response to applied stresses. Alternatively, if an electric field is applied to the piezoelectric material, then mechanical deformation occurs. The electrical response to mechanical stimuli is denoted as the piezoelectric effect while the mechanical response to electrical input is the converse piezoelectric effect. Analogously, there are magnetic materials, known as magnetoelastic materials, which exhibit changes in magnetization when stress is applied, or which mechanically deform in the presence of magnetic fields. Similarly, the magnetic response to mechanical stimuli is denoted as the magnetoelastic effect while the mechanical response to magnetic input is the converse magnetoelastic response. The benefit of multiferroic composites is that voltages can be used to control the magnetic properties of the system in comparison to traditional techniques which require electrical current. The advantage is clarified when considering the previous discussion regarding the insurmountable heating problems caused by scaling CMOS devices below 20 nm. This intrinsic low energy capability suggests multiferroic composites as a solution for next-generation memory devices that overcome the limitations of CMOS.

Pioneering experimental work by Ryu et al. [21] showing strong coupling between the magnetic and electrical properties of Terfenol-D/PZT/Terfenol-D laminate multiferroic composites represented a critical milestone that initiated a resurgence of interest in multiferroics. In their study, a direct magnetoelectric (DME) coupling coefficient of 1500 mV/cm-Oe was found demonstrating orders of magnitude larger transduction of magnetic energy to electrically energy than previously observed [21, 22]. Following this work, numerous studies investigated magnetoelectric coupling in various geometries and combinations of piezoelectric and magnetoelastic materials [23–27]. For example, Li et al. [28] demonstrated alternatives to laminate geometries by measuring a 1900 mV/cm-Oe DME coefficient in a CFO/PZT disk-ring composite. In addition to these studies, significant focus was placed on understanding the converse magnetoelectric (CME) coupling of multiferroic composites [29–33]. Jia et al. [34] was one of the first to study the CME effect in a PMN-PT/Terfenol-D/PMN-PT laminate composite and reported a coupling coefficient of 450 mG/V. A major advancement followed when Hockel et

al. [35] measured a 4700 mG/V CME coefficient in a PZT/Terfenol-D/PZT laminate composite. Building on these fundamental studies, work began on understanding the application of multiferroics to sensor, transformer, and microwave-frequency technologies began [23, 24, 36–41]. Together, these fundamental studies and bulk applications set a precedent for the potential of using multiferroic composites to control magnetism in the context of nanoscale devices.

Some of the first work to explore the potential for multiferroics in nanoscale devices, focused on studying strain-mediated effects in ferromagnetic thin films [42, 43]. For example, seminal work by Weiler et al. [44] demonstrated 90° magnetization rotation in Ni thin films deposited on piezoelectric actuators. Following this, Brintlinger et al. [45] provided experimental and numerical predictions, using OOMMF and assuming constant strain within the structure, to show reversible switching in FeGa/BTO thin films. This constant strain assumption was shown to work well in several studies that measured and modeled the coupling in thin film piezoelectric/magnetoelastic heterostructures [46–48]. However, a significant breakthrough was provided by Bur et al. [49] when modeling results incorporating nonuniform strain distributions provided better predictions of strain-induced coercive field changes in nanopatterned Ni bars. Along with this work, several other studies provided further evidence for the need of modeling techniques that accounted for nonuniformities in strain [50–53].

In an effort to overcome the shortcomings of previous modeling techniques, researchers began exploring methods to couple the governing mechanical and micromagnetic equations [54–57]. The two leading methods for accomplishing this goal involved either phase-field techniques or weak formulations to solve the governing system of equations [58–60]. In this space, a major contribution by Zhang and Chen [58] leveraged a Gauss-Seidel approach to solve the coupled micromagnetics and phase-field microelasticity equations. In contrast to the phase-field theory, Liang et al. [60–63] introduced a breakthrough modeling technique through a series of seminal papers that use an innovative weak-formulation to couple the governing micromagnetics, elastodynamics, and piezoelectric constitutive equations. In their work, the fully-coupled model was used to investigate strain-induced magnetization rotation in nanoscale magnetoe-

lastic structures such as ellipses and rings. In addition to this modeling effort, a considerable amount of experimental work was conducted [25, 64–66]. For example, Cui et al. [67–69] introduced the concept of using patterned electrodes to apply localized strain and demonstrated magnetization rotation in micron sized magnetoelastic disks and rings. Another example refers to a study in which Sohn et al. [70] were able to experimentally verify, with MFM, the fully-coupled model predictions of multistep strain-mediated magnetization rotation in Ni disks. These foundational studies have provided important insights for understanding how nanoscale magnetism can be controlled using multiferroic composites. However, there is still a need for more experimental validation and improvement in magnetic measurement techniques because the field is continuing to grow rapidly.

Along these lines, numerous studies investigating coupling phenomena and strain-mediated effects in multi-dot arrays have been conducted. Motivation for much of this work stems from the potential application of multiferroics to MRAM. In this setting, dipole coupling between adjacent magnetoelastic nanodots is leveraged to store or transmit information. Roy et al. has shown analytically that 180° magnetization switching in elliptical elements can be achieved using strain with energy dissipation on the order of tens of attojoules [51, 71–73]. Later work successfully illustrated the concept of integrating Bennett clocking with strain-mediated designs to propagate information and perform logic operations along 1D chains of nanodots [74–76]. In these studies, arrays consisting of chains of magnetoelastic nanodots are patterned on piezoelectric substrates where control of the nanomagnets' magnetization is accomplished by leveraging shape anisotropy, dipole coupling, and strain-mediated effects. Despite the substantial work conducted investigating the application of dipole-coupled nanomagnets for memory applications, there is still ample space to explore new architectures by leveraging modern simulation tools and MEMS fabrication capabilities.

To summarize, the advent of big data will push modern data storage and computing capabilities to their limits. Consequently, this has prompted efforts to develop next-generation memory and logic devices that would overcome the scaling issues of contemporary CMOS circuits.

MRAM has been investigated as a potential solution, but its widespread use has been hindered because the STT write mechanism extensively used in devices has comparatively low energy efficiency. As a result, significant research interest has focused on controlling magnetism in nanoscale structures using strain-mediated multiferroic composites. Although sophisticated modeling tools and experimental capabilities have been developed for studying the multiferroic structures, there is a need for more experimental validation and improved measurement techniques. Moreover, even though many device architectures such as ring structures or arrays of dipole coupled nanomagnets have been studied, there are still many new combinations of materials and geometries that deserve investigation. In this regard, sophisticated modeling tools and MEMS fabrication capabilities can be leveraged to discover novel device functionality and magnetic-coupling phenomena. The work in this dissertation provides advancements which improve magnetic measurement capabilities that add to the experimental validation of current simulation tools. Additional contributions regard novel device functionality and coupling phenomena. Specifically, an innovative characterization technique will be introduced, and magnetization measurements of submicron Ni disks will be used to validate models of multiferroic devices. Additionally, the combined effects of magnetic shape anisotropy, magnetic dipole coupling, and strain will be studied in the context of artificial antiferromagnetic ordering, deterministic magnetization switching, and control of magnetic monopoles.

1.2 Dissertation Overview

In this dissertation, the ability of strain to control the magnetic state of nanoscale structures patterned on ferroelectric substrates is investigated both numerically and experimentally. First, the two modeling techniques used in this work are presented in Chapter 2. Specifically, the micromagnetics theory is provided along with the relevant physical assumptions and procedure for incorporating strain into the model. Subsequently, a weak formulation that couples the governing micromagnetics, elastodynamics, and piezoelectric constitutive equations is outlined for implementation in an iterative finite element code. In Chapter 3, Scanning Electron Microscopy

with Polarization Analysis (SEMPA) is used to measure the effects of strain on the magnetic states of submicron Ni disks. Data collected from this innovative measurement technique was then used to validate the two simulation methods of this dissertation. In Chapter 4, dipole coupling between magnetoelastic nanodots is leveraged to achieve voltage-induced transitions between artificial antiferromagnetic and artificial ferromagnetic ordering. This functionality is demonstrated through micromagnetic simulations of three nanodot arrays. Additionally, magnetization measurements of the fabricated device are shown and a secondary model incorporating geometric defects is developed to account for discrepancies between simulation and experiment. In Chapter 5, a design to achieve 360° deterministic magnetization switching consisting of three dipole-coupled ellipses is introduced. The device functionality is modeled using the techniques of Chapter 2 and a discussion of the advantages of the fully-coupled model over the purely micromagnetics formulation is given. In Chapter 6, a novel design integrating multiferroics with artificial spin ices (ASI) is used to locally control magnetic monopoles. This control method is numerically demonstrated in a Kagome lattice ASI consisting of elliptical magnetoelastic elements. The device performance and energy requirements are also studied. Lastly, a summary of the work presented in this dissertation is given in Chapter 7.

1.3 Chapter References

[1] *2.5 quintillion bytes of data created every day. how does cpg & retail manage it? - ibm consumer products industry blog*, https://www.ibm.com/blogs/insights-on-business/consumer-products/2-5-quintillion-bytes-of-data-created-every-day-how-does-cpg-retail-manage-it/.

[2] S. Sagiroglu and D. Sinanc, "Big data: a review", in Collaboration technologies and systems (cts), 2013 international conference on (IEEE, 2013), pp. 42–47.

[3] *152,000 smart devices every minute in 2025: idc outlines the future of smart things*, https://www.forbes.com/sites/michaelkanellos/2016/03/03/152000-smart-devices-every-minute-in-2025-idc-outlines-the-future-of-smart-things/28652c44b63e.

[4] N. Z. Haron and S. Hamdioui, "Why is cmos scaling coming to an end?", in Design and test workshop, 2008. idt 2008. 3rd international (IEEE, 2008), pp. 98–103.

[5] M. Lundstrom, "Moore's law forever?", Science **299**, 210 (2003).

[6] H. Li and Y. Chen, "An overview of non-volatile memory technology and the implication for tools and architectures", in Proceedings of the conference on design, automation and test in europe (European Design and Automation Association, 2009), pp. 731–736.

[7] A. Makarov, T. Windbacher, V. Sverdlov, and S. Selberherr, "Cmos-compatible spintronic devices: a review", Semiconductor Science and Technology **31**, 113006 (2016).

[8] W. J. Gallagher and S. S. Parkin, "Development of the magnetic tunnel junction mram at ibm: from first junctions to a 16-mb mram demonstrator chip", IBM Journal of Research and Development **50**, 5 (2006).

[9] F. Matsukura, Y. Tokura, and H. Ohno, "Control of magnetism by electric fields", Nature nanotechnology **10**, 209 (2015).

[10] J. C. Slonczewski, “Current-driven excitation of magnetic multilayers”, Journal of Magnetism and Magnetic Materials **159**, L1 (1996).

[11] L. Berger, “Emission of spin waves by a magnetic multilayer traversed by a current”, Physical Review B **54**, 9353 (1996).

[12] S. Bhatti, R. Sbiaa, A. Hirohata, H. Ohno, S. Fukami, and S. Piramanayagam, “Spintronics based random access memory: a review”, Materials Today (2017).

[13] Y. Huai, “Spin-transfer torque mram (stt-mram): challenges and prospects”, AAPPS bulletin **18**, 33 (2008).

[14] J. Katine, F. Albert, R. Buhrman, E. Myers, and D. Ralph, “Current-driven magnetization reversal and spin-wave excitations in co/cu/co pillars”, Physical review letters **84**, 3149 (2000).

[15] Y. Huai, F. Albert, P. Nguyen, M. Pakala, and T. Valet, “Observation of spin-transfer switching in deep submicron-sized and low-resistance magnetic tunnel junctions”, Applied Physics Letters **84**, 3118 (2004).

[16] G. Fuchs, N. Emley, I. Krivorotov, P. Braganca, E. Ryan, S. Kiselev, J. Sankey, D. Ralph, R. Buhrman, and J. Katine, “Spin-transfer effects in nanoscale magnetic tunnel junctions”, Applied Physics Letters **85**, 1205 (2004).

[17] Z. Diao, D. Apalkov, M. Pakala, Y. Ding, A. Panchula, and Y. Huai, “Spin transfer switching and spin polarization in magnetic tunnel junctions with mgo and alo x barriers”, Applied Physics Letters **87**, 232502 (2005).

[18] H. Kubota, A. Fukushima, Y. Ootani, S. Yuasa, K. Ando, H. Maehara, K. Tsunekawa, D. D. Djayaprawira, N. Watanabe, and Y. Suzuki, “Evaluation of spin-transfer switching in cofeb/mgo/cofeb magnetic tunnel junctions”, Japanese Journal of Applied Physics **44**, L1237 (2005).

[19] Y. Huai, D. Apalkov, Z. Diao, Y. Ding, A. Panchula, M. Pakala, L.-C. Wang, and E. Chen, "Structure, materials and shape optimization of magnetic tunnel junction devices: spin-transfer switching current reduction for future magnetoresistive random access memory application", Japanese journal of applied physics **45**, 3835 (2006).

[20] J.-P. Wang, "Spintronics and promising applications", IEEE Magnetics Summer School, 39 (2015).

[21] J. Ryu, S. Priya, A. V. Carazo, K. Uchino, and H.-E. Kim, "Effect of the magnetostrictive layer on magnetoelectric properties in lead zirconate titanate/terfenol-d laminate composites", Journal of the American Ceramic Society **84**, 2905 (2001).

[22] C.-W. Nan, M. Bichurin, S. Dong, D. Viehland, and G. Srinivasan, "Multiferroic magnetoelectric composites: historical perspective, status, and future directions", Journal of Applied Physics **103**, 1 (2008).

[23] S. Dong, J. Li, and D. Viehland, "Voltage gain effect in a ring-type magnetoelectric laminate", Applied physics letters **84**, 4188 (2004).

[24] S. Dong, J.-F. Li, and D. Viehland, "Circumferentially magnetized and circumferentially polarized magnetostrictive/piezoelectric laminated rings", Journal of applied physics **96**, 3382 (2004).

[25] J. L. Hockel, A. Bur, T. Wu, K. P. Wetzlar, and G. P. Carman, "Electric field induced magnetization rotation in patterned ni ring/pb (mg1/3nb2/3) o3](1- 0.32)-[pbtio3] 0.32 heterostructures", Applied Physics Letters **100**, 022401 (2012).

[26] V. Mathe, G. Srinivasan, and A. Balbashov, "Magnetoelectric effects in bilayers of lead zirconate titanate and single crystal hexaferrites", Applied Physics Letters **92**, 122505 (2008).

[27] J. Gao, J. Das, Z. Xing, J. Li, and D. Viehland, "Comparison of noise floor and sensitivity for different magnetoelectric laminates", Journal of Applied Physics **108**, 084509 (2010).

[28] L. Li, Y. Q. Lin, and X. M. Chen, "Cofe 2 o 4/ pb (zr 052 ti 0.48) o 3 disk-ring magnetoelectric composite structures", Journal of Applied Physics **102**, 064103 (2007).

[29] G. Srinivasan, "Magnetoelectric composites", Annual Review of Materials Research **40**, 153 (2010).

[30] J. Zhai, Z. Xing, S. Dong, J. Li, and D. Viehland, "Magnetoelectric laminate composites: an overview", Journal of the American Ceramic Society **91**, 351 (2008).

[31] T. Wu, T.-K. Chung, C.-M. Chang, S. Keller, and G. P. Carman, "Influence of electric voltage bias on converse magnetoelectric coefficient in piezofiber/metglas bilayer laminate composites", Journal of applied physics **106**, 054114 (2009).

[32] C.-M. Chang and G. P. Carman, "Modeling shear lag and demagnetization effects in magneto-electric laminate composites", Physical review B **76**, 134116 (2007).

[33] A. C. Chavez, M. Lopez, and G. Youssef, "Converse magneto-electric coefficient of concentric multiferroic composite ring", Journal of Applied Physics **119**, 233905 (2016).

[34] Y. Jia, S. W. Or, H. L. W. Chan, X. Zhao, and H. Luo, "Converse magnetoelectric effect in laminated composites of pmn–pt single crystal and terfenol-d alloy", Applied physics letters **88**, 242902 (2006).

[35] J. L. Hockel, T. Wu, and G. P. Carman, "Voltage bias influence on the converse magnetoelectric effect of pzt/terfenol-d/pzt laminates", Journal of Applied Physics **109**, 064106 (2011).

[36] S. Dong, J.-F. Li, and D. Viehland, "Vortex magnetic field sensor based on ring-type magnetoelectric laminate", Applied physics letters **85**, 2307 (2004).

[37] S. Dong, J.-F. Li, D. Viehland, J. Cheng, and L. Cross, "A strong magnetoelectric voltage gain effect in magnetostrictive-piezoelectric composite", Applied Physics Letters **85**, 3534 (2004).

[38] J. Zhai, J. Li, S. Dong, D. Viehland, and M. I. Bichurin, "A quasi (unidirectional) tellegen gyrator", Journal of applied physics **100**, 124509 (2006).

[39] M. Bichurin, V. Petrov, Y. V. Kiliba, and G. Srinivasan, "Magnetic and magnetoelectric susceptibilities of a ferroelectric/ferromagnetic composite at microwave frequencies", Physical Review B **66**, 134404 (2002).

[40] Z. Huang, "Theoretical modeling on the magnetization by electric field through product property", Journal of applied physics **100**, 114104 (2006).

[41] Y. K. Fetisov and G. Srinivasan, "Electric field tuning characteristics of a ferrite-piezoelectric microwave resonator", Applied physics letters **88**, 143503 (2006).

[42] T.-K. Chung, S. Keller, and G. P. Carman, "Electric-field-induced reversible magnetic single-domain evolution in a magnetoelectric thin film", Applied Physics Letters **94**, 132501 (2009).

[43] Y. Chen, T. Fitchorov, C. Vittoria, and V. Harris, "Electrically controlled magnetization switching in a multiferroic heterostructure", Applied Physics Letters **97**, 052502 (2010).

[44] M. Weiler, A. Brandlmaier, S. Geprägs, M. Althammer, M. Opel, C. Bihler, H. Huebl, M. Brandt, R. Gross, and S. Goennenwein, "Voltage controlled inversion of magnetic anisotropy in a ferromagnetic thin film at room temperature", New Journal of Physics **11**, 013021 (2009).

[45] T. Brintlinger, S.-H. Lim, K. H. Baloch, P. Alexander, Y. Qi, J. Barry, J. Melngailis, L. Salamanca-Riba, I. Takeuchi, and J. Cumings, "In situ observation of reversible nanomagnetic switching induced by electric fields", Nano letters **10**, 1219 (2010).

[46] W. Eerenstein, N. Mathur, and J. F. Scott, "Multiferroic and magnetoelectric materials", nature **442**, 759 (2006).

[47] T. H. Lahtinen, K. J. Franke, and S. Van Dijken, "Electric-field control of magnetic domain wall motion and local magnetization reversal", Scientific reports **2**, 258 (2012).

[48] D. Z. Bai, J.-G. Zhu, W. Yu, and J. A. Bain, "Micromagnetic simulation of effect of stress-induced anisotropy in soft magnetic thin films", Journal of applied physics **95**, 6864 (2004).

[49] A. Bur, T. Wu, J. Hockel, C.-J. Hsu, H. K. Kim, T.-K. Chung, K. Wong, K. L. Wang, and G. P. Carman, "Strain-induced magnetization change in patterned ferromagnetic nickel nanostructures", Journal of Applied Physics **109**, 123903 (2011).

[50] J.-M. Hu, Z. Li, L.-Q. Chen, and C.-W. Nan, "High-density magnetoresistive random access memory operating at ultralow voltage at room temperature", Nature communications **2**, 553 (2011).

[51] K. Roy, S. Bandyopadhyay, and J. Atulasimha, "Switching dynamics of a magnetostrictive single-domain nanomagnet subjected to stress", Physical Review B **83**, 224412 (2011).

[52] J. Dean, M. Bryan, G. Hrkac, A. Goncharov, C. Freeman, M. Bashir, T. Schrefl, and D. Allwood, "The incorporation of the cauchy stress matrix tensor in micromagnetic simulations", Journal of Applied Physics **108**, 073903 (2010).

[53] J. Atulasimha and S. Bandyopadhyay, "Bennett clocking of nanomagnetic logic using multiferroic single-domain nanomagnets", Applied Physics Letters **97**, 173105 (2010).

[54] G. Carbou, M. Efendiev, and P. Fabrie, "Global weak solutions for the landau–lifschitz equation with magnetostriction", Mathematical Methods in the Applied Sciences **34**, 1274 (2011).

[55] Y. Shu, M. Lin, and K. Wu, "Micromagnetic modeling of magnetostrictive materials under intrinsic stress", Mechanics of Materials **36**, 975 (2004).

[56] C. Miehe and G. Ethiraj, "A geometrically consistent incremental variational formulation for phase field models in micromagnetics", Computer Methods in Applied Mechanics and Engineering **245**, 331 (2012).

[57] H. Szambolics, J.-C. Toussaint, L. Buda-Prejbeanu, F. Alouges, E. Kritsikis, and O. Fruchart, "Innovative weak formulation for the landau–lifshitz–gilbert equations", IEEE Transactions on Magnetics **44**, 3153 (2008).

[58] J. Zhang and L. Chen, "Phase-field microelasticity theory and micromagnetic simulations of domain structures in giant magnetostrictive materials", Acta Materialia **53**, 2845 (2005).

[59] I. Cimrák and M. Slodička, "An iterative approximation scheme for the landau–lifshitz–gilbert equation", Journal of computational and applied mathematics **169**, 17 (2004).

[60] C.-Y. Liang, S. M. Keller, A. E. Sepulveda, A. Bur, W.-Y. Sun, K. Wetzlar, and G. P. Carman, "Modeling of magnetoelastic nanostructures with a fully coupled mechanical-micromagnetic model", Nanotechnology **25**, 435701 (2014).

[61] C.-Y. Liang, S. M. Keller, A. E. Sepulveda, W.-Y. Sun, J. Cui, C. S. Lynch, and G. P. Carman, "Electrical control of a single magnetoelastic domain structure on a clamped piezoelectric thin film—analysis", Journal of Applied Physics **116**, 123909 (2014).

[62] C.-Y. Liang, A. E. Sepulveda, D. Hoff, S. M. Keller, and G. P. Carman, "Strain-mediated deterministic control of 360 domain wall motion in magnetoelastic nanorings", Journal of Applied Physics **118**, 174101 (2015).

[63] C.-Y. Liang, A. Sepulveda, S. Keller, and G. P. Carman, "Deterministic switching of a magnetoelastic single-domain nano-ellipse using bending", Journal of Applied Physics **119**, 113903 (2016).

[64] L. Martin, S. Crane, Y. Chu, M. Holcomb, M. Gajek, M. Huijben, C. Yang, N. Balke, and R. Ramesh, "Multiferroics and magnetoelectrics: thin films and nanostructures", Journal of Physics: Condensed Matter **20**, 434220 (2008).

[65] H. K. Kim, L. T. Schelhas, S. Keller, J. L. Hockel, S. H. Tolbert, and G. P. Carman, "Magnetoelectric control of superparamagnetism", Nano letters **13**, 884 (2013).

[66] M. Buzzi, R. Chopdekar, J. Hockel, A. Bur, T. Wu, N. Pilet, P. Warnicke, G. Carman, L. Heyderman, and F. Nolting, "Single domain spin manipulation by electric fields in strain coupled artificial multiferroic nanostructures", Physical review letters **111**, 027204 (2013).

[67] J. Cui, J. L. Hockel, P. K. Nordeen, D. M. Pisani, C.-y. Liang, G. P. Carman, and C. S. Lynch, "A method to control magnetism in individual strain-mediated magnetoelectric islands", Applied Physics Letters **103**, 232905 (2013).

[68] J. Cui, J. L. Hockel, P. K. Nordeen, D. M. Pisani, G. P. Carman, and C. S. Lynch, "Giant electric-field-induced magnetic anisotropy reorientation with patterned electrodes on a ni thin film/lead zirconate titanate heterostructure", Journal of Applied Physics **115**, 17C711 (2014).

[69] J. Cui, C.-Y. Liang, E. A. Paisley, A. Sepulveda, J. F. Ihlefeld, G. P. Carman, and C. S. Lynch, "Generation of localized strain in a thin film piezoelectric to control individual magnetoelectric heterostructures", Applied Physics Letters **107**, 092903 (2015).

[70] H. Sohn, C.-y. Liang, M. E. Nowakowski, Y. Hwang, S. Han, J. Bokor, G. P. Carman, and R. N. Candler, "Deterministic multi-step rotation of magnetic single-domain state in nickel nanodisks using multiferroic magnetoelastic coupling", Journal of Magnetism and Magnetic Materials **439**, 196 (2017).

[71] K. Roy, S. Bandyopadhyay, and J. Atulasimha, "Energy dissipation and switching delay in stress-induced switching of multiferroic nanomagnets in the presence of thermal fluctuations", Journal of Applied Physics **112**, 023914 (2012).

[72] K. Roy, "Ultra-low-energy straintronics using multiferroic composites", in Spin, Vol. 3, 02 (World Scientific, 2013), p. 1330003.

[73] K. Roy, S. Bandyopadhyay, and J. Atulasimha, "Hybrid spintronics and straintronics: a magnetic technology for ultra low energy computing and signal processing", Applied Physics Letters **99**, 063108 (2011).

[74] M. S. Fashami, K. Roy, J. Atulasimha, and S. Bandyopadhyay, "Magnetization dynamics, bennett clocking and associated energy dissipation in multiferroic logic", Nanotechnology **22**, 155201 (2011).

[75] M. Salehi-Fashami, M. Al-Rashid, W.-Y. Sun, P. Nordeen, S. Bandyopadhyay, A. Chavez, G. Carman, and J. Atulasimha, "Binary information propagation in circular magnetic nanodot arrays using strain induced magnetic anisotropy", Nanotechnology **27**, 43LT01 (2016).

[76] N. DrSouza, J. Atulasimha, and S. Bandyopadhyay, "Energy-efficient bennett clocking scheme for four-state multiferroic logic", IEEE Transactions on Nanotechnology **11**, 418 (2012).

2 Modeling Magnetic Nanostructures

2.1 Introduction

Improvements in micro- and nano-fabrication techniques have offered unprecedented capabilities in the manipulation of material structures and properties [1]. These advances offer new opportunities for engineering novel magnetic materials and devices where an immediate impact can be made in the development of ultra-high-density-magnetic storage [2]. As interest in these magnetic devices has increased, the need for sophisticated modeling tools has grown as well. Although magnetization originates from the spin and angular momentum of electrons in a material, the modeling techniques widely used assume a continuum approximation of magnetization even for nanoscale devices. The micromagnetic theory used for these simulations was first developed in a seminal paper of Landau and Lifshitz followed by several prominent papers from Brown [3–7]. Subsequently a detailed treatment of micromagnetic theory was given by Brown in [8]. In the micromagnetic theory a continuous magnetization vector is used to describe the details of the transition region between magnetic domains instead of accounting for the contribution of individual atomic magnetic moments. Using this assumption, magnetic domain structures and nucleation states can be determined from standard energy minimization techniques. However, this approach does not accurately predict magnetization reversal and so is only useful for static problems. To address dynamic systems, modeling efforts have focused on the Landau-Lifshitz-Gilbert (LLG) equation which describes the precessional motion of the magnetic moment. Since only a handful of analytical solutions are possible, modern simulation tools have used either finite difference or finite element methods to solve the LLG equation.

In this chapter, two techniques used for modeling the magnetoelastic nanostructures studied in the remainder of this work are presented. The first method involves solving only the governing micromagnetics equation known as the Landau-Lifshitz-Gilbert (LLG) equation. The second method then couples the LLG equation with the elastodynamics and piezoelectric constitutive

equations. Here we begin by providing the LLG equation and associated effective magnetic field terms that account for external stimuli such as applied strains. Next, the fully-coupled model is developed by introducing the relevant energy terms and associated effective magnetic fields. Lastly, a weak formulation coupling the LLG and elastodynamics equations is derived for implementation in a finite element numerical code.

2.2 Micromagnetics

The magnetization dynamics of magnetoelastic nanostructures, in a continuum approximation, can be determined from a Landau-Lifshitz-Gilbert (LLG) micromagnetics formulation [9, 10]

$$\frac{\partial \underline{m}}{\partial t} = -\mu_0 \gamma \left(\underline{m} \times \underline{H}_{eff}\right) + \alpha \left(\underline{m} \times \frac{\partial \underline{m}}{\partial t}\right) \tag{2.1}$$

where $\underline{m}$ is the normalized magnetization vector, μ_0 is the permeability of free space, γ is the gyromagnetic ratio, and α is the Gilbert damping constant. Here, thermal fluctuations are neglected, but room temperature material properties are used. Hence, in EQ 2.1, the effective magnetic field ($\underline{H}_{eff}$) of the system is the sum of the externally applied field ($\underline{H}_{ex}$), exchange field ($\underline{H}_{ex}$), demagnetization field ($\underline{H}_{d}$), magnetoelastic field ($\underline{H}_{me}$), and magnetocrystalline anisotropy (MCA) field ($\underline{H}_{anis}$). Specifically, the effective field is given by

$$\underline{H}_{eff} = \underline{H}_{ext} + \underline{H}_{ex} + \underline{H}_{anis} + \underline{H}_{d} + \underline{H}_{me} \tag{2.2}$$

Additionally, the model assumes small elastic deformations as well as uniform strains within the magnetoelastic elements [11, 12]. Consequently, the magnetoelastic field is defined by

$$\underline{H}_{me} = \frac{3\lambda_s Y \left(\varepsilon_x - \varepsilon_y\right)}{\mu_0 M_s} \tag{2.3}$$

where λ_s is the saturation magnetostriction, Y is the Young's modulus, M_s is the saturation magnetization, and (ε_x, ε_y) are strains in the x and y directions, respectively. In particular,

these values represent voltage-induced strains where the biaxial strain difference of EQ 2.3 is produced by applying an electric field to patterned electrodes on a piezoelectric layer. The $\underline{H}_{me}$ term is represented in EQ 2.3 by a uniform uniaxial anisotropy defined as [13, 14]

$$K_{\varepsilon} = \frac{1}{2}\mu_0 M_s \underline{H}_{me} \tag{2.4}$$

For this work, a cubic crystal structure is typically used. Thus, the effective field due to MCA is given by

$$\underline{H}^{i}_{anis} = \frac{-2}{\mu_0 M_s}\left[Kc_1\left(m_j^2 + m_k^2\right) + Kc_2\left(m_j^2 m_k^2\right)\right] \tag{2.5}$$

where m_i is the magnetization component in the ith direction and the Kc_i are first and second order cubic anisotropy constants, respectively [14–16]. This LLG formulation is solved within MuMax3 using a Dormand-Prince finite difference method [17, 18].

2.3 Fully-coupled Model

A deeper understanding of the effects of mechanical strain on the magnetoelastic response of nanostructures can be obtained by extending the micromagnetics formulation of Section 2.2 to include coupling between the magnetic, mechanical, and piezoelectric governing equations. This was done by Liang et al. [19–22] and is achieved by coupling the LLG equation with the elastodynamics and piezoelectric constitutive equations. For brevity, this section provides only the coupling of the micromagnetics and mechanical governing equations through a weak formulation suited for implementation in a finite element framework [23]. This is sufficient to describe the fully-coupled model developed by Liang et al. [19] since it is straightforward to couple the linear piezoelectric equations to the weak formulation developed in this section. We begin by presenting the relevant energy terms of a magnetic system. Then the corresponding effective magnetic fields are determined. Lastly, a weak formulation of the LLG equation is derived for implementation in the finite element software COMSOL.

2.3.1 Energy Terms

The total energy of the system has contributions from the externally applied magnetic field (E_{ext}), the exchange interaction (E_{ex}), crystal anisotropy (E_{anis}), demagnetization (E_d), and the magnetoelastic interaction (E_{me}). It is worth noting that each magnetic energy term boils down to some form of the dot product of the magnetization ($\underline{m}$) and the corresponding field (e.g., H_{ex}). Here, it will be assumed that the crystal structure is cubic. The energy terms are then given by the following equations:

$$E_{tot} = E_{ext} + E_{ex} + E_{anis} + E_d + E_{me} \tag{2.6}$$

$$E_{ext} = -\mu_o M_s(\underline{m} \cdot \underline{H}_{ext}) \tag{2.7}$$

$$E_{ex} = A_{ex}(\nabla \underline{m})^2 \tag{2.8}$$

$$E_{anis}^{cubic} = K_1(m_1^2 m_2^2 + m_1^2 m_3^2 + m_2^2 m_3^2) + K_2(m_1^2 m_2^2 m_3^2) \tag{2.9}$$

$$E_d = -\frac{\mu_o M_s}{2}(\underline{m} \cdot \underline{H}_d) \tag{2.10}$$

$$E_{me} = \frac{1}{2}\underline{\underline{\varepsilon}}^{el} : \underline{\underline{\underline{\underline{C}}}} : \underline{\underline{\varepsilon}}^{el} \tag{2.11}$$

where M_s is the saturation magnetization of the material, A_{ex} is the exchange stiffness of the material, the K_i are anisotropy constants determined from experiment, ε^{el} is the elastic strain tensor, and C is the elastic stiffness tensor of the material. In a magnetoelastic material, the magnetic moments and displacements of the material are coupled such that the total strain ($\underline{\underline{\varepsilon}}$) is a summation of magnetic ($\underline{\underline{\varepsilon}}^m$) and mechanical/elastic ($\underline{\underline{\varepsilon}}^{el}$) components. In component form, the strain associated with a cubic crystal is

$$\varepsilon_{ij}^m = \begin{cases} \frac{3}{2}\lambda_{100}\left(m_i m_j - \frac{1}{3}\right), & \text{for } i = j \\ 3n+1, & \text{for } i \neq j \end{cases} \tag{2.12}$$

2.3.2 Effective Fields

To better understand the effects each energy term plays in determining the state of a magnetic system, it is useful instead to study the influence of corresponding effective magnetic fields. These fields can be obtained by taking derivatives of the corresponding energy terms with respect to the magnetization vector. That is,

$$\underline{H}_{eff} = \frac{-1}{\mu_o M_s} \frac{\partial E_{tot}}{\partial \underline{m}} \tag{2.13}$$

Clearly, the effective field due to the externally applied bias field ($\underline{H}_{ext}$) is itself the bias field, i.e.,

$$\underline{H}_{ext} = H_{app} \tag{2.14}$$

The effective field due to the anistropy for a cubic crystal structure ($\underline{H}_{anis}$) is given in component form as

$$\underline{H}^i_{anis} = -\frac{2m_i}{\mu_o M_s}[K_1(m_j^2 + m_k^2) + K_2(m_j^2 m_k^2)] \tag{2.15}$$

Similarly, the effective field from the magnetoelastic interaction is found as

$$\begin{aligned} \underline{H}_{me} &= -\frac{1}{\mu_o M_s} \frac{\partial}{\partial \underline{m}} \left(\frac{1}{2} \underline{\underline{\underline{C}}} (\underline{\underline{\varepsilon}}^{el})^2 \right) && (2.16) \\ &= -\frac{1}{\mu_o M_s} \frac{\partial}{\partial \underline{m}} \left(\frac{1}{2} \underline{\underline{\underline{C}}} \left(\underline{\underline{\varepsilon}} - \underline{\underline{\varepsilon}}^m \right)^2 \right) && (2.17) \\ &= -\frac{1}{\mu_o M_s} \underline{\underline{\underline{C}}} (\underline{\underline{\varepsilon}} - \underline{\underline{\varepsilon}}^m) \cdot \frac{\partial \varepsilon^m}{\partial \underline{m}} && (2.18) \end{aligned}$$

The effective field due to demag is evidently the demag field. However, it is advantageous to write the demag field in terms of a potential. From Ampere's Law ($\nabla \times \underline{H}_d = 0$), Gauss' Law ($\nabla \cdot \underline{B} = 0$), and the relationship between the magnetic induction and magnetization ($\underline{B} = \underline{H}_d + M_s \underline{m}$), one can write the demag field in terms of a magnetic potential (ϕ):

$$\underline{H}_d = -\nabla \phi \tag{2.19}$$

Before deriving the effective exchange field, we will perform some preliminary calculations starting with expanding $\nabla\underline{m}$:

$$\begin{aligned}
\nabla\underline{m} &= \left(\hat{e}_x\frac{\partial}{\partial x}+\hat{e}_y\frac{\partial}{\partial y}+\hat{e}_z\frac{\partial}{\partial z}\right)(m_1\hat{e}_x+m_2\hat{e}_y+m_3\hat{e}_z) \\
&= m_{1,x}\hat{e}_x\hat{e}_x+m_{1,y}\hat{e}_y\hat{e}_x+m_{1,z}\hat{e}_z\hat{e}_x \\
&+ m_{2,x}\hat{e}_x\hat{e}_y+m_{2,y}\hat{e}_y\hat{e}_y+m_{2,z}\hat{e}_z\hat{e}_y \\
&+ m_{3,x}\hat{e}_x\hat{e}_z+m_{3,y}\hat{e}_y\hat{e}_z+m_{3,z}\hat{e}_z\hat{e}_z \\
\Leftrightarrow & \begin{pmatrix} m_{1,x} & m_{1,y} & m_{1,z} \\ m_{2,x} & m_{2,y} & m_{2,z} \\ m_{3,x} & m_{3,y} & m_{3,z} \end{pmatrix}
\end{aligned}$$

noting that $(\nabla\underline{m})^2 = (\nabla\underline{m}) : (\nabla\underline{m})$ is the double dot product (i.e., dot product for matrices), we find

$$\begin{aligned}
(\nabla\underline{m})^2 &= (\nabla\underline{m}) : (\nabla\underline{m}) \\
&= \begin{pmatrix} m_{1,x} & m_{1,y} & m_{1,z} \\ m_{2,x} & m_{2,y} & m_{2,z} \\ m_{3,x} & m_{3,y} & m_{3,z} \end{pmatrix} : \begin{pmatrix} m_{1,x} & m_{1,y} & m_{1,z} \\ m_{2,x} & m_{2,y} & m_{2,z} \\ m_{3,x} & m_{3,y} & m_{3,z} \end{pmatrix} \\
&\equiv m_{1,x}^2+m_{1,y}^2+m_{1,z}^2+m_{2,x}^2+m_{2,y}^2+m_{2,z}^2+m_{3,x}^2+m_{3,y}^2+m_{3,z}^2
\end{aligned}$$

Recall, in order to find the effective field, a derivative of the energy taken with respect to the magnetization vector must be computed. Specifically, for the exchange energy, the first variation is taken such that

$$\int[\delta E_{ex}]dV = \int\left[A_{ex}\delta(\nabla\underline{m})^2\right]dV = A_{ex}\int[H_{eff}\cdot\delta\underline{m}]dV \tag{2.20}$$

The first variation is

$$\begin{aligned}\int A_{ex}\delta(\nabla\underline{m})^2 dV &= A_{ex}\int \delta(m_{1,x}^2+m_{1,y}^2+m_{1,z}^2+m_{2,x}^2+m_{2,y}^2+m_{2,z}^2 \\ &\qquad +m_{3,x}^2+m_{3,y}^2+m_{3,z}^2)dV \\ &\Leftrightarrow\ A_{ex}\int \delta(m_{i,j}m_{i,j})dV \\ &= A_{ex}\int 2m_{i,j}\delta m_{i,j}dV\end{aligned}$$

Integrating by parts diagramatically

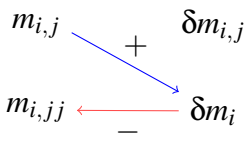

The integrand becomes

$$A_{ex}\int 2m_{i,j}\delta m_{i,j}dV = 2A_{ex}\int[-m_{i,jj}\delta m_i]dV + 2A_{ex}\int[m_{i,j}\delta m_i]dS$$

From the boundary conditions we have $m_{i,j}\delta m_i \to 0$. Now consider the following calculation,

$$\begin{aligned}\nabla^2\underline{m} &\equiv \nabla(\nabla\cdot\underline{m}) - \nabla\times(\nabla\times\underline{m}) \\ &\Leftrightarrow \partial_k\hat{e}_k(\partial_m\hat{e}_m\cdot m_n\hat{e}_n) - \partial_j\hat{e}_j\times(\varepsilon_{lin}m_{n,i}\hat{e}_l) \\ &= \partial_k\hat{e}_k(m_{n,m}\delta_{mn}) - (m_{n,ij}\varepsilon_{lin}\varepsilon_{rjl}\hat{e}_r) \\ &= m_{n,nk}\hat{e}_k - [m_{n,ij}(\delta_{ir}\delta_{nj}-\delta_{ij}\delta_{nr})\hat{e}_r] \\ &= m_{n,nk}\hat{e}_k - m_{n,nr}\hat{e}_r + m_{r,jj}\hat{e}_r \\ &= m_{k,jj}\hat{e}_k\end{aligned}$$

Therefore,

$$\int A_{ex}\delta(\nabla\underline{m})^2 dV = 2A_{ex}\int[\nabla^2\underline{m}\cdot\delta\underline{m}]dV \tag{2.21}$$

From EQ 2.20 the effective exchange field is then given by

$$\underline{H}_{ex} = \frac{2A_{ex}}{\mu_o M_s}\nabla^2 \underline{m} \tag{2.22}$$

2.3.3 Weak formulation of LLG

In order to implement LLG in a multiphysics software such as COMSOL, it is necessary to express the LLG equation in a weak form. The weak form requires an order reduction of the governing differential equation. Additionally, weakening the governing equation involves rewriting it in the form of a volume integral multiplied by a test function ψ as done in EQ 2.23 for the LLG equation:

$$\int \left(\left[\frac{\partial \underline{m}}{\partial t} - \alpha \left(\underline{m} \times \frac{\partial \underline{m}}{\partial t} \right) \right] \cdot \psi + \mu_o \gamma (\underline{m} \times \underline{H}_{eff}) \cdot \psi \right) dV = 0 \tag{2.23}$$

From the definition of the effective field (EQ 2.2), the third term becomes:

$$\int \mu_o \gamma (\underline{m} \times \underline{H}_{eff}) \cdot \psi dV = \int \mu_o \gamma (\underline{m} \times [\underline{H}_{ext} + \underline{H}_{ex} + \underline{H}_{anis} + \underline{H}_d + \underline{H}_{me}]) \cdot \psi dV \tag{2.24}$$

Since the effective field due to the exchange interaction involves second order derivatives (see EQ 2.22), it must be weakened through integration by parts. Noting that the cross product is distributive, we have

$$\begin{aligned}
\int \mu_o \gamma (\underline{m} \times \underline{H}_{ex}) \cdot \psi dV &= \frac{2A_{ex}\gamma}{M_s} \int (\underline{m} \times \nabla^2 \underline{m}) \cdot \psi dV \\
&\Leftrightarrow \frac{2A_{ex}\gamma}{M_s} \int [m_n \hat{e}_n \times (m_{i,jj} \hat{e}_i)] \cdot (\psi_s \hat{e}_s) dV \\
&= \frac{2A_{ex}\gamma}{M_s} \int (m_n m_{i,jj} \varepsilon_{lni} \hat{e}_l) \cdot (\psi_s \hat{e}_s) dV \\
&= \frac{2A_{ex}\gamma}{M_s} \int \varepsilon_{sni} \psi_s m_n m_{i,jj} dV
\end{aligned}$$

In order to weaken the equation, it is necessary to "share" derivatives from the $m_{i,jj}$ term with the remaining terms. This is accomplished through integration by parts:

$$\frac{2A_{ex}\gamma}{M_s}\int \varepsilon_{sni}\psi_s m_n m_{i,jj}dV = \frac{2A_{ex}\gamma}{M_s}\left(\int (\psi_s m_n)_{,j} m_{i,j}\varepsilon_{sni}dV + \int (\psi_s m_n m_{i,j})n_j\varepsilon_{sni}dS\right)$$

From the boundary conditions we have $\psi_s m_{i,j} m_n \to 0$. Then EQ 2.3.3 becomes,

$$\frac{2A_{ex}\gamma}{M_s}\int \varepsilon_{sni}\psi_s m_n m_{i,jj}dV = -\frac{2A_{ex}\gamma}{M_s}\int (\psi_{s,j}m_n + \psi_s m_{n,j})m_{i,j}\varepsilon_{sni}dV$$

Noting that $\psi_s m_{i,j} m_{n,j}\varepsilon_{sni} = 0$, the exchange term reduces to

$$-\frac{2A_{ex}\gamma}{M_s}\int (\psi_{s,j}m_n + \psi_s m_{n,j})m_{i,j}\varepsilon_{sni}dV = -\frac{2A_{ex}\gamma}{M_s}\int m_{i,j}\psi_{s,j}m_n\varepsilon_{sni}dV$$

Observe that $m_{i,j}\psi_{s,j}m_n\varepsilon_{sni} = \varepsilon_{sni}m_n m_{i,j}\psi_{s,j}$, which is simply a cross product between the magnetization vector and its spatial derivatives dotted with the spatial derivative of the test function, i.e.,

$$-\frac{2A_{ex}\gamma}{M_s}\int m_{i,j}\psi_{s,j}m_n\varepsilon_{sni}dV \to -\frac{2A_{ex}\gamma}{M_s}\sum_s\int\left[\left(\underline{m}\times\frac{\partial\underline{m}}{\partial x_s}\right)\cdot\frac{\partial\psi_s}{\partial x_s}\right]dV \tag{2.25}$$

From EQ's 2.23, 2.24, and 2.25 the weak formulation of the LLG equation is given by

$$\begin{aligned}\int\left(\left[\frac{\partial\underline{m}}{\partial t}-\alpha\left(\underline{m}\times\frac{\partial\underline{m}}{\partial t}\right)\right]\right)\cdot\psi dV &= \int\mu_o\gamma(\underline{m}\times[\underline{H}_{ext}+\underline{H}_{anis}+\underline{H}_d+\underline{H}_{me}])\cdot\psi dV \\ &+\frac{2A_{ex}\gamma}{M_s}\sum_s\int\left[\left(\underline{m}\times\frac{\partial\underline{m}}{\partial x_s}\right)\cdot\frac{\partial\psi_s}{\partial x_s}\right]dV\end{aligned} \tag{2.26}$$

Observe from the previous derivations that all the terms except the demag term are explicitly dependent on the magnetization vector ($\underline{m}$). To account for the scalar potential (i.e., demag) in COMSOL, a separate PDE module for which there is a single dependent variable (ϕ) must be used. The remaining terms in EQ 2.26 are then modeled in the second PDE module.

2.4 Conclusion

In this section, we presented two techniques used for modeling the magnetoelastic nanostructures studied in the remainder of this work. The first method involves solving only the Landau-Lifshitz-Gilbert micromagnetics equation using a finite difference method in which mechanical strains are represented as effective magnetic fields. The second method couples the LLG equation with the elastodynamics and piezoelectric constitutive equations and solves the system of PDE's using an iterative finite element approach that captures the interdependence of nonuniform distributions of strain and magnetization. Lastly, building on this framework, a weak formulation of the LLG and elastodynamics equations was derived for implementation in a finite element numerical code.

2.5 Chapter References

[1] H. Long, Z. Liu, E. Ong, and E. Li, "Micromagnetic modeling simulations and applications", in Electromagnetic compatibility, 2006. emc-zurich 2006. 17th international zurich symposium on (IEEE, 2006), pp. 398–401.

[2] J. Fidler and T. Schrefl, "Micromagnetic modelling-the current state of the art", Journal of Physics D: Applied Physics **33**, R135 (2000).

[3] L. Landau and E. Lifshitz, Physikalische Zeitschrift der Sowjetunion **8** (1935).

[4] W. F. Brown Jr, "Domain theory of ferromagnetics under stress: part 1", Physical Review **52**, 325 (1937).

[5] W. F. Brown Jr, "Theory of reversible magnetization in ferromagnetics", Physical Review **55**, 568 (1939).

[6] W. F. Brown Jr, "Theory of the approach to magnetic saturation", Physical Review **58**, 736 (1940).

[7] W. F. Brown Jr, "Ferromagnetic domains and the magnetization curve", Journal of Applied Physics **11**, 160 (1940).

[8] W. F. Brown, *Micromagnetics*, 18 (Interscience Publishers, 1963).

[9] T. Gilbert, "Classics in Magnetics A Phenomenological Theory of Damping in Ferromagnetic Materials", IEEE Transactions on Magnetics **40**, 3443 (2004).

[10] M. Lakshmanan, "The fascinating world of the landau–lifshitz–gilbert equation: an overview", Philosophical Transactions of the Royal Society of London A: Mathematical, Physical and Engineering Sciences **369**, 1280 (2011).

[11] I. Gilbert, A. C. Chavez, D. T. Pierce, J. Unguris, W.-Y. Sun, C.-Y. Liang, and G. P. Carman, "Magnetic microscopy and simulation of strain-mediated control of magnetization in pmn-pt/ni nanostructures", Applied physics letters **109**, 162404 (2016).

[12] A. C. Chavez, W.-Y. Sun, J. Atulasimha, K. L. Wang, and G. P. Carman, "Voltage induced artificial ferromagnetic-antiferromagnetic ordering in synthetic multiferroics", Journal of Applied Physics **122**, 224102 (2017).

[13] B. D. Cullity and C. D. Graham, *Introduction to magnetic materials* (John Wiley & Sons, 2011).

[14] R. C. O'handley, *Modern magnetic materials: principles and applications* (Wiley, 2000).

[15] S. Chikazumi, *Physics of magnetism* (Wiley, 1964).

[16] J. M. Coey, *Magnetism and magnetic materials* (Cambridge University Press, 2010).

[17] A. Vansteenkiste, J. Leliaert, M. Dvornik, M. Helsen, F. Garcia-Sanchez, and B. Van Waeyenberge, "The design and verification of MuMax3", AIP Advances **4** (2014) 10.1063/1.4899186.

[18] A. Vansteenkiste and B. V. De Wiele, "MUMAX: A new high-performance micromagnetic simulation tool", Journal of Magnetism and Magnetic Materials **323**, 2585 (2011).

[19] C.-Y. Liang, S. M. Keller, A. E. Sepulveda, A. Bur, W.-Y. Sun, K. Wetzlar, and G. P. Carman, "Modeling of magnetoelastic nanostructures with a fully coupled mechanical-micromagnetic model", Nanotechnology **25** (2014) 10.1088/0957-4484/25/43/435701.

[20] C. Y. Liang, S. M. Keller, A. E. Sepulveda, W. Y. Sun, J. Cui, C. S. Lynch, and G. P. Carman, "Electrical control of a single magnetoelastic domain structure on a clamped piezoelectric thin film - Analysis", Journal of Applied Physics **116** (2014) 10.1063/1.4896549.

[21] C.-Y. Liang, A. E. Sepulveda, D. Hoff, S. M. Keller, and G. P. Carman, "Strain-mediated deterministic control of 360 domain wall motion in magnetoelastic nanorings", Journal of Applied Physics **118**, 174101 (2015).

[22] C.-Y. Liang, A. Sepulveda, S. Keller, and G. P. Carman, "Deterministic switching of a magnetoelastic single-domain nano-ellipse using bending", Journal of Applied Physics **119**, 113903 (2016).

[23] H. Szambolics, J.-C. Toussaint, L. Buda-Prejbeanu, F. Alouges, E. Kritsikis, and O. Fruchart, "Innovative weak formulation for the landau–lifshitz–gilbert equations", IEEE Transactions on Magnetics **44**, 3153 (2008).

3 Magnetic Microscopy and Simulation of Strain-mediated Magnetization Control in Ni Disks

3.1 Background

One of the primary goals of the field of spintronics is to electrically control magnetization in a reliable and efficient manner [1–4]. Many methods for manipulating magnetization electrically have been explored experimentally. For example, the coupling between ferroelectric and magnetic order parameters in single-phase multiferroic systems such as $BiFeO_3$ [5, 6] is one avenue by which electrical control of magnetism may be achieved [7–9]. Another example is the use of spin transfer torque (STT) for information encoding in magnetic memory devices such as magnetic tunnel junctions and domain wall motion devices [10–12]. An additional method for electrically controlling magnetism involves generating a spin-orbit torque through the spin hall effect for switching the magnetization in bilayers consisting of ferromagnets and heavy metals [13–15]. Lastly, electrical control of magnetism can be achieved by leveraging the magnetoelastic coupling in a piezoelectric/ferromagnet heterostructure, a method which has gained significant interest because of its ultra-low energy strain-mediated switching mechanism [16–19]. For this control scheme, an applied electric field generates a strain in the piezoelectric layer, and this strain then causes a change in the direction of the ferromagnetic layer's easy axis through magnetostriction. Simulations suggest this strain-mediated approach can be used to switch the magnetic moment of a nanomagnet while dissipating less than 1.5 aJ, making this approach the most promising in terms of energy efficiency [20, 21].

Here we use scanning electron microscopy with polarization analysis (SEMPA) [22, 23] to study the strain-induced magnetization changes in Ni films and submicron disks patterned on a

ferroelectric $[Pb(Mg_{1/3}Nb_{2/3})O_3]_{0.68}[PbTiO_3]_{0.32}$ (PMN-PT) substrate. Strain is generated by applying an electric field to the underlying ferroelectric layer and SEMPA images taken before and after application of the electric field allow precise determination of changes to the three-dimensional vector magnetization with a resolution in the tens of nanometers. The magneto-electric coupling strongly affects the vortex magnetization patterns in the Ni disks. Specifically, the strain can either compresses a vortex state into two antiparallel domains that point along the strain defined easy axis, or it can remove the vortex core resulting in a single-domain state. The SEMPA images are used to quantitatively evaluate the accuracy of two types of micromagnetic simulations: one which treats the strain with a simple uniform uniaxial anisotropy, and another that fully couples elastodynamic equations with the Landau-Lifshitz-Gilbert (LLG) equation to capture the effects of the local structure of the strain on the magnetization. While both models produce satisfactory results, the fully-coupled elastodynamic and micromagnetic simulation produces more accurate results, demonstrating a deficiency in the standard micromagnetics formalism that uses a spatially uniform uniaxial anisotropy to model magnetoelastic effects. The improved accuracy of the fully coupled solution would be crucial in accurately predicting device designs/responses near instabilities or studies relying on highly magnetoelastic materials such as Terfenol-D $(Tb_{0.3}Dy_{0.7})Fe_{1.92}$.

3.2 Device Fabrication

The sample geometry considered here is illustrated in Figure 3.1. Submicron Ni disks were patterned on a 10 mm $\times$ 10 mm $\times$ 0.5 mm single crystal PMN-PT (011) substrate. The [100] in-plane crystallographic axis of the PMN-PT substrate is aligned with the sample's y-direction while the [01$\underline{1}$] in-plane crystallographic axis is aligned with the x-direction. Planar electrodes are evaporated on the PMN-PT's top (30 nm Pt) and bottom (30 nm Ta) surfaces. The disks have diameters ranging from 100 nm to 1000 nm and are patterned by electron beam lithography on the top (Pt) surface using a double layer of PMMA/MMA e-beam resist followed by electron beam evaporation of Ti(5 nm)/Ni(12 nm) and liftoff. The PMN-PT substrate was poled with a

0.8 MV/m electric field before the Ti/Ni film was deposited. Applying a post-poling electric field of 0.8 MV/m produces anisotropic in-plane strain 21. The differences in strain between $E = 0$ MV/m and $E = 0.8$ MV/m are $\varepsilon_{yy} = 1200\mu$m/m and $\varepsilon_{xx} = -3200\mu$m/m, as shown in Figure 1b for a similar substrate. The large strain jump at 0.6 MV/m is due to an electric field-induced phase transformation from the rhombohedral phase to the orthorhombic phase that is strongly dependent upon the PMN-PT composition. Optical and scanning electron micrographs illustrating the sample geometry are presented in Figure 3.1(c) and 3.1(d).

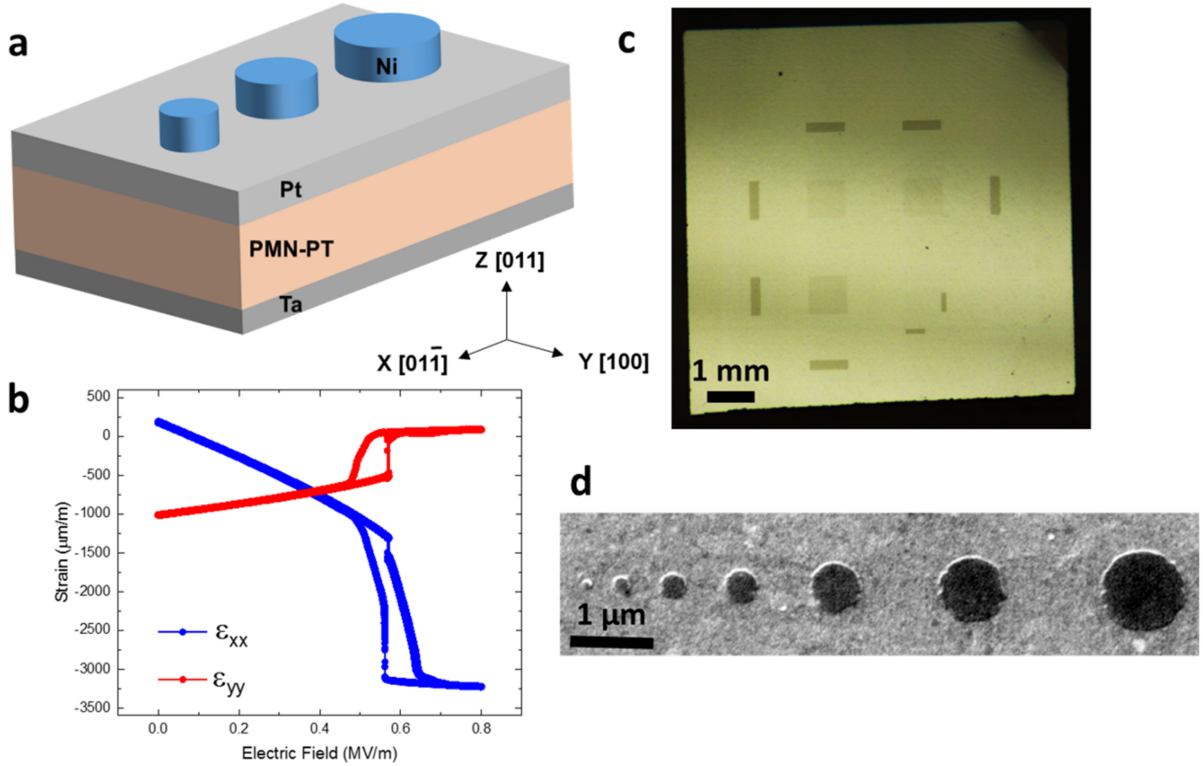

Figure 3.1: (a) Diagram of the sample geometry used in this work. Pt and Ta electrodes on either side of a 500 μm thick PMN-PT substrate are used to apply an electric field in the z direction. (b) Plot of strain in a similar PMN-PT substrate as a function of applied electric field. Uncertainties are derived from uncertainty of the instrument and are less than 5%. (c) Optical micrograph of the sample. The rectangular patterns are used for alignment and sample orientation during electron beam writing. The square patterns are the Ni nanostructure arrays. (d) Scanning electron micrograph showing Ni disks ranging from 100 nm to 1 μm in diameter. [24]

3.3 Modeling Overview

The magnetization data obtained by SEMPA are used to validate the modeling methods discussed in Sections 2.2 and 2.3. Specifically, two nickel disks of 400 nm and 600 nm diameter are modeled using the fully-coupled and purely micromagnetics formulations previously discussed in Ch 2. For each model, temperature fluctuations are neglected, but room temperature material properties are assumed. Additionally, each model assumes small elastic deformations and linear elasticity. Magnetocrystalline anisotropy is also neglected because the evaporated Ni film grain size (3 nm) is smaller than the exchange length. The ground state of each disk was determined by starting the system in a randomly oriented magnetic state and allowing it to settle into a stable configuration. The disks are modeled for the unstrained and strained conditions of the experiment. The strained model corresponds to a strain state with -3200 μm/m (compressive strain) along the x-axis and 1200 μm/m (tensile strain) along the y-axis. For the fully-coupled model, the geometry was discretized using tetrahedral elements with a size on the order of the exchange length of Ni (8.5 nm). The material properties used for the nickel disks were $M_s = 4.8 \times 10^5$ A/m, $A_{ex} = 1.05 \times 10^{-11}$ J/m, $\alpha = 0.08$, $\lambda_{100} = -46 \times 10^{-6}$, $\lambda_{111} = -24 \times 10^{-6}$, $c_{11} = 2.5 \times 10^{11}$ N/m^2, $c_{12} = 1.6 \times 10^{11}$ N/m^2, $c_{44} = 1.18 \times 10^{11}$ N/m^2. For the fully-coupled model, the Ni disks were discretized using tetrahedral elements with a size on the order of Ni exchange length (8.5 nm). For the purely micromagnetics simulation, cubic elements (1 nm^3) were used to mesh the disks.

3.4 Results

Nanoscale imaging of the magnetization of the patterned structures was performed at room temperature using scanning electron microscopy with polarization analysis (SEMPA). SEMPA is a scanning electron microscopy technique in which the spin polarization of the secondary electrons is measured, allowing a map of the sample's magnetization to be constructed [22, 23]. The initial magnetization configuration was set by applying a 120 mT magnetic field in the $+x$

direction. The surface was cleaned in situ with Ar+ ion beam etching to remove contaminants and native oxide. The etch process was monitored with Auger electron spectroscopy. Following cleaning, a few monolayers of Fe were evaporated onto the sample, a standard technique used to increase the spin polarization measured by SEMPA without altering the structure of the underlying magnetization [25]. We first studied the effect of an applied electric field on the magnetization of large Ni rectangles. Figure 3.2 shows SEMPA images of a corner of one of these rectangles. On the Ni portion of the sample, the magnetization of the Fe layer follows that of the underlying Ni, whereas on the surrounding substrate, the Fe magnetization forms its own domain structure. Note that the exchange coupling between the Fe layer and the Ni structures is much stronger than magnetostriction, so while the Fe deposited directly on the PMN-PT responds according to the Fe magnetostriction alone, the Fe deposited on the Ni is locked to the Ni magnetization, which has opposite magnetostriction. Figure 3.2(b) shows that without an applied electric field, the Ni is mostly magnetized in the $\pm y$ direction (determined by the rectangle's shape anisotropy), while the Fe on the surrounding substrate is mostly magnetized in the $\pm x$ direction. The differences in orientation may be due to residual strain in the substrate that sets the initial Fe magnetization configuration during growth. As seen in Figure 3.2(c), when an electric field of 0.8 MV/m is applied, the substrate is strained, and the Ni magnetization rotates to point in the $\pm x$ direction while the Fe rotates to point in the $\pm y$ direction. In Figures 3.2(e) and 3.2(f), polar plots show the distribution of magnetization directions extracted from Figures 3.2(b) and 3.2(c), respectively. The opposite preferred magnetization axes of the Fe and Ni regions of the sample are due to the opposite signs of the magnetostriction coefficients for these two materials, i.e. Fe has a positive magnetostriction coefficient while Ni has a negative magnetostriction coefficient. The electric-field-induced anisotropic strain from the PMN-PT substrate produces an easy axis in the Fe along the $\pm y$ direction and an easy axis in the Ni along the $\pm x$ direction.

Figures 3.3(a)-3.3(d) show SEMPA images for the patterned nickel disks. The large disks exhibit a vortex magnetization pattern, while the small disks exhibit uniform magnetization. The diameter at which the crossover from vortex to single domain occurs (approximately 500

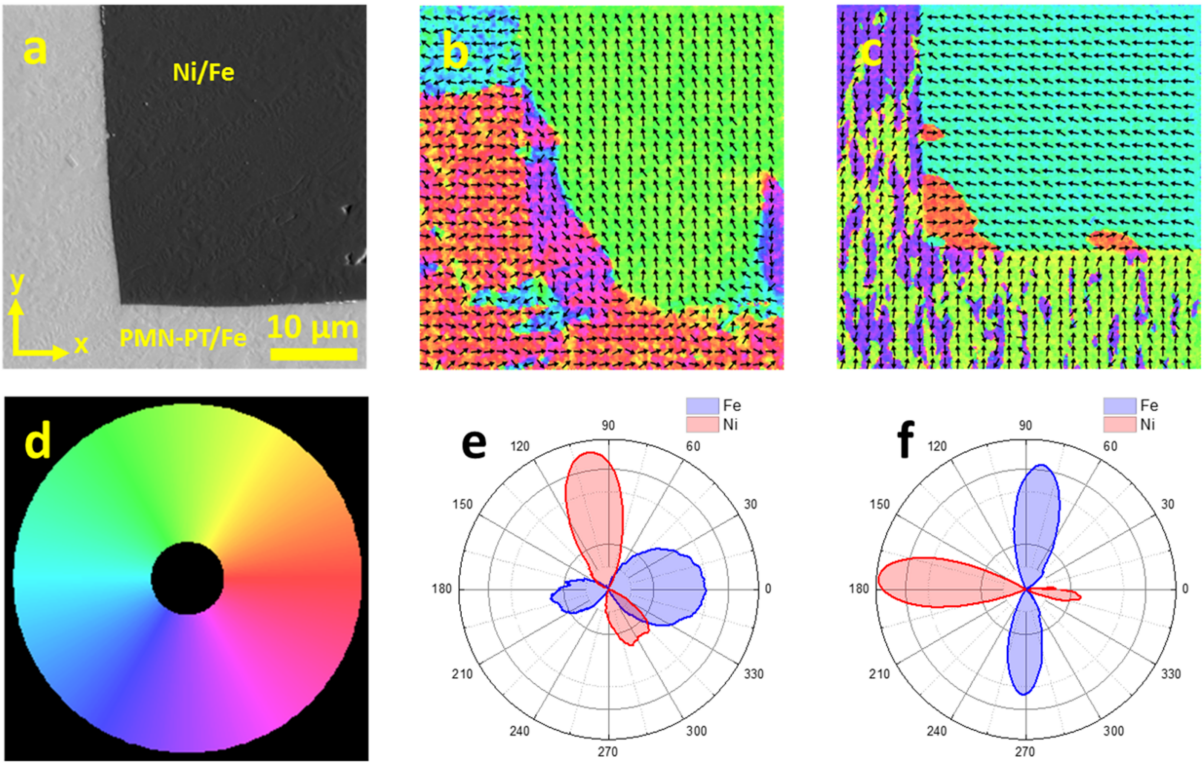

Figure 3.2: (a) Scanning electron micrograph showing the corner of a large Ni rectangle on a PMN-PT substrate. The entire area (substrate and Ni) is covered with a few monolayers of Fe to improve magnetic contrast in SEMPA. (b) SEMPA image showing the magnetization of the Ni rectangle as well as the thin layer of Fe on the PMN-PT substrate without an applied electric field. (c) Image of same area after straining the sample by applying a 0.8 MV/m electric field to the substrate. The magnetization directions in (b) and (c) are given by the color wheel in (d). This color scale is also used for all subsequent magnetization images in this work. (e) and (f): Polar plots showing the distribution of magnetization directions present in images (b) and (c), respectively. The blue portions represent the Fe magnetization, and the red portions represent the Ni magnetization. The strain produced by the applied electric field rotates the magnetization 90° and also slightly reduces the spread of the distribution of magnetization angles. [24]

nm) is not completely consistent due to the metastability of each state and the edge roughness in the individual disks. Using SEMPA, however, we can directly image the magnetization of each individual disk in its initial configuration and in the presence of an applied electric field, so the exact magnetization changes due to the magnetoelastic coupling with the substrate can be resolved on the nanoscale.

We focus on Ni disks initially magnetized in a vortex configuration, which allows us to probe the effect of strain on magnetization in all in-plane directions. In Figure 3.3(a)-3.3(d), we present SEMPA images of 400 and 600 nm Ni disks before and during the application of a 0.8 MV/m electric field. The 400 nm disk initially contains an off-center vortex (a), but the strain-induced anisotropy removes the vortex and rotates the disk's magnetization to point in the +x direction (b). The 600 nm disk initially contains a vortex located in the disk's center (c). Upon the application of the electric field, the regions of the magnetization parallel to the *x*-axis grow, while the regions of magnetization parallel to the *y*-axis shrink (d), as one would expect given the negative magnetostriction of Ni. The vortex core is not removed, but the strain in the piezoelectric substrate effectively compresses the vortex into two antiparallel domains. Note that because the strain is uniaxial rather than unidirectional, the disk does not enter a uniformly magnetized configuration.

The results of the fully-coupled simulations are presented in Figure 3.3(e)-3.3(h). Unlike the 400 nm disk in Figure 3.3(a), the 400 nm disk modeled here has a largely uniformly-magnetized ground state, though the magnetization does rotate at the disk's edge. The overall magnetization rotates by 90° upon the application of strain. Again, we note that the edge roughness of the experimental disks and the metastability of the vortex state prevent the completely consistent experimental generation of a uniformly-magnetized ground state. The magnetization of the 600 nm Ni disk, initially in a circular vortex configuration, is compressed somewhat by the application of strain, qualitatively consistent with the SEMPA images.

The results of the purely micromagnetics model are presented in Figure 3.3(i)-3.3(l). The 400

nm and a 600 nm diameter Ni disks are first modeled without a uniaxial anisotropy to capture the no strain condition followed by application of a uniaxial anisotropy equivalent to a 150 mT effective field. The effective field is related to the strain by $3\lambda_s c_{44}(\varepsilon_x - \varepsilon_y)/M_s$. When the uniaxial anisotropy is imposed, the magnetization rotates to the $+x$ direction, consistent with Figure 3.3(b). The 600 nm disk shows a vortex ground state in the micromagnetic simulation and, consistent with the SEMPA data shown in Figure 3.3(d), the vortex in the 600 nm disk is compressed by the strain. In order to more quantitatively compare the SEMPA images and

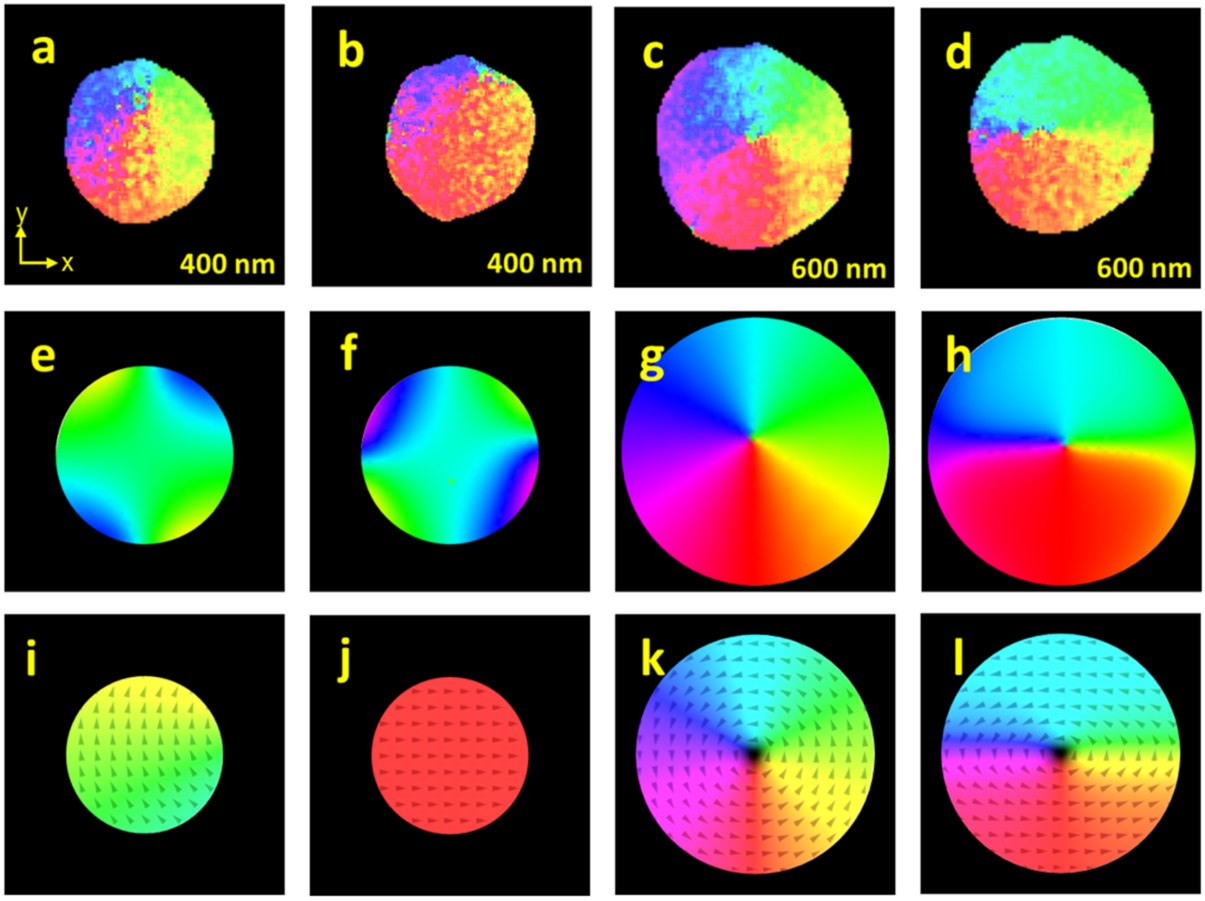

Figure 3.3: The effect of strain on 400 nm and 600 nm diameter Ni disks. (a) and (b) show SEMPA images of the magnetization of a 400 nm Ni disk before and during application of a 0.8 MV/m electric field to the substrate. The off-center vortex is removed and the magnetization is mostly uniform in this case. (c) and (d) show SEMPA images for a 600 nm Ni disk. The vortex is compressed into two antiparallel domains. (e) and (f) show simulation results of the fully-coupled model for the magnetization of a 400 nm Ni disk without (e) and with (f) strain. The strain rotates the magnetization by 90°. Analogous results for the 600 nm disk are presented in (g) and (h). The initial vortex magnetization configuration is compressed into two antiparallel domains. (i)-(l) show simulation results of the purely micromagnetics model for the same systems as (e)-(h). The color scale used here is the same as that in Figure 3.2(d). [24]

the results of the two simulations, we extracted several line cuts of the magnetization angle ϕ, as defined in the inset of Figure 3.4(a), taken in circles about the center of the 600 nm disk. Representative line cuts with a 225 nm radius are displayed in Figure 4 as a function of angular position θ on the disk. The most important item to note from these plots is that all three cuts (experiment, uniaxial anisotropy, and coupled solution) show the same functional form for both the unstrained and strained configuration. For the unstrained state seen in Figure 3.4(a), the disk's magnetization is a circularly-symmetric vortex, and the magnetization angle varies linearly with angular position on the disk. In the strained case, as a consequence of the negative magnetoelastic response of the disk to the applied strain, magnetization in the *x*-direction (compressive direction) is favored at the expense of magnetization in the *y*-direction (tensile direction), causing the two step-like features seen in Figure 3.4(b). The plot shows that the magnetization in both the top (0°-180°) and bottom halves (180°-360°) of the disk is more uniform than in the unstrained state, i.e., the slope of the ϕ vs θ curve is shallower on the steps in Figure 3.4(b) relative to Figure 3.4(a). To be provide a better understanding of the differences between the experiment and analytical solutions we provide the following discussion. First, for the unstrained case shown in Figure 3.4(a) both the uniaxial anisotropy and coupled solutions accurately represent the Ni magnetization direction. This shows that both solutions reasonably predict the ground state of this material and selected geometry. This is reasonable because the fully-coupled system of equations should reduce to the LLG equation when no strain is applied. However, for the strained case there are distinct differences between the experiment, the uniaxial anisotropy, and the coupled solution. Specically, there is significant disagreement for the top half of the disk (i.e., 0°-180°). As shown in Figure 3.3(d), there are geometric imperfections that result in magnetic pinning effects not accounted for by either numerical model. Despite this, the coupled solution more accurately refelects the slope of the ϕ vs. θ curve of the experimental data in Figure 3.4(b). More importantly, for the lower half of the disk (i.e., 180°-36°) the coupled solution is again more accurate since it nearly matches both the measured slope of the ϕ vs. θ curve and the measured magnetization direction ϕ. The coupled elastodynamics-LLG simulation is more accurate because the strain and magnetization are coupled, such that an applied strain modifies the magnetization which in turns modifies the strain state. This is

in sharp contrast to the uniaxial anisotropy solution which only models the effect of strain on the magnetization state and neglects magnetization induced changes to the strain state. In addition to this lack of coupling, the elastodynamics-LLG solution can represent strain gradients through the volume of the disk. Inspection of Figure 3.4(b) also shows discrepancies between the experiment and both numerical solutions at 0°, 180°, and 360°. At these locations there are nearly antiparallel domain states resulting from the applied strain and this formation requires abrupt changes in magnetization direction along the diameter. These regions are unlikely to be resolved by SEMPA because of their small size and the lack of topographic contrast between areas near the edge of the disk. While the above data has shown the coupled solution is more accurate than the uniaxial anisotropy model, larger disparity with the uniaxial model is expected if a stronger magnetoelastic material such as Terfenol-D ($Tb_{0.3}Dy_{0.7}Fe_{1.92}$) were used in the study. Furthermore, greater disagreement (i.e., less accuracy of uniaxial model) between the models is also expected for geometric configurations that produce large strain gradients or are near magnetic instabilities.

To be provide a better understanding of the differences between the experiment and analytical solutions we provide the following discussion. First, for the unstrained case shown in Figure 3.4(a) both the uniaxial anisotropy and coupled solutions accurately represent the Ni magnetization direction. This shows that both solutions reasonably predict the ground state of this material and selected geometry. This is reasonable because the fully-coupled system of equations should reduce to the LLG equation when no strain is applied. However, for the strained case there are distinct differences between the experiment, the uniaxial anisotropy, and the coupled solution. Specically, there is significant disagreement for the top half of the disk (i.e., 0°-180°). As shown in Figure 3.3(d), there are geometric imperfections that result in magnetic pinning effects not accounted for by either numerical model. Despite this, the coupled solution more accurately refelects the slope of the ϕ vs. θ curve of the experimental data in Figure 3.4(b). More importantly, for the lower half of the disk (i.e., 180°-360°) the coupled solution is again more accurate since it nearly matches both the measured slope of the ϕ vs. θ curve and the measured magnetization direction ϕ. The coupled elastodynamics-LLG simulation is more

accurate because the strain and magnetization are coupled, such that an applied strain modifies the magnetization which in turns modifies the strain state. This is in sharp contrast to the uniaxial anisotropy solution which only models the effect of strain on the magnetization state and neglects magnetization induced changes to the strain state. In addition to this lack of coupling, the elastodynamics-LLG solution can represent strain gradients through the volume of the disk. Inspection of Figure 3.4(b) also shows discrepancies between the experiment and both numerical solutions at 0°, 180°, and 360°. At these locations there are nearly antiparallel domain states resulting from the applied strain and this formation requires abrupt changes in magnetization direction along the diameter. These regions are unlikely to be resolved by SEMPA because of their small size and the lack of topographic contrast between areas near the edge of the disk. While the above data has shown the coupled solution is more accurate than the uniaxial anisotropy model, larger disparity with the uniaxial model is expected if a stronger magnetoelastic material such as Terfenol-D were used in the study. Furthermore, greater disagreement (i.e., less accuracy of uniaxial model) between the models is also expected for geometric configurations that produce large strain gradients or are near magnetic instabilities.

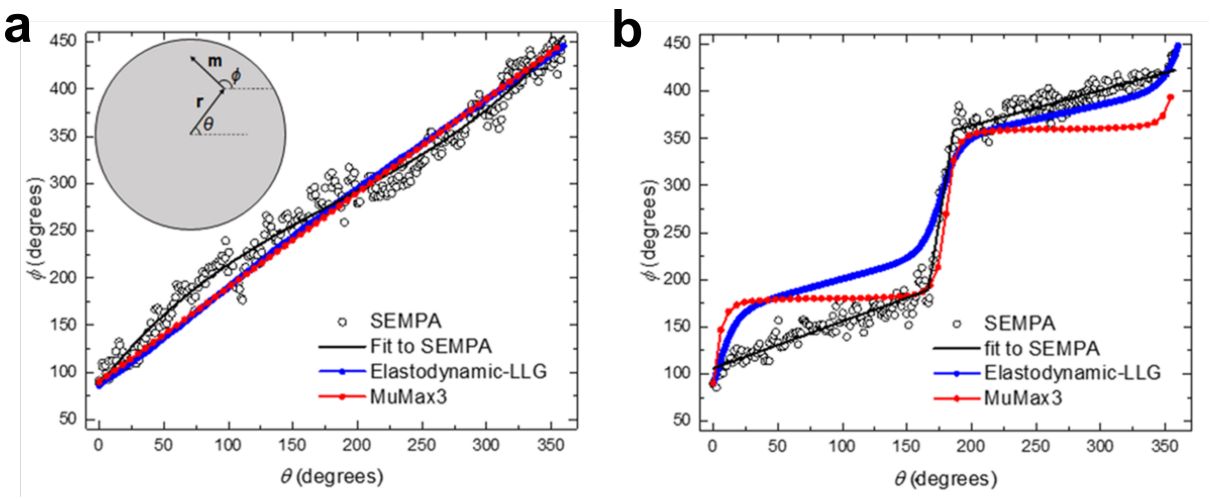

Figure 3.4: Magnetization direction as a function of angular position on the disk for the unstrained (a) and strained (b) 600 nm disks. The inset in (a) defines the angles θ and ϕ. The circular line cuts are taken at $r = 225$ nm. The black line in (a) is a 4th order polynomial fit to the SEMPA data, and the black line in (b) is a piecewise linear fit to the SEMPA data. The constant offset between the SEMPA data and the elastodyanmic-LLG simulation is due to pinning at irregularities at the disk edge, as noted in the text.[24]

3.5 Conclusion

In this section, we used SEMPA to directly image the vector magnetization of Ni structures before and after straining the underlying ferroelectric substrate and show that the magnetoelectric coupling allows the magnetization patterns to be manipulated. In particular, we demonstrate that the strain produces a uniaxial easy axis for the magnetization. For a disk initially magnetized in a vortex, the magnetization configuration is either eliminated from the disk or compressed into two antiparallel domains. These results can be successfully modeled both with basic micromagnetic simulations incorporating a spatially-uniform uniaxial anisotropy to model the strain as well as by fully-coupled micromagnetic elastodynamic simulations. However, the coupled solution more accurately captures the local effects of strain and for stronger magnetoelastic materials or operation near instabilities a fully coupled solution should be used rather than simply adding a spatially-uniform magnetic anisotropy. We anticipate that the techniques described here will be useful in the design of devices utilizing strain to control magnetization [16–19].

3.6 Chapter References

[1] S. A. Wolf, J. Lu, M. R. Stan, E. Chen, and D. M. Treger, "The promise of nanomagnetics and spintronics for future logic and universal memory", Proceedings of the IEEE **98**, 2155 (2010).

[2] I. Zutic, J. Fabian, and S. D. Sarma, "Spintronics: Fundamentals and applications", Reviews of Modern Physics **76**, 323 (2004).

[3] C. Chappert, A. Fert, and F. N. Van Dau, "The emergence of spin electronics in data storage", Nature Materials **6**, 813 (2007).

[4] A. Hoffmann and S. D. Bader, "Opportunities at the frontiers of spintronics", Physical Review Applied **4**, 1 (2015).

[5] J. Wang, J. B. Neaton, H. Zheng, V. Nagarajan, S. B. Ogale, B. Liu, D. Viehland, V. Vaithyanathan, D. G. Schlom, U. V. Waghmare, N. A. Spaldin, K. M. Rabe, M. Wuttig, and R. Ramesh, "Epitaxial BiFeO$_3$ multiferroic thin film heterostructures.", Science **299**, 1719 (2003).

[6] M. Trassin, "Low energy consumption spintronics using multiferroic heterostructures", Journal of Physics Condensed Matter **28** (2015) 10.1088/0953-8984/28/3/033001.

[7] Y.-H. Chu, L. W. Martin, M. B. Holcomb, M. Gajek, S.-J. Han, Q. He, N. Balke, C.-H. Yang, D. Lee, W. Hu, Q. Zhan, P.-L. Yang, A. Fraile-Rodríguez, A. Scholl, S. X. Wang, and R. Ramesh, "Electric-field control of local ferromagnetism using a magnetoelectric multiferroic.", Nature materials **7**, 478 (2008).

[8] J. T. Heron, J. L. Bosse, Q. He, Y. Gao, M. Trassin, L. Ye, J. D. Clarkson, C. Wang, J. Liu, S. Salahuddin, D. C. Ralph, D. G. Schlom, J. Íñiguez, B. D. Huey, and R. Ramesh, "Deterministic switching of ferromagnetism at room temperature using an electric field", Nature **516**, 370 (2014).

[9] R. Ramesh and N. A. Spaldin, "Multiferroics: Progress and prospects in thin films", Nature Materials **6**, 21 (2007).

[10] E. B. Myers, "Current-Induced Switching of Domains in MagneticMultilayer Devices", Science **285**, 867 (1999).

[11] D. C. Ralph and M. D. Stiles, "Spin transfer torques", Journal of Magnetism and Magnetic Materials **320**, 1190 (2008).

[12] F. Matsukura, Y. Tokura, and H. Ohno, "Control of magnetism by electric fields", Nature nanotechnology **10**, 209 (2015).

[13] J. Sinova, S. O. Valenzuela, J. Wunderlich, C. H. Back, and T. Jungwirth, "Spin Hall effects", Reviews of Modern Physics **87**, 1213 (2015).

[14] A. Hoffmann, "Spin hall effects in metals", IEEE Transactions on Magnetics **49**, 5172 (2013).

[15] L. Liu, O. Lee, T. Gudmundsen, D. Ralph, and R. Buhrman, "Current-induced switching of perpendicularly magnetized magnetic layers using spin torque from the spin hall effect", Physical review letters **109**, 096602 (2012).

[16] M. Buzzi, R. V. Chopdekar, J. L. Hockel, A. Bur, T. Wu, N. Pilet, P. Warnicke, G. P. Carman, L. J. Heyderman, and F. Nolting, "Single domain spin manipulation by electric fields in strain coupled artificial multiferroic nanostructures", Physical Review Letters **111**, 1 (2013).

[17] H. Sohn, M. E. Nowakowski, C. Y. Liang, J. L. Hockel, K. Wetzlar, S. Keller, B. M. McLellan, M. A. Marcus, A. Doran, A. Young, M. Kläui, G. P. Carman, J. Bokor, and R. N. Candler, "Electrically driven magnetic domain wall rotation in multiferroic heterostructures to manipulate suspended on-chip magnetic particles", ACS Nano **9**, 4814 (2015).

[18] Y. Gao, J. M. Hu, L. Wu, and C. W. Nan, "Dynamic in situ visualization of voltage-driven magnetic domain evolution in multiferroic heterostructures", Journal of Physics Condensed Matter **27** (2015) 10.1088/0953-8984/27/50/504005.

[19] A. T. Chen and Y. G. Zhao, "Research Update: Electrical manipulation of magnetism through strain-mediated magnetoelectric coupling in multiferroic heterostructures", APL Materials **4**, 1 (2016).

[20] K. Roy, S. Bandyopadhyay, and J. Atulasimha, "Switching dynamics of a magnetostrictive single-domain nanomagnet subjected to stress", Physical Review B **83**, 1 (2011).

[21] K. Roy, S. Bandyopadhyay, and J. Atulasimha, "Energy dissipation and switching delay in stress-induced switching of multiferroic nanomagnets in the presence of thermal fluctuations", Journal of Applied Physics **112** (2012) 10.1063/1.4737792.

[22] M. R. Scheinfein, J. Unguris, M. H. Kelley, D. T. Pierce, and R. J. Celotta, "Scanning electron microscopy with polarization analysis (SEMPA)", Review of Scientific Instruments **61**, 2501 (1990).

[23] Y. Zhu, *Modern techniques for characterizing magnetic materials* (Springer Science & Business Media, 2005).

[24] I. Gilbert, A. C. Chavez, D. T. Pierce, J. Unguris, W.-Y. Sun, C.-Y. Liang, and G. P. Carman, "Magnetic microscopy and simulation of strain-mediated control of magnetization in pmn-pt/ni nanostructures", Applied physics letters **109**, 162404 (2016).

[25] T. Wu, A. Bur, H. K. D. Kim, P. Zhao, and G. P. Carman, "Giant electrical control of magnetic anisotropy in magnetoelectric heterostructures using (011) PMN-PT single crystal", **7978**, 797818 (2011).

4 Voltage Induced Artificial Ferromagnetic-Antiferromagnetic Ordering in Synthetic Multiferroics

4.1 Background

Significant research interest has focused on controlling magnetism at the nanoscale [1, 2]. The motivation for many of these studies stems from non-volatile random-access memories (NVRAM) based on nanomagnetic elements. In this application space, researchers have exploited phenomena such as the spin hall effect and spin transfer torque for spintronic devices to manipulate the magnetic state of nanopatterned bits and logic elements [3–8]. Although these previous techniques offer methods for controlling nanoscale magnetism, alternatives have been sought due to the comparatively large energy dissipation associated with these mechanisms[5].

Specifically, heterogeneous multiferroic structures combining piezoelectric and magnetoelastic elements have dramatically reduced write energy dissipation by orders of magnitude in comparison to previous spintronic devices [9–11]. These multiferroic structures rely on strain transfer between the piezoelectric substrate and the magnetoelastic elements to produce magnetic state changes [12–22]. For example, the magnetization of a chain of single domain nanomagnets patterned on top of a piezoelectric substrate can be manipulated to propagate information [23–28]. This control is accomplished by combining shape anisotropy with dipole coupling between neighboring elements. In addition to controlling the magnetic state of multiferroic nanomagnets, strain has been used for altering ferromagnetic and antiferromagnetic phases in $EuTiO_3$ and the magnetic FeRh [29, 30] material. For example, researchers have been able to modify the relative proportions of antiferromagnetic and ferromagnetic phases in FeRh via voltage in-

duced strains [30, 31]. While both strain mediated magnetic manipulation of dipole coupled elements as well as changes in state have been studied, there is a relative lack of studies focused on using dipole coupled elements to transition between macroscopically antiferromagnetic and ferromagnetic states.

Here we demonstrate the voltage induced strain control of magnetism in a nanoscale array of single domain dipole-dipole coupled nanomagnets. The analytical and experimental data show a voltage induced transition between a high magnetic remanence state to a low magnetic remanence state. Discrepancies between analytical and experimental results are explained in terms of geometric defects present in the fabricated samples

4.2 Modeling and Experimental Setup

The three geometries (C1, C2, and C3) considered along with the corresponding $x-y$ coordinate system are illustrated in Figure 4.1(a) and consist of elliptical and circular nanodots separated by an edge to edge distance of 50 nm. The circular features are 100 nm in diameter and the major and minor axes of the ellipses are 135 nm and 75 nm, respectively. To evaluate the influence of fabrication defects on magnetic hysteresis, a geometric defect is added into configuration C1 as shown in Figure 4.1(b). The defect is modeled as a semicircular region located at $\theta = 30^{\circ}$ with a 10 nm radius and having a constant magnetic anisotropy (e.g., $K_d = 90$ kJ/m^3) along the [110] direction that represents magnetic pinning effects caused by imperfections in fabricated samples [19]. When an electric field of 0.8 MV/m is applied, there is a strain gradient across the elements. Since the model assumes a uniform strain distribution, the effects of strain and geometric defects are taken into account as a ratio ($\beta = K_d/K_\varepsilon$). This represents the ratio of defect anisotropy to the magnetoelastic anisotropy induced by the mechanical strain. Anisotropy ratios were studied between 2.2 and 10.2. Similar defect studies are conducted for C2 and C3 with defects included in all circular nanodots of each configuration.

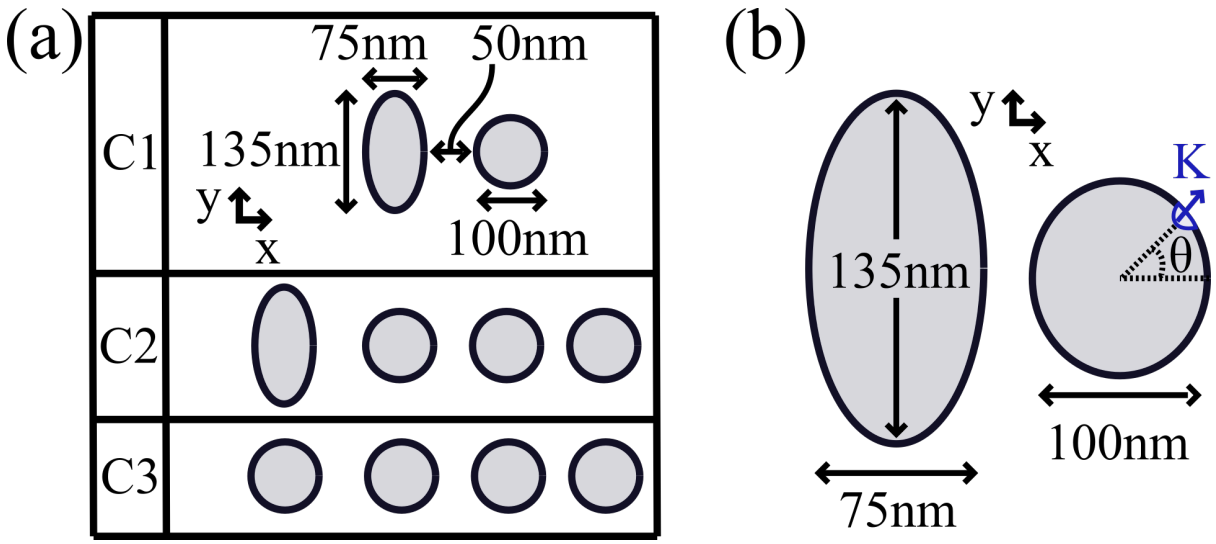

Figure 4.1: (a) Schematic of simulated magnetoelastic nanodot configuration with dimensions. (b) Illustrative example of 10 nm defect located at $\theta = 30^{\circ}$ from the chain axis for configuration 1 pinning effect hysteresis model with anisotropy directed along [110]. [32]

The numerical hysteresis curves are obtained by first applying a bias field of 600 Oe along the positive x-axis and allowing the magnetization to stabilize for 1 ns. The applied fields are then varied in 50 Oe increments for $|600\text{ Oe}| \geq H_{app} > |250\text{ Oe}|$ and varied in 10 Oe increments for $H_{app} \leq |250\text{ Oe}|$. The applied field is held constant for 0.3ns and then volume-averaged magnetization values for the configuration are recorded. The selected time steps were chosen based on convergence simulations. The nanodots are discretized in 1 nm^3 elements and the material properties used for nickel are $M_s = 4.6 \times 10^5$ A/m, $A_{ex} = 1.05x10^{-11}$ J/m, $\alpha = 0.08$, $\lambda_s = -34x10^{-6}$, and $Y = 200$ GPa. The modulus of the PMN-PT substrate is $Y_p = 140$ GPa.

Figure 4.2(a) shows the C1-C3 device profile with corresponding layer thicknesses. Fabrication consists of depositing (Au, Pt) planar electrodes on a 10mm x 10mm x 0.5mm (011) single crystal $[Pb(Mg_{1/3}Nb_{2/3})O_3]_{0.68}[PbTiO_3]_{0.32}$ (PMN-PT) substrate. This composition is chosen because it is near the morphotropic phase boundary where the piezoelectric response is largest. Following poling, the single domain Ni nanostructures are fabricated on the top surface using e-beam lithography as described in Refs. [25] & [33]. The [100] and [011] crystallographic axes of the ferroelectric substrate are aligned with the x-axis and y-axis, respectively. Figures 4.2(b)-4.2(d) show SEM micrographs of all three fabricated configurations (C1-C3). Each

configuration is fabricated in arrays covering a 1 mm^2 area and spaced 1 mm apart. In an array, each configuration has a spacing of 270 nm in the x-direction and 500 nm spacing in the y-direction. These arrays provide sufficient magnetic signal for measuring in an experimental setup. Hysteresis measurements are made for all three nanodot array configurations using

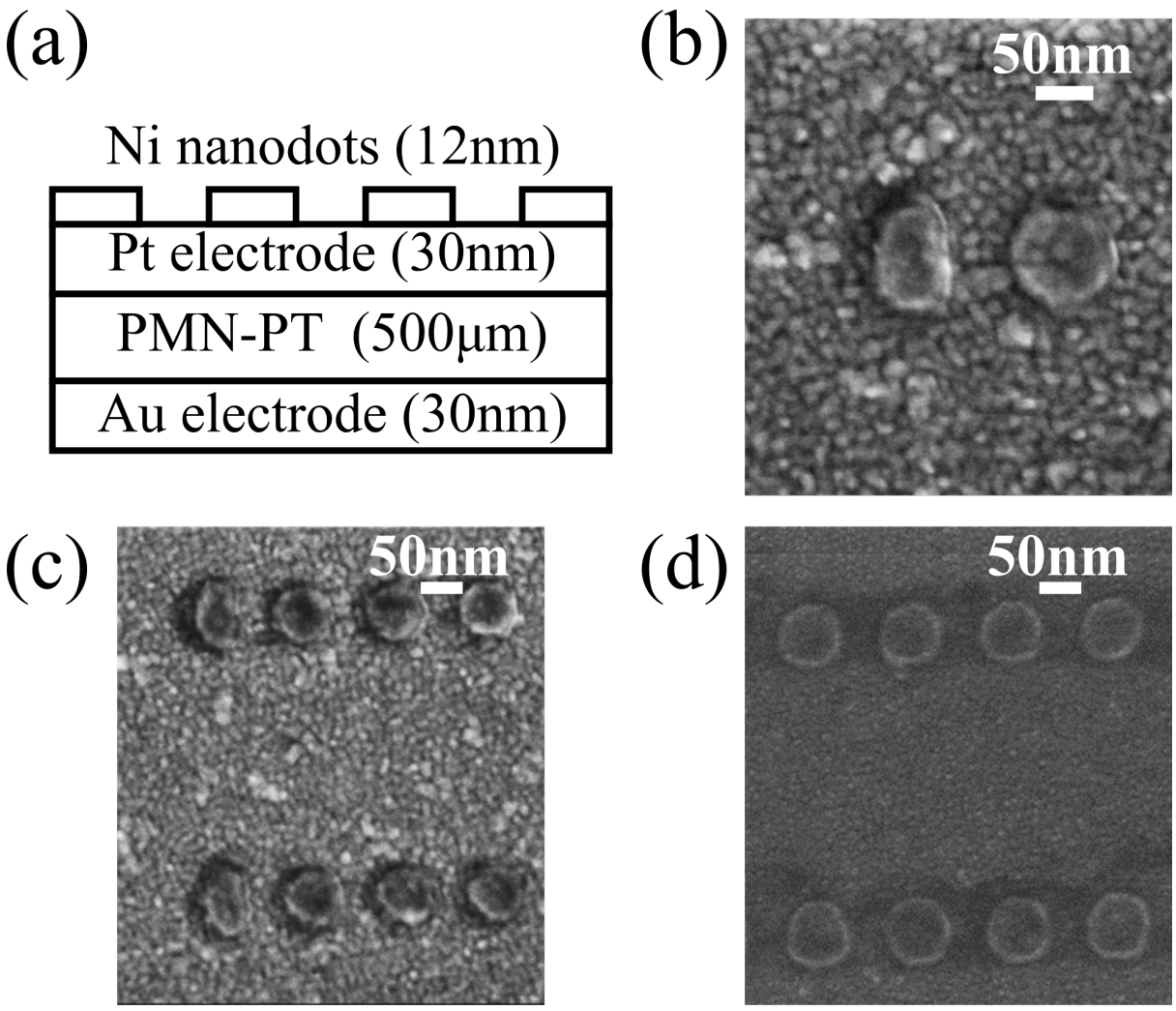

Figure 4.2: (a) Schematic of fabricated device illustrating sample materials and thicknesses. (b-d) SEM micrographs of configurations 1-3, respectively. [32]

longitudinal MOKE. The magnetic field ranges between ± 600 Oe along the x-axis in 25 Oe increments. Measurements are recorded at either 0 MV/m or 0.8 MV/m electric fields for each magnetic field value and averaged over 50 iterations. The 0.8 MV/m electric field produces in-plain anisotropic strains of $\varepsilon_x = 1200\ \mu$m/m and $\varepsilon_y = -3200\ \mu$m/m [33]. The magnetization data is recorded using a standard lock-in technique and the measured data represents an average magnetic response of the nanodot array 9.

4.3 Results

Numerically and experimentally generated hysteresis curves, with bias fields applied along the x-axis, are presented for C1-C3 at $E = 0$ MV/m and $E = 0.8$ MV/m. Simulated curves are presented first followed by magnetization curves measured with MOKE magnetometry. Lastly, numerically generated hysteresis curves accounting for fabrication defects are given to explain differences between modeled and measured values.

Figures 4.3(a)-4.3(c) provide modeled hysteresis curves along the x-axis of C1-C3 for $E = 0$ MV/m (unstrained) and $E = 0.8$ MV/m (strained) cases. Without electric field the magnetic remanence and coercive field values are ($Mr = 0.48$, $Hc = 50$ Oe) for C1, ($Mr = 0.75$, $Hc = 100$ Oe) for C2, and ($Mr = 1.00$, $Hc = 350$ Oe) for C3. Applying an electric field of 0.8 MV/m reduces the remanence and coercive field values to zero for all three configurations. The increasing trend of Mr and Hc values for C1-C3 when $E = 0$ MV/m, are explained by

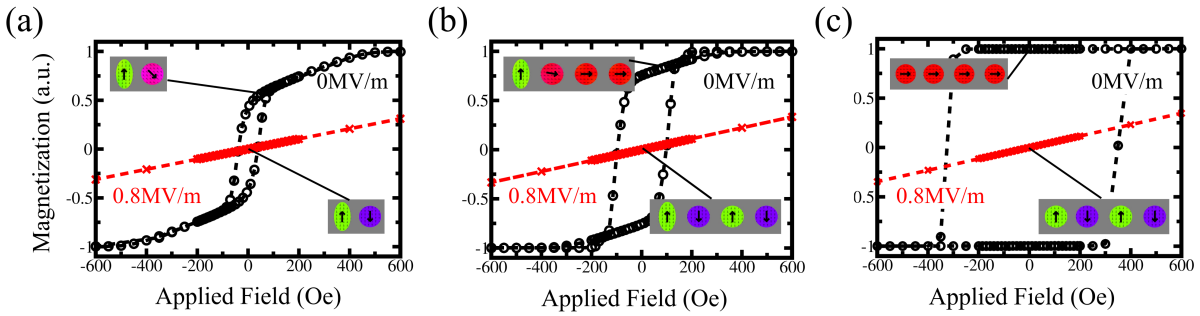

Figure 4.3: (a)-(c) Magnetization curves determined from micromagnetics simulations of configurations 1-3 for both 0 MV/m (unstrained) and 0.8 MV/m (strained) applied electric fields. [32]

shape anisotropy and dipole coupling between the nanodots. At saturation, dipole coupling between the nanodots favors magnetization alignment along the x-axis for all configurations. However, when the field is withdrawn, C1, C2 and C3 behave differently. Figure 4.3(c) shows that dipole coupling between the nanodots maintains parallel magnetization alignment (i.e., artificial ferromagnetic ordering) along the x-axis when $H_{app} = 0$ Oe. The magnetization of C2 does not completely align along the x-axis when $H_{app} = 0$ Oe because the shape anisotropy of

the ellipse causes its magnetization to lie along the y-axis for this field. Consequently, dipole coupling causes the magnetization of its nearest circular nanodot to rotate towards the y-axis. However, dipole coupling between the remaining circular nanodots limits this rotation resulting in the semi-artificial ferromagnetic state of Figure 4.3(b). Similarly, the magnetization of the ellipse in C1 lies along the y-axis for $H_{app} = 0$ Oe and, through dipole coupling, causes rotation of the circular dot's magnetization. As shown in Figure 4.3(a), the rotation angle is greater in C1 compared to C2 because there is only one circular feature. That is, the additional dipole coupling of the extra circular nanodots in C2 is not present in C1, hence the ellipse exerts greater influence on the nanodot of C1. The remanence values for C1-C3 indicate that the x-axis is magnetically hardest for C1 and easiest for C3, thus explaining the increase in Hc from C1-C3 when no electric field is applied. The models thus show that nanostructures can be used to achieve artificial ferromagnetic behavior that is tunable by the choice of geometry.

Magnetoelastic effects explain the reduction of M_r and H_c to zero for all configurations when $E = 0.8$ MV/m (i.e., strain is applied). The application of an electric field generates a compressive piezoelectric strain along the y-axis. The voltage induced magnetoelastic anisotropy of the Ni nanodots in all configurations favors magnetization alignment along the compressive axis (i.e., y-axis) because Ni is negatively magnetostrictive. In C3 magnetoelastic effects combine with dipole coupling to cause antiparallel alignment of the nanodot magnetizations as shown in the insets of Figure 4.3 (i.e., artificial antiferromagnetic ordering). For C2 and C1, the shape anisotropy of the ellipses, in addition to the magnetoelastic response of the nanodots, combine with dipole coupling to cause the observed complete antiparallel magnetization alignment. In contrast to the unstrained ($E = 0$ MV/m) configurations, C1-C3 do not saturate at an applied field of 600 Oe for $E = 0.8$ MV/m because the bias field is insufficient to overcome the combination of magnetoelastic, shape, and dipole effects. This indicates that the added magnetoelastic anisotropy causes the x-axis to become magnetically very hard resulting in zero coercive field and zero remanence values for all configurations. Compared with the unstrained case, these results show a voltage induced transition from artificial ferromagnetic ordering (parallel alignment) to artificial antiferromagnetic ordering (antiparallel alignment) using patterned

nanostructures.

Figures 4.4(a)-4.4(c) present hysteresis curves, measured by longitudinal MOKE magnetometry, for the C1-C3 device at applied electric fields of 0 MV/m and 0.8 MV/m. The applied magnetic bias fields are applied along the x-axis and vary between ± 600 Oe. Without mechanical strains (i.e., $E = 0$ MV/m) the remanence and coercive field values are ($M_r = 0.43$, $H_c = 36$ Oe) for C1, ($M_r = 0.73$, $H_c = 40$ Oe) for C2, and ($M_r = 0.87$, $H_c = 45$ Oe) for C3. Figures 4.4(a)-4.4(c), show that when and electric field of 0.8 MV/m is applied, the measured magnetic remanence and coercive field values are (0.16, 34 Oe) for C1, (0.22, 38 Oe) for C2, and (0.24, 45 Oe) for C3. The overall trends in remanence and coercive field values of the ex-

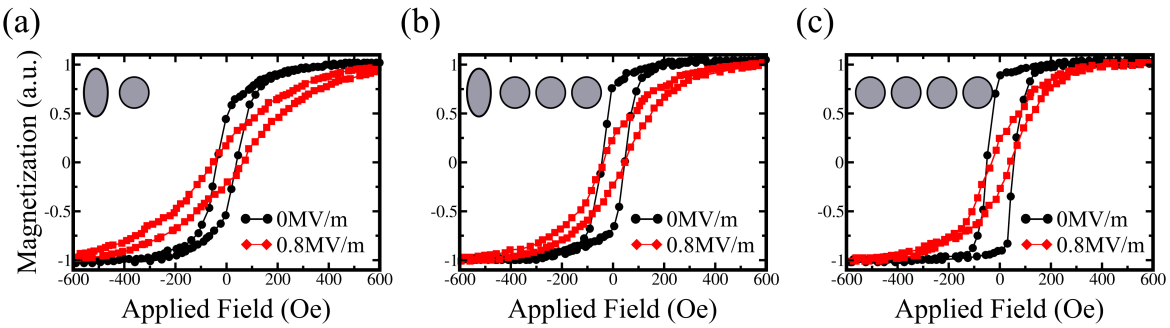

Figure 4.4: Magnetization curves measured using MOKE magnetometry for both unstrained (0 MV/m) and strained cases (0.8 MV/m). (a) M-H loop of configuration 1. (b) M-H loop of configuration 2. (c) M-H loop of configuration 3. [32]

perimental data for $E = 0$ MV/m are similar to the simulations, but there are some differences. Specifically, the remanence and coercive field values increase from C1-C3 in accordance with the micromagnetics model. However, the measured M_r and H_c values are different from the numerical solutions. Also, in contrast to theory, the measured data indicates that the x-axis is magnetically harder in C3 than C2. This can be explained with two assumptions about the magnetization of the nanodots. First, assume that the magnetization of the ellipse in C2 completely aligns along the y-axis at $H_{app} = 0$ Oe. Secondly, assume that each of the four nanodots in C2 and C3 account for one fourth of the total magnetization in each configuration. Consequently, without a bias field only the circular nanodots of C2 and C3 contribute to M_r so that that maximum possible remanence values of these configurations are 0.75 and 1.0, respectively.

Based on these assertions, the measured data suggest that 0.74/0.75=99% of the nanodots in C2 remain pointed along the x-axis at $H_{app} = 0$ while 0.87/1.0=87% of the circular nanodots of C3 point in this direction for the same field. These results suggest the presence of geometric defects since they pin the magnetization of the nanodots.

Applying a 0.8 MV/m electric field to the sample reduces the remanence and coercive field values for all configurations, but these reductions are lower than simulation predictions. In particular, the simulations suggest that Mr of each configuration should reduce to a similar value (i.e., $M_r = 0$). The measurements show this Mr decrease, however the remanence values are much higher ($M_r \approx 0.20$). Additionally, the simulations show that Hc should reduce to 0 Oe for C1-C3, but the measured values only slightly decrease from the unstrained state (i.e., $E = 0$ MV/m). Imperfections arising during fabrication of nanostructures have been shown to limit the rotation of device magnetization14. Hence, the measured data suggests that similar pinning sites are present in the sample and are responsible for the device response in both the presence and absence of electric fields. Although the measured data does not show switching from artificial antiferromagnetic to artificial ferromagnetic ordering, it does show a reduction in Mr from the unstrained state ($E = 0$ MV/m) to the strained state ($E = 0.8$ MV/m), as predicted by the model.

Figures 4.5(a)-4.5(c) present numerically generated hysteresis curves of C1-C3 which contain semicircular defects and aid in the explanation of discrepancies between the measured and simulated data. For the case of $E = 0.8$ MV/m, the non-uniform strain distribution and effect of geometrical defects are taken into account as a ratio ($\beta = K_d/K_\varepsilon$) of the defect anisotropy to the equivalent anisotropy of applied mechanical strain for $2.2 \leq \beta \leq 10.2$. The defects are located on the periphery of all circular nanodots at $\theta = 30^\circ$ for C1-C3. The remanence and coercive field values from the defect models for $E = 0$ MV/m are in close agreement with experiment and produce $M_r = [0.44, 0.74, 0.82]$ and $H_c = [39, 47, 50]$Oe for C1, C2, and C3, respectively. For the strained cases (i.e., β cases), closest agreement, with M_r and H_c, to experiment was obtained with $\beta = 10.2$. The corresponding remanence and coercivity values were

$Mr = [0.06, 0.12, 0.11]$ and $H_c = [25, 25, 40]$Oe for C1-C3. The accuracy in determining M_r

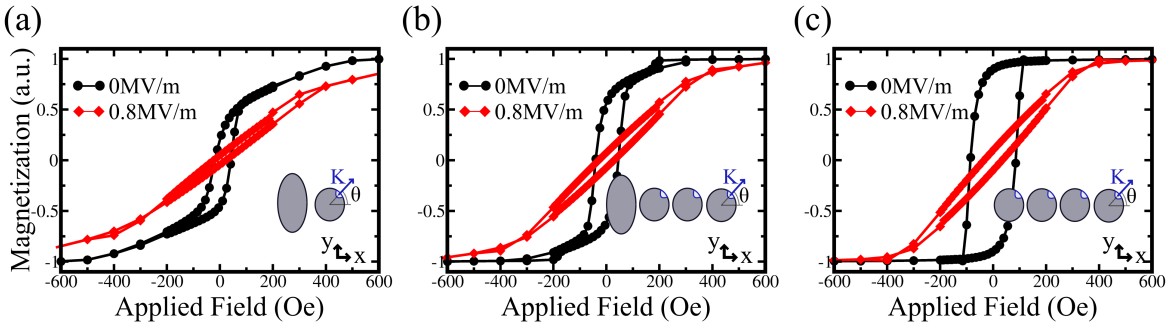

Figure 4.5: Simulation results demonstrating the influence circular defects have on the magnetization curves of the nanodots arrays. (a-c) Magnetization curves of configurations 1-3, respectively. [32]

and H_c by simulation of strain-based nanostructure devices is improved by accounting for fabrication defects in the model using localized regions of constant magnetic anisotropy directed along a fixed axis. When defects are included in the $E = 0$ MV/m models, the simulation error in M_r is reduced from 11%, 2.7%, 14% to 2.2%, 1.3%, 6% for C1, C2, C3. Additionally, the simulation error in H_c is reduced from 28%, 60%, 87% to 7.7%, 15%, 10% for C1, C2, C3. This improvement is achieved because the defect produces, through the exchange interaction, local regions favoring inclination away from the x-axis. For C3 this causes a portion of the volume in each nanodot to misalign with the x-axis thereby decreasing the magnetic remanence of C3 relative to the simulations without defects. Furthermore, since these local regions make the x-axis less energetically favorable, the nanodots can be demagnetized with lower applied fields resulting in a reduction of coercive field for C3. Similar effects are seen in C2 and C1 resulting in better prediction of Mr and Hc values. The strong agreement between the measured values and defect simulations for $E = 0$ MV/m suggest that pinning sites are present in the sample. Furthermore, the presence of defects would lead to significant strain gradients making the assumption of uniform strain distributions highly inaccurate and thus responsible for the severe disagreement between simulation and measured values for $E = 0.8$ MV/m. Although the defect studies for an applied strain are not as well matched as the unstrained studies, they provide further evidence for geometric defects causing discrepancies between measured and modeled hysteresis loops.

4.4 Conclusion

In this section, three configurations of patterned multiferroic nanostructures were proposed for producing transitions between artificially produced antiferromagnetic and ferromagnetic states. This functionality has been demonstrated numerically, but not experimentally validated, and there is quantitative disagreement between model and experiment. The quantitative differences are related to geometric defects present in the fabricated samples and when these artifacts are accounted for, there is relatively good quantitative agreement, in M_r and H_c, between simulations and experiment but these pinning sites prevent complete transitions between artificial antiferromagnetic and artificial ferromagnetic magnetic arrangement. This demonstration and understanding of the role that defects play in strain mediated electrical nanoscale devices can lead to more effective control of magnetism with potential application for nanoscale motors or nanomanipulation.

4.5 Chapter References

[1] J. Shen and J. Kirschner, "Tailoring magnetism in artificially structured materials : the new frontier", **500**, 300 (2002).

[2] S. a. Wolf, D. D. Awschalom, R. a. Buhrman, J. M. Daughton, S. von Molnár, M. L. Roukes, a. Y. Chtchelkanova, and D. M. Treger, "Spintronics: a spin-based electronics vision for the future.", Science (New York, N.Y.) **294**, 1488 (2001).

[3] J. Slonczewski, "Current-driven excitation of magnetic multilayers", Journal of Magnetism and Magnetic Materials **159**, L1 (1996).

[4] J. Z. Sun, "Spin-current interaction with a monodomain magnetic body: A model study", Physical Review B **62**, 570 (2000).

[5] J. A. Katine, F. J. Albert, R. A. Buhrman, E. B. Myers, and D. C. Ralph, "Current-driven magnetization reversal and spin-wave excitations in Co/Cu/Co pillars", Physical Review Letters **84**, 3149 (2000).

[6] L. Liu, C.-f. Pai, Y. Li, H. W. Tseng, D. C. Ralph, and R. A. Buhrman, "Spin-Torque Switching with the Giant Spin Hall Effect of Tantalum", Science **336**, 555 (2012).

[7] D. Bhowmik, L. You, and S. Salahuddin, "Spin hall effect clocking of nanomagnetic logic without a magnetic field", Nature Nanotechnology **9**, 59 (2014).

[8] Z. Diao, Z. Li, S. Wang, Y. Ding, A. Panchula, E. Chen, L. C. Wang, and Y. Huai, "Spin-transfer torque switching in magnetic tunnel junctions and spin-transfer torque random access memory", Journal of Physics Condensed Matter **19** (2007) 10.1088/0953-8984/19/16/165209.

[9] A. K. Biswas, S. Bandyopadhyay, and J. Atulasimha, "Complete magnetization reversal in a magnetostrictive nanomagnet with voltage-generated stress: A reliable energy-

efficient non-volatile magneto-elastic memory", Applied Physics Letters **105** (2014) 10.1063/1.4893617.

[10] K. Roy, S. Bandyopadhyay, and J. Atulasimha, "Hybrid spintronics and straintronics : A magnetic technology for ultra low energy computing and signal processing", Applied Physics Letters **99**, 1 (2016).

[11] K. Roy, S. Bandyopadhyay, and J. Atulasimha, "nanomagnets in the presence of thermal fluctuations Energy dissipation and switching delay in stress-induced switching of multiferroic nanomagnets in the presence of thermal fluctuations", Journal of Applied Physics **112** (2012) 10.1063/1.4737792.

[12] N. D'Souza, J. Atulasimha, and S. Bandyopadhyay, "Four-state nanomagnetic logic using multiferroics", Journal of Physics D: Applied Physics **44** (2011) 10.1088/0022-3727/44/26/265001.

[13] N. A. Pertsev and H. Kohlstedt, "Resistive switching via the converse magnetoelectric effect in ferromagnetic multilayers on ferroelectric substrates", Nanotechnology **21** (2010) 10.1088/0957-4484/21/47/475202.

[14] N. Tiercelin, Y. Dusch, A. Klimov, S. Giordano, V. Preobrazhensky, and P. Pernod, "Room temperature magnetoelectric memory cell using stress-mediated magnetoelastic switching in nanostructured multilayers", Applied Physics Letters **99**, 1 (2011).

[15] T. Brintlinger, S. H. Lim, K. H. Baloch, P. Alexander, Y. Qi, J. Barry, J. Melngailis, L. Salamanca-Riba, I. Takeuchi, and J. Cumings, "In situ observation of reversible nanomagnetic switching induced by electric fields", Nano Letters **10**, 1219 (2010).

[16] J. M. Hu, T. Yang, J. Wang, H. Huang, J. Zhang, L. Q. Chen, and C. W. Nan, "Purely electric-field-driven perpendicular magnetization reversal", Nano Letters **15**, 616 (2015).

[17] A. Bur, T. Wu, J. Hockel, C. J. Hsu, H. K. Kim, T. K. Chung, K. Wong, K. L. Wang, and G. P. Carman, "Strain-induced magnetization change in patterned ferromagnetic nickel nanostructures", Journal of Applied Physics **109** (2011) 10.1063/1.3592344.

[18] T. K. Chung, S. Keller, and G. P. Carman, "Electric-field-induced reversible magnetic single-domain evolution in a magnetoelectric thin film", Applied Physics Letters **94**, 1 (2009).

[19] J. Cui, C. Y. Liang, E. A. Paisley, A. Sepulveda, J. F. Ihlefeld, G. P. Carman, and C. S. Lynch, "Generation of localized strain in a thin film piezoelectric to control individual magnetoelectric heterostructures", Applied Physics Letters **107** (2015) 10.1063/1.4930071.

[20] C. Y. Liang, A. Sepulveda, S. Keller, and G. P. Carman, "Deterministic switching of a magnetoelastic single-domain nano-ellipse using bending", Journal of Applied Physics **119** (2016) 10.1063/1.4944650.

[21] C. Y. Liang, S. M. Keller, A. E. Sepulveda, W. Y. Sun, J. Cui, C. S. Lynch, and G. P. Carman, "Electrical control of a single magnetoelastic domain structure on a clamped piezoelectric thin film - Analysis", Journal of Applied Physics **116** (2014) 10.1063/1.4896549.

[22] J. Cui, J. L. Hockel, P. K. Nordeen, D. M. Pisani, C. Y. Liang, G. P. Carman, and C. S. Lynch, "A method to control magnetism in individual strain-mediated magnetoelectric islands", Applied Physics Letters **103** (2013) 10.1063/1.4838216.

[23] M. S. Fashami, K. Munira, S. Bandyopadhyay, A. W. Ghosh, S. Member, J. Atulasimha, and S. Member, "Switching of Dipole Coupled Multiferroic Nanomagnets in the Presence of Thermal Noise: Reliability of Nanomagnetic Logic", IEEE Transactions on Magnetics **12**, 1206 (2013).

[24] M. S. Fashami, K. Roy, J. Atulasimha, and S. Bandyopadhyay, "Magnetization dynamics, Bennett clocking and associated energy dissipation in multiferroic logic", Nanotechnology **22**, 155201 (2011).

[25] M. Salehi-Fashami, M. Al-Rashid, W.-Y. Sun, P. Nordeen, S. Bandyopadhyay, A. C. Chavez, G. P. Carman, and J. Atulasimha, "Binary information propagation in circular magnetic nanodot arrays using strain induced magnetic anisotropy", Nanotechnology **27**, 43LT01 (2016).

[26] J. Atulasimha and S. Bandyopadhyay, "Bennett clocking of nanomagnetic logic using multiferroic single-domain nanomagnets", Applied Physics Letters **97**, 2008 (2010).

[27] K. Roy, "clocking in the presence of thermal fluctuations Critical analysis and remedy of switching failures in straintronic logic using Bennett clocking in the presence of thermal fluctuations", Applied Physics Letters **104** (2014) 10.1063/1.4858484.

[28] K. Roy, S. Bandyopadhyay, and J. Atulasimha, "Switching dynamics of a magnetostrictive single-domain nanomagnet subjected to stress", Physical Review B **83**, 1 (2011).

[29] J. H. Lee, L. Fang, E. Vlahos, X. Ke, Y. W. Jung, L. F. Kourkoutis, J.-w. Kim, P. J. Ryan, T. Heeg, M. Roeckerath, V. Goian, M. Bernhagen, J. W. Freeland, R. Uecker, P. C. Hammel, K. M. Rabe, S. Kamba, D. A. Muller, C. J. Fennie, P. Schiffer, V. Gopalan, E. Johnston-halperin, and D. G. Schlom, "A strong ferroelectric ferromagnet created by means of spin – lattice coupling", Nature Letters **466** (2010) 10.1038/nature09331.

[30] Y. Lee, Z. Q. Liu, J. T. Heron, J. D. Clarkson, J. Hong, C. Ko, M. D. Biegalski, U. Aschauer, S. L. Hsu, M. E. Nowakowski, J. Wu, H. M. Christen, S. Salahuddin, J. B. Bokor, N. A. Spaldin, D. G. Schlom, and R. Ramesh, "Large resistivity modulation in mixed-phase metallic systems", Nature Communications, 1 (2015).

[31] X. Marti, I. Fina, C. Frontera, J. Liu, P. Wadley, Q. He, R. J. Paull, J. D. Clarkson, J. Kudrnovský, I. Turek, J. Kuneš, D. Yi, J. H. Chu, C. T. Nelson, L. You, E. Arenholz, S.

Salahuddin, J. Fontcuberta, T. Jungwirth, and R. Ramesh, “Room-temperature antiferromagnetic memory resistor”, Nature Materials **13**, 367 (2014).

[32] A. C. Chavez, W.-Y. Sun, J. Atulasimha, K. L. Wang, and G. P. Carman, “Voltage induced artificial ferromagnetic-antiferromagnetic ordering in synthetic multiferroics”, Journal of Applied Physics **122**, 224102 (2017).

[33] I. Gilbert, A. C. Chavez, D. T. Pierce, J. Unguris, W. Y. Sun, C. Y. Liang, and G. P. Carman, “Magnetic microscopy and simulation of strain-mediated control of magnetization in PMN-PT/Ni nanostructures”, Applied Physics Letters **109** (2016) 10.1063/1.4965028.

5 Deterministic Switching of Dipole Coupled Nanoellipses

5.1 Background

Magnetoelectric heterostructures with deterministic magnetization reorientation offer a new approach to nanoscale devices such as memory and nanomotors [1–3]. Deterministic control refers to controlling the direction of magnetization rotation in a repeatable manner. This requires the breaking of symmetry in the magnetic energy profile together with a mechanism to control the magnetization energy landscape. There are multiple mechanisms that can be used to drive magnetization reorientation in magnetic heterostructures. These include application of an external magnetic field, injection of spin current, changing the magnetic dipole interactions with neighboring structures, and using strain to change the magnetoelastic energy [4, 5]. Among these the latter, in the form of strain-coupled magnetoelectric heterostructures, has been shown to be the most energy efficient [6]. Strain-coupled magnetoelectric heterostructures are composite structures with thin magnetoelastic materials on top of piezoelectric substrates. When voltage is applied to the piezoelectric substrate, an in-plane strain is generated. This strain couples to the magnetoelastic material, driving magnetization reorientation.

The design of magnetoelectric heterostructures with deterministic switching behavior requires control of the various contributions to the magnetic energy anisotropy. These include the magnetocrystalline anisotropy, external magnetic field (Zeeman), magnetization gradient (exchange), magnetoelastic, and shape (magnetostatic) anisotropy [7]. The magnetocrystalline anisotropy energy is associated with the crystal structure, with some materials displaying an easy axis and a hard axis of magnetization associated with various crystallographic directions. The Zeeman Energy is associated with the energy produced from an external magnetic field of any origin. The exchange energy is associated with the interaction energy between two mag-

netic moments within a material. Exchange energy is a quantum effect that acts over short distances (equivalent to the exchange length of the material) between neighboring magnetic spins. The magnetoelastic energy is associated with magnetostriction where strain modifies the magnetic energy profile, inducing easy and hard directions of magnetization. The shape anisotropy (demagnetization energy) is the energy associated with the internal magnetic field opposing the direction of magnetization within the magnetic element. Shape anisotropy can also induce easy and hard directions. The effective magnetic field at a point is found by taking the partial derivative of the magnetic energy with respect to magnetization. This effective field produces a torque on the local magnetic moments, driving them to rotate toward the direction that minimizes their energy in the effective field.

The symmetric shape anisotropy of an ellipse, with an easy direction along the major axis and hard direction along the minor axis, can be changed with applications of anisotropic energies of different origins. The application of in-plane strain to a magnetoelastic ellipse can rotate the easy direction away from the major axis. If the magnetoelastic constant of a material, λ_s, is positive, the direction of a uniaxial tensile stress component becomes easier to magnetize. Similarly, if λ_s is negative, the direction of a uniaxial compressive stress component becomes easier to magnetize [7]. This effect is enhanced when the stress state is biaxial with orthogonal tensile and compressive stress components. In a magnetoelectric heterostructure, this stress is induced by coupling to the strain produced by an electric field in a piezoelectric. When the principal strain components align with the major and minor axes of the ellipse, and are of sufficient magnitude and have the correct sign to make the minor axis become the easy axis, the magnetization will rotate a full 90° in either a clockwise or counter-clockwise direction [8]. To achieve deterministic switching, the symmetry of the magnetic energy must be broken. Several methods have been proposed to accomplish this in strain-mediated multiferroic heterostructures, generally leading to complex nanomagnet geometries and electrode configurations. Among these are a four-fold-symmetry nanomagnet1 and a “cat-eye” geometry [9]. Fabrication of these structures with complicated geometries and patterned electrodes with multiple leads can be more difficult than fabrication of the proposed three nanoellipse structure and

requires a complex control strategy to drive the magnetization reorientation.

Several methods have been developed to obtain deterministic control of magnetization rotation. Patterned electrodes can be used to sequentially rotate the strain for deterministic control. This requires a complicated control mechanism since each pair of electrode must be actuated in sequence [1, 9, 10]. A simpler control mechanism was proposed by Li et al. for 180° out-of-plane magnetization switching [11]. This method, known as strain-mediated ballistic switching, takes advantage of magnetization dynamics. Magnetization has angular momentum, and thus undergoes damped precession about the direction of an effective magnetic field when the field undergoes a sudden change. Ballistic switching was extended by Peng et al. [12] to in-plane 180° magnetization switching using two electrodes and a single short voltage pulse. A finite element simulation was used to demonstrate strain-mediated ballistic switching in a single CoFeB ellipse on a PZT thin film. The magnetization in the ellipse was initially aligned with the positive x-axis ($m_x = 1$) parallel to the major axis of the ellipse with the y-axis aligned with the minor axis. Two electrodes perpendicular to the x-axis were actuated and produced approximately 1100 ppm in-plane tensile strain along the ellipse y-axis. The y-axis, with tensile strain large enough to overcome the demagnetization energy, became the new easy axis of magnetization for the CoFeB element. The tensile strain drove the magnetization to precess about the y-axis. The voltage induced strain was released when mx was between the 0 and -1. With the strain removed, damped precession began with the magnetization moving about the negative x-direction and damped to 180° from its original configuration. This simpler control mechanism requiring only a single voltage pulse is implemented in the three-ellipse geometry discussed below.

Design of the geometry to enable control of the magnetization dynamics of the three ellipse configuration was performed in two steps. First, simulations were performed using a conventional micromagnetics finite difference code without strain coupling. The conventional micromagnetics simulation was used to create the initial geometry of the three ellipse structure. The uncoupled micromagnetics model assumes uniform strain, therefore neglecting the strain

variations present in the magnetoelastic material [13]. Next, simulations were performed using a finite element code with coupled micromagnetics, elastodynamics, and linear piezoelectric constitutive behavior to assess the magnetization dynamics associated with the geometry and effects of strain gradients across the structure.

5.2 Micromagnetics Model and Parametric Sweeps

Previous simulations of a magnetic tunnel junction described in the literature indicated that properly positioning side magnetic elements can help reduce the energy needed to produce magnetization reorientation in the central element; however, no size ranges were provided [14]. Here, initial values of geometric parameters for a three-ellipse design were obtained using the conventional micromagnetics code of Section 2.2. The three-ellipse geometry is defined in Figure 5.1a. The major and minor axes of the three ellipses, a_0, b_0, a_1 and b_1 and the angle ϕ were varied with θ fixed at 45° to obtain geometries in which the magnetization of the outer ellipses would drive magnetization rotation in the inner ellipse. Figure 5.1 displays results from one of these simulations in which the magnetization of the outer ellipses was able to drive reorientation of the magnetization of the inner ellipse. The magnetization in the inner ellipse was initialized in the positive y-direction and the magnetizations in the outer ellipses were initialized along their major axes at 45°. The micromagnetics code was then run to obtain the stable magnetization state. The equilibrium magnetization state of this system is shown in Figure (1b). The magnetization in the outer ellipses was then reinitialized and held fixed at -45° (5.1c) and the micromagnetics code was run again to obtain the stable equilibrium state. The desired result was the 180° magnetization rotation in the central ellipse shown (5.1d). The geometry in Figure (5.1a) gives a potential design, but it is challenging to achieve with current fabrication capabilities since the three ellipses are in contact. To obtain a refined three ellipse design, feature sizes were varied within the range of available fabrication techniques. Electron beam lithography processes that can be used for fabrication of such a device can produce patterns on the order of 30 nm with a tolerance of ± 5 nm. Resolutions as low as 10

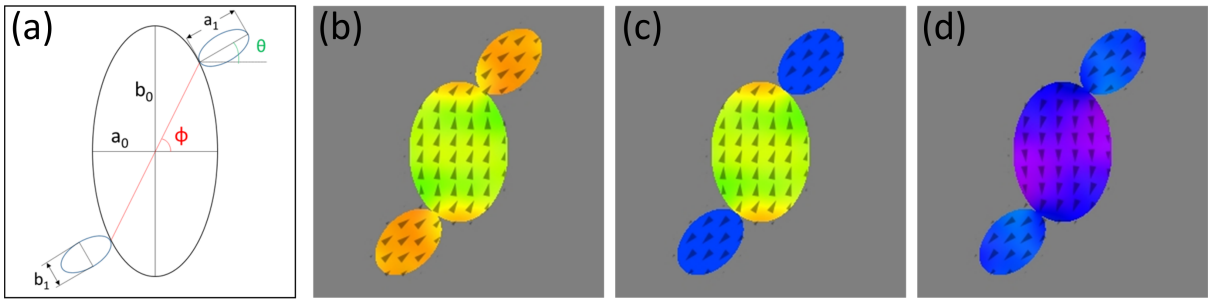

Figure 5.1: (a) Example geometry of the three-ellipse design (b) Magnetization configuration of the three-ellipse design after 1 ns using a conventional micromagnetics code. (c) Magnetization in the outer ellipses was switched 180°. (d) The final configuration indicates 180° magnetization switching in the inner ellipse. [15]

nm with a tolerance of ± 2 nm can be achieved with further processing steps, these include processing at low temperatures (~ 2°C) [16, 17]. A minimum ellipse dimension of 50 nm was chosen with a separation distance of 15 nm between any two ellipses to account for fabrication tolerances. The final dimensions of the inner and outer ellipses were $a0 = 95$ nm, $b0 = 125$ nm, $a1 = 75$ nm, and $b1 = 50$ nm. Each ellipse was 4 nm thick. θ and ϕ were chosen to be 45° and 70° respectively.

Next, strain-mediated ballistic switching was simulated using the conventional micromagnetics code that does not directly include magnetoelastic energy terms. The effects of mechanical strains were modeled indirectly by applying time varying uniaxial anisotropies within each ellipse. Strains were converted to magnetic anisotropies using $K_u = 1.5\lambda_s E(\varepsilon_x - \varepsilon_y)$ for implementation in the micromagnetics software [7]. K_u is the uniaxial anisotropy constant, E is the Young's Modulus of the material, and $(\varepsilon_x - \varepsilon_y)$ represents the average in-plane strain of each ellipse. In previous models of Ni/PZT multiferroic heterostructures with perpendicular magnetization reversal, large and unrealistic biaxial strains of up 13,000 ppm in the 100 nm PZT substrate were used to drive magnetization reorientation [18]. In this study, we applied strains as high as 5000 ppm along the minor axis of each outer ellipse to induce ballistic switching in these ellipses. This will need to be further reduced if PZT is used as the piezoelectric layer, but this strain level can be achieved with single crystal PMN-PT [19]. This preliminary geometry was next assessed using the fully coupled finite element model.

5.3 Fully-coupled Model

The fully-coupled model of section 2.3 was used to assess the effects of strain and magnetization gradients on the magnetization dynamics of the three-ellipse design chosen from the parametric sweeps presented in Section 5.2. Specifically, the fully-coupled simulations were performed with a geometry that included the piezoelectric substrate and conductive electrodes. In this geometry, the three CoFeB ellipses were positioned on a 700 nm x 700 nm x 500 nm PZT-5H substrate. The Gilbert damping constant, magnetic saturation, exchange constant, elastic constants, and magnetostrictive coefficient of CoFeB used in the model were [20–24] $\alpha = 0.0120$-22, $M_s = 1 \times 10^6$ [A/m]12, $A_{ex} = 1.5 \times 10^{-11}$ [J/m]12, $c_{11} = 2.8 \times 10^{11}$ [N/m^2] 12, $c_{12} = 1.4 \times 10^{11}$ [N/m^2] 12, $c_{44} = 0.7 \times 10^{11}$ [N/m^2] 12, $\lambda_s = 110 \times 10^{-6}$23-24. A pair

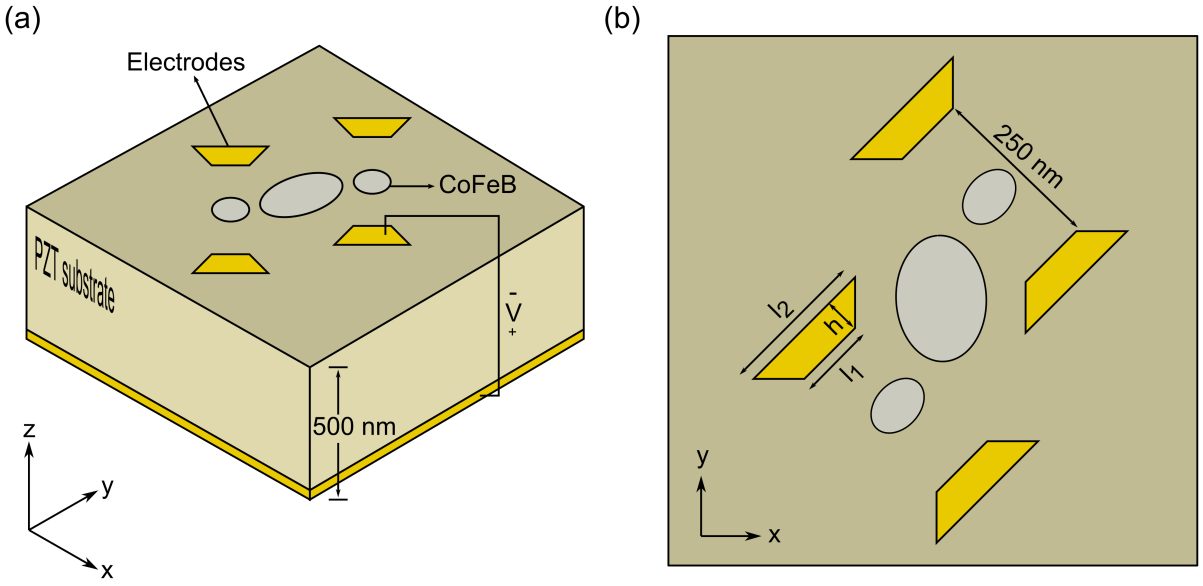

Figure 5.2: (a) Isometric view (b) Top view of three ellipse configuration and electrodes used in fully-coupled finite element simulations. [15]

of electrodes was placed on either side of each smaller ellipse, with 250 nm separation between each electrode. These electrodes were shaped as trapezoids with the dimensions $l_1 = 75$ nm, $l_2 = 150$ nm, and $h = 50$ nm. Figure (5.2b) is a top view of the geometry used in the fully-coupled finite element model. Low reflecting boundary conditions were applied to the four edges of the PZT substrate to simulate infinite width. This boundary condition eliminated wave reflections within the substrate. The top of the substrate was free to displace in the z-

direction. The displacements at the bottom surface were fixed such that $u_1 = u_2 = u_3 = 0$. The bottom surface of the substrate was the ground plane. Voltage was applied to the trapezoidal electrodes on the top surface. A tetrahedral mesh was used for the PZT substrate. The magnetic elements used a swept triangular mesh. The largest mesh size in the magnetic domain was set according to the exchange length of CoFeB which is 4.9 nm. The exchange length is given by $l_{ex} = \sqrt{\frac{2A_{ex}}{\mu_0 M_s^2}}$ [25]. Thus, the maximum mesh size used in the model was 5 nm to capture the exchange effects.

The magnetization in each ellipse was initially aligned in the positive y-direction and allowed to relax to steady state for 1ns before the pulsed voltage was applied. A series of 7.3V pulses was applied to each electrode. This is well below the breakdown electric field of 25 MV/m for PZT thin films [12]. This pulse was applied for 0.22ns at an interval of 4ns between each pulse to achieve 360° rotation. The pulse produced an average tensile strain along the minor axis of 4,400 ppm in the outer ellipses and 1,800 ppm in the inner ellipse. Although previous devices using thin film PZT have been proposed using larger strains values, strains above 1,800 ppm in thin film PZT are not possible to achieve. Other piezoelectric substrates must be considered for fabrication and testing of this device. However, for a proof of concept of a deterministic magnetization rotation, we considered strains as high at 5,000 ppm. Figure 5.3 illustrates the input voltage pulse applied to the electrodes and the corresponding in-plane strain it produced in each ellipse.

5.4 Results

The strain-induced magnetic response of the three ellipse heterostructure is discussed below. First, the temporal response predicted by the conventional micromagnetics formulation is given. Second, the results of the fully-coupled model are presented. The differences in the device behavior predicted by the two different modeling approaches is then discussed.

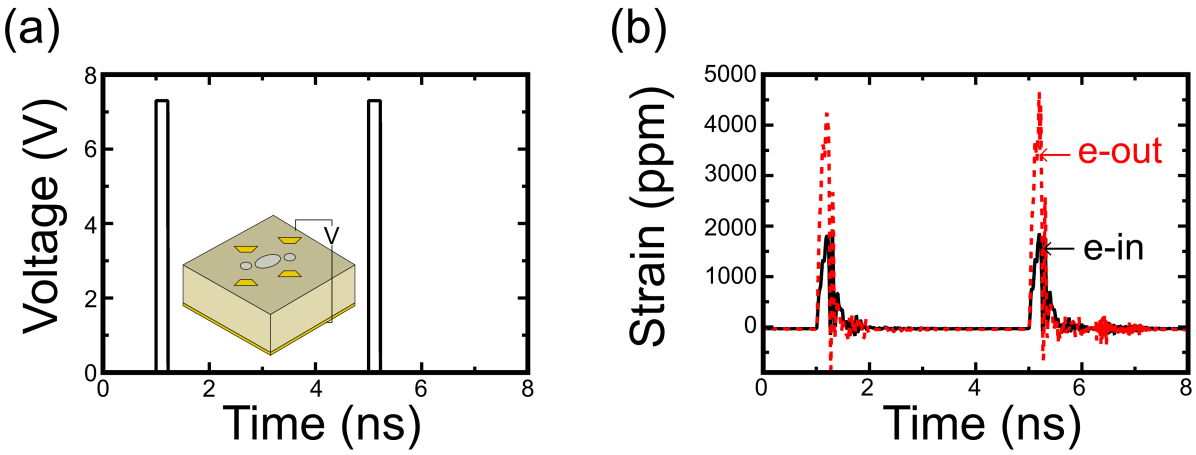

Figure 5.3: (a) Input voltage pulses (b) Voltage pulse induced average strain response of inner and outer ellipses. [15]

The conventional micromagnetics simulation did not produce 180° ballistic switching of the outer ellipses when they were subjected to a 1 ns duration change in magnetic anisotropy equivalent to that produced by the strain pulse in the fully-coupled model. Consequently, the magnetization of the inner ellipse could not be rotated 360º without reinitializing the magnetization in the outer ellipses. The magnetization of the outer ellipses rotated a maximum of 115° with respect to the horizontal x-axis in response to the anisotropy change while the inner ellipse's magnetization rotated 50° degrees clockwise. For full 180° degrees switching of the outer ellipses, the magnetization must rotate past 135° degrees with the application of strain. These results indicate that uniaxial strain induced anisotropy changes could not overcome the dipole coupling between the three ellipses that favors parallel alignment of their magnetization

In the fully-coupled model, 360° magnetization switching of the inner ellipse was achieved by two consecutive 180° ballistic switches of the two outer ellipses as seen in Figures 5.4a and 5.4b. The magnetization of the inner ellipse completed its first 180° switch (1 to -1) in 1.6 ns while the outer ellipses achieved 180° reorientation in 1.3 ns. Given a wave speed of approximately 4000 m/s in PZT-5H, reorientation of the inner ellipse is expected to begin approximately 30ps after the initial voltage is applied. Figure 5.4b indicates that the magnetization of the outer ellipses begin to rotate at $t = 1.03$ ns while the magnetization of the inner ellipse starts rotating at $t = 1.08$ ns. This difference indicates magnetic reorientation

of the inner ellipse was driven by the effective field (i.e., dipole coupling) produced from the magnetization configuration of the outer ellipses. Hence, when the outer ellipses are switched ballistically, magnetic reorientation of the inner ellipse occurs due to the effective field of the side ellipses. This effective field is a result of the magnetization distribution within each ellipse. The internal magnetization and the effective magnetic field it produces is dependent on the aspect ratio of each ellipse. The effective field of each ellipse element was approximated using the field of a magnetic dipole. By simplifying the three ellipse design to a three dipole system, the torque exerted by the outer ellipses results in counterclockwise rotation of the inner ellipse's magnetization. The difference in predicted behavior between the two models is due

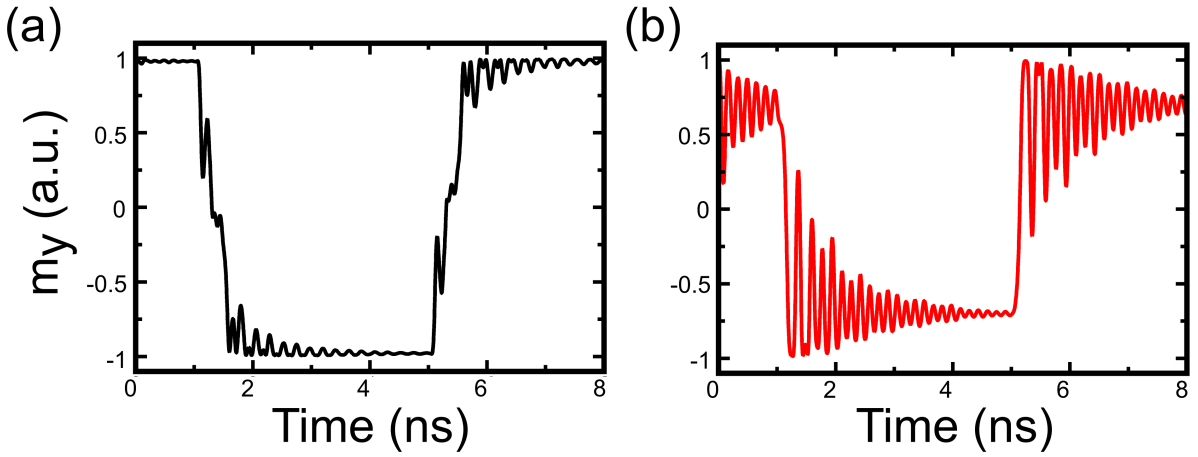

Figure 5.4: (a) m_y of the inner ellipse demonstrating 360° ballistic switching in fully-coupled model. (b) m_y of magnetization in one of the outer ellipses. [15]

to non-uniform strain distributions that are captured only by the fully coupled model. In the simplified micromagnetics model, the uniaxial anisotropy within the ellipses fails to capture these strain gradients. Consequently 360° magnetic switching of the inner ellipse is demonstrated by the fully-coupled model, but not found using the micromagnetics simulation. In the fully coupled model, all three ellipses are subjected to time dependent compressive and tensile strains. The non-uniform strain distribution is the result of the interaction of mechanical waves within the substrate that arise from having two pairs of electrodes actuated simultaneously. The non-uniform distribution creates multiple hard and easy axes of magnetization inside the inner ellipse which makes rotations easier. This variation in strain helps drive magnetization rotation of the inner ellipse after reorientation in the smaller ellipses.

5.5 Conclusion

In this section, A conventional micromagnetics simulation and a fully-coupled finite element model was used to simulate a three ellipse heterostructure capable of 360° deterministic magnetization rotation in a new multiferroic heterostructure. The heterostructure was composed of three CoFeB nanoellipses layered on top of a PZT thin film. In the micromagnetics model, the strain in each was simulated as a uniaxial anisotropy along the minor axis of each ellipse. The outer ellipses and larger ellipse were simulated with uniaxial strains of 5000 ppm and 1800 ppm strain respectively. In this simplified simulation, the magnetization within the three ellipses did not rotate 360°. Instead, the magnetization stayed in its original configuration and no rotations were observed in the structure. In the fully-coupled model, the magnetization of the larger ellipse underwent 360° counterclockwise rotation after ballistic switching of the outer ellipses. The magnetization of the outer ellipses was switched using a 7.3 V pulse applied for 0.22 ns to cause 180° rotation. Then an identical second pulse was applied to create full 360° rotation. The voltage pulses produced a tensile strain along the minor axis of each ellipse. The larger and smaller ellipses experienced strains of approximately 1800 ppm and 4400 ppm respectively. This demonstrates the necessity of having a fully-coupled simulation to accurately predict the behavior of multiferroic heterostructures, especially in the dynamic regime. The strain gradients that occur in the physical device are not captured by the simplified approximation of the micromagnetics model. The fully-coupled finite element model better predicts the magnetization dynamics in multiferroic heterostructures.

5.6 Chapter References

[1] C. Y. Liang, A. E. Sepulveda, D. Hoff, S. M. Keller, and G. P. Carman, "Strain-mediated deterministic control of 360 domain wall motion in magnetoelastic nanorings", Journal of Applied Physics **118** (2015) 10.1063/1.4934196.

[2] J. J. Wang, J. M. Hu, J. Ma, J. X. Zhang, L. Q. Chen, and C. W. Nan, "Full 180° magnetization reversal with electric fields", Scientific Reports **4**, 1 (2014).

[3] S. Cherepov, P. Khalili Amiri, J. G. Alzate, K. Wong, M. Lewis, P. Upadhyaya, J. Nath, M. Bao, A. Bur, T. Wu, G. P. Carman, A. Khitun, and K. L. Wang, "Electric-field-induced spin wave generation using multiferroic magnetoelectric cells", Applied Physics Letters **104** (2014) 10.1063/1.4865916.

[4] W. Eerenstein, N. D. Mathur, and J. F. Scott, "Multiferroic and magnetoelectric materials.", Nature **442**, 759 (2006).

[5] J. M. Hu, Z. Li, J. Wang, and C. W. Nan, "Electric-field control of strain-mediated magnetoelectric random access memory", Journal of Applied Physics **107** (2010) 10.1063/1.3373593.

[6] K. Roy, S. Bandyopadhyay, and J. Atulasimha, "Switching dynamics of a magnetostrictive single-domain nanomagnet subjected to stress", Physical Review B **83**, 1 (2011).

[7] R. C. O'handley, *Modern magnetic materials: principles and applications* (Wiley, 2000).

[8] M. Buzzi, R. V. Chopdekar, J. L. Hockel, A. Bur, T. Wu, N. Pilet, P. Warnicke, G. P. Carman, L. J. Heyderman, and F. Nolting, "Single domain spin manipulation by electric fields in strain coupled artificial multiferroic nanostructures", Physical Review Letters **111**, 1 (2013).

[9] J. Cui, S. M. Keller, C.-y. Liang, G. P. Carman, and C. S. Lynch, "Nanoscale magnetic ratchets based on shape anisotropy", Nanotechnology **28** (2017).

[10] A. K. Biswas, H. Ahmad, J. Atulasimha, and S. Bandyopadhyay, "Experimental Demonstration of Complete 180° Reversal of Magnetization in Isolated Co Nanomagnets on a PMN-PT Substrate with Voltage Generated Strain", Nano Letters **17**, 3478 (2017).

[11] X. Li, D. Carka, C. Y. Liang, A. E. Sepulveda, S. M. Keller, P. K. Amiri, G. P. Carman, and C. S. Lynch, "Strain-mediated 180° perpendicular magnetization switching of a single domain multiferroic structure", Journal of Applied Physics **118** (2015) 10.1063/1.4923350.

[12] R.-C. Peng, J.-M. Hu, K. Momeni, J.-J. Wang, L.-Q. Chen, and C.-W. Nan, "Fast 180° magnetization switching in a strain-mediated multiferroic heterostructure driven by a voltage", Scientific Reports **6**, 27561 (2016).

[13] I. Gilbert, A. C. Chavez, D. T. Pierce, J. Unguris, W. Y. Sun, C. Y. Liang, and G. P. Carman, "Magnetic microscopy and simulation of strain-mediated control of magnetization in PMN-PT/Ni nanostructures", Applied Physics Letters **109** (2016) 10.1063/1.4965028.

[14] L. Leem and J. S. Harris, "Magnetic coupled spin-torque devices for nonvolatile logic applications", Journal of Applied Physics **105** (2009) 10.1063/1.3056141.

[15] A. A. Kundu, A. C. Chavez, S. M. Keller, G. P. Carman, and C. S. Lynch, "360° deterministic magnetization rotation in a three-ellipse magnetoelectric heterostructure", Journal of Applied Physics **123**, 104105 (2018).

[16] L. E. Ocola and A. Stein, "Effect of cold development on improvement in electron-beam nanopatterning resolution and line roughness", Journal of Vacuum Science & Technology B: Microelectronics and Nanometer Structures **24**, 3061 (2006).

[17] W. (Hu, K. Sarveswaran, M. Lieberman, and G. H. Bernstein, "Sub-10 nm electron beam lithography using cold development of poly(methylmethacrylate)", Journal of Vacuum Science & Technology B: Microelectronics and Nanometer Structures **22**, 1711 (2004).

[18] J. M. Hu, T. Yang, J. Wang, H. Huang, J. Zhang, L. Q. Chen, and C. W. Nan, "Purely electric-field-driven perpendicular magnetization reversal", Nano Letters **15**, 616 (2015).

[19] H. Sohn, M. E. Nowakowski, C. Y. Liang, J. L. Hockel, K. Wetzlar, S. Keller, B. M. McLellan, M. A. Marcus, A. Doran, A. Young, M. Kläui, G. P. Carman, J. Bokor, and R. N. Candler, "Electrically driven magnetic domain wall rotation in multiferroic heterostructures to manipulate suspended on-chip magnetic particles", ACS Nano **9**, 4814 (2015).

[20] S. Iihama, S. Mizukami, H. Naganuma, M. Oogane, Y. Ando, and T. Miyazaki, "Gilbert damping constants of Ta/CoFeB/MgO(Ta) thin films measured by optical detection of precessional magnetization dynamics", Physical Review B - Condensed Matter and Materials Physics **89**, 1 (2014).

[21] M. Oogane, T. Wakitani, S. Yakata, R. Yilgin, Y. Ando, A. Sakuma, and T. Miyazaki, "Magnetic damping in ferromagnetic thin films", Japanese Journal of Applied Physics, Part 1: Regular Papers and Short Notes and Review Papers **45**, 3889 (2006).

[22] G. Malinowski, K. C. Kuiper, R. Lavrijsen, H. J. M. Swagten, and B. Koopmans, "Magnetization dynamics and Gilbert damping in ultrathin Co48Fe32B20 films with out-of-plane anisotropy", Applied Physics Letters **94**, 102501 (2009).

[23] G. A. Lebedev, B. Viala, T. Lafont, D. I. Zakharov, O. Cugat, and J. Delamare, "Converse magnetoelectric effect dependence with CoFeB composition in ferromagnetic/piezoelectric composites", Journal of Applied Physics **111** (2012) 10.1063/1.3679443.

[24] T. Lafont, L. Gimeno, J. Delamare, G. A. Lebedev, D. I. Zakharov, B. Viala, O. Cugat, N. Galopin, L. Garbuio, and O. Geoffroy, "Magnetostrictive-piezoelectric composite structures for energy harvesting", Journal of Micromechanics and Microengineering **22** (2012) 10.1088/0960-1317/22/9/094009.

[25] G. S. Abo, Y. K. Hong, J. Park, J. Lee, W. Lee, and B. C. Choi, "Definition of magnetic exchange length", IEEE Transactions on Magnetics **49**, 4937 (2013).

6 Voltage Control of Magnetic Monopoles in Artificial Spin Ice

6.1 Background

Spurred by Pauling's prediction of proton disorder in water ice, spin ices have been widely studied as geometrically frustrated magnetic systems [1–4]. An interesting feature of these materials are quasi-particle magnetic monopoles present in $Ho_2Ti_2O_7$ and $Dy_2Ti_2O_7$ [5–8]. Studies have shown that these monopoles can be manipulated to create magnetic currents analogous to modern electronics which utilize electric charge for storing or propagating information [9–11]. Studying these monopole states is challenging because the relevant phenomena occur at cryogenic temperatures and are sensitive to lattice mismatch between substrate and spin ice crystal [2, 9–11]. To overcome some of these technological challenges, researchers have begun to focus on artificial spin ice (ASI) systems [12–16]. ASI's are lithographically patterned magnetic single domain structures arranged in lattice geometries that are leveraged to create synthetic magnetic monopoles. Pioneering experiments in square and Kagome lattice ASI's have established the presence of magnetic monopoles [12, 17–20]. Stochastic monopole nucleation and movement in ASI's has been achieved by application and subsequent reversal of an externally applied saturating magnetic field [17, 19–22]. Monopole dynamics have been probed through extensive cascade type experiments revealing quenched disorder and freedom from thermal fluctuations [23–25]. Further studies revealed hysteretic memory effects in square lattices following training magnetic field cycles [26]. Although repeatable microstates are achievable, the initial configuration and subsequent limit cycles are stochastically determined. This external field control is problematic since manipulation of magnetic current in ASI's requires individual control of the single magnetic domain structures. Thus, a new approach to manipulate single domain structures in ASI systems is needed for future technological application. One approach that warrants consideration, to overcome present stochastic ASI

control, is strain-mediated multiferroic heterostructures. These multiferroic composites combine present-day piezoelectric and magnetoelastic materials to efficiently control nanoscale magnetism [27, 28]. Magnetic control is achieved using voltage-induced piezoelectric strain within patterned magnetoelastic elements [28–31]. Nanopatterned structures resembling the magnetic islands in ASI lattices have been studied on arrays of magnetically dipole-coupled elements with Bennett clocking [32, 33]. The Bennett clocking approach utilizes strain-induced magnetoelastic effects, shape anisotropy, and dipole coupling between neighboring elements to propagate logical information across a lattice. Additionally, numerical and experimental studies have demonstrated strain-induced 180° precessional magnetic switching [34–37]. In this paper, numerical modeling demonstrates magnetic monopole control within a Kagome lattice through switching of the central nodal element using magnetoelastic strain.

6.2 Model Setup

Our design for controlling magnetic monopoles in a Kagome lattice-based ASI consists of elliptical magnetoelastic islands on a piezoelectric substrate. This design uses voltage induced strains in the piezoelectric layer to control local magnetization states. The magnetoelastic structures, and the relevant dipolar interactions between them, are numerically studied with the Landau-Lifshitz-Gilbert (LLG) micromagnetics formulation of Section 2.2. The model neglects thermal fluctuations, but room temperature material properties are used, and the model assumes small elastic deformations as well as uniform strains within the magnetoelastic elements [30, 38].

In this paper, a four ring multiferroic Kagome lattice ASI containing a monopole was modeled as shown in Figure 6.1. As seen from the figure, the modeled system is a subset of an infinite Kagome lattice and contains four hexagonal unit cells with a monopole centrally located. Per convention, the dumbbell charge model is used to identify monopoles in an ASI by replacing magnetic dipole moments with two charges ($\pm Q$). Specifically, lattice sites in a Kagome ASI

exhibiting $\pm 3Q$ are defined as monopoles. Equivalently an ASI monopole in a Kagome lattice is denoted as a vertex site with the magnetization of three elliptical elements directed into $(+3Q)$ or out $(-3Q)$ of the vertex. The present study assumes the influence of elements beyond the four unit-cells are negligible, so the modeled magnetization switching of the strained central ellipse element f_o, as seen in Figure 6.1, is representative of an infinite lattice. This set of neighboring elements exert the greatest influence on f_o and the resulting dipolar effects on the strain-induced magnetic response can only be captured through simulation of multiple islands. Specifically, it is not possible to know that f_o can switch 180° within the lattice from a simulation of a single ellipse because the dipolar interactions are unknown a priori. Along these lines, the details of the magnetization dynamics (e.g., $\theta \sim \text{atan}[m_y/m_x]$) depend on the dipole coupling between neighboring elements for each modeled ASI. The simulated lattice is shown schematically with the hexagonal rings labeled I-IV and the center of each elliptical magnetic island labeled with f_i, r_i, or q_i. The ASI initial magnetization state is chosen with the monopole located at the f_o-r_o-q_3 vertex. Thus, movement of the monopole results from 180° switching of f_o's magnetization so that the magnetization of f_o, r_3, q_o are directed into their common vertex. The ellipse dimensions were chosen based on a parametric sweep in a micromagnetic simulation focusing on geometries likely to give uniform single domain structures. Ellipses with major axes ranging from 120 nm to 60 nm of 0.8 aspect ratios were tested via a parametric sweep of element dimensions. Larger geometries were favored since they will be easier to fabricate in future experiments. The choice of the 0.8 aspect ratio was motivated by Ref [35], in which successful strain-induced precessional motion was demonstrated. Both larger and smaller aspect ratios were also considered, but small aspect ratios (e.g., 0.2) make strain-induced switching very difficult due to large shape-derived energy wells, whereas larger ratios (i.e., 1) create thermally unstable ellipses. Based on these results from the parametric sweep, ellipses with major axes of 100 nm, minor axes of 80 nm, and 3 nm thickness were selected. Per convention, the thermal stability factor at room temperature of modern MRAM devices is set to 40KbT [39, 40]. For the materials and geometry chosen, the shape anisotropy of the CoFeB, Ni, and FeGa ellipses are 61KbT, 47KbT, and 82KbT, respectively. The parametric sweep also informed our choice of the separation distance between adjacent elliptical

lattice elements, d, which was set to be 25nm, as shown in Figure 6.1. All models used in the parametric sweeps and dynamic studies, which will be presented in the results section, used cuboidal finite-difference-time-domain mesh elements with volumes of 1 nm^3. This volume was chosen as a result of convergence studies. To study dynamic switching of the monopole

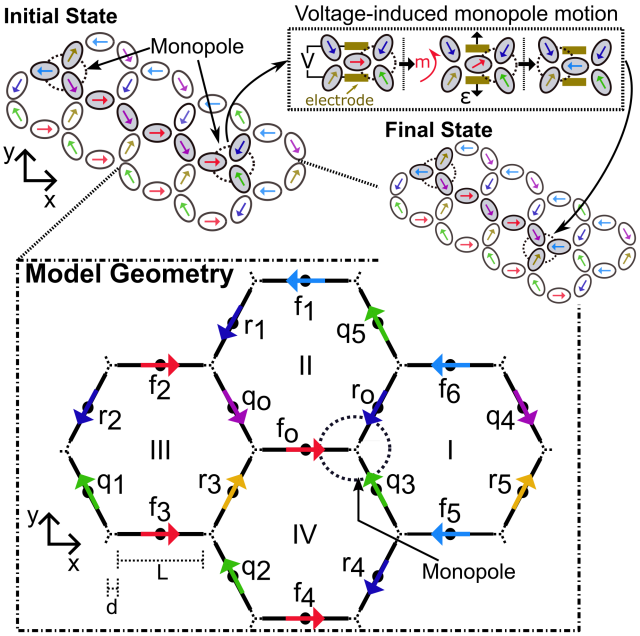

Figure 6.1: (a) Schematic illustrating monopole defect motion in Kagome ASI caused by voltage-induced strain. Inset shows the initial magnetic orientation of the four rings modeled with a monopole defect located at f_o-r_o-q_3 vertex. [41]

location within the ASI, precessional magnetic switching of the single domain elliptical magnetoelastic structures was used. This precessional switching was achieved by applying a highly localized voltage-induced strain pulse to a single central ellipse, f_o, in the ASI unit cell, in a direction parallel to the minor axis of the ellipse. To confirm that such strain localization is feasible, a finite element study was done to calculate the voltage-controlled strain distribution across the ASI lattice and piezoelectric substrate. The finite element results indicate that the switching strains can be localized to a single ellipse, and nearest neighbors experience, at most, 6% of the threshold switching strain. These results validate the assumption used in our micromagnetic simulation that strains can be localized to an ASI's individual elements. To better represent voltage-induced strain in a working device, the localized strain pulse was ramped linearly to its maximum value. Experimental and numerical studies have demonstrated precessional switching with 70 ps rise/release times of piezostrain. Additional theoretical investiga-

tions have suggested that this ramp time can be further reduced by optimizing the electrode geometry, electronics, and piezoelectric film thickness [32, 34–37]. Based on this, the voltage-controlled strain pulses used in this study were programmed to reach a maximum value after 10 ps following a linear ramp function, and they were removed following the same function with a negative slope.

Three magnetoelastic materials were chosen to be included in this modeling study; namely CoFeB, Ni, and FeGa. CoFeB was chosen because of its relatively large saturation magnetization and magnetostriction [37, 42]. Ni was chosen because it is widely studied and is one of the easiest magnetoelastic material to fabricate [27, 28, 38]. FeGa is chosen for its high magnetoelastic properties which reduce the energy requirements to precessionally switch the single domain elements [43]. The CoFeB and Ni systems are assumed to be polycrystalline with grain sizes much smaller than the exchange length, which allows the MCA to be neglected [37]. The FeGa (19% Ga) is assumed to be single crystal, as the large magnetoelastic response of interest is absent in polycrystalline films [43, 44]. The material properties used for simulation are given in Table 6.1 [37, 38, 42–45]. Note, the crystalline anisotropy constants K_{c1} and K_{c2} are aligned along the $< 1,0,0 >$ and $< 1,1,0 >$ directions, respectively. The relevant piezoelectric coefficients of PMN-PT for producing the modeled strain values are found in Ref [46]. A combination of micromagnetic parametric studies and piezoelectric finite element models were used to determine suitable strains, pulse widths, and electric fields for achieving precessional switching of the modeled magnetic elements. The biaxial strain values and pulse widths chosen for CoFeB, Ni, and FeGa were 1600 ppm (0.425 ns), 1600 ppm (0.35 ns), and 2400 ppm (0.27 ns) which correspond to 4.8 MV/m, 4.8 MV/m, and 7.2 MV/m electric fields produced by the electrodes in Figure 6.1, respectively. The duration of the pulse is critical for achieving precessional switching. For the present study, it was found that $\pm$0.03 ns, $\pm$0.03 ns, and $\pm$0.02 ns per pulse width was allowable to achieve precessional switching for CoFeB, Ni, and FeGa respectively.

Table 6.1: Material Properties for Multiferroic Artificial Spin Ice

Material	M_s (A/m)	A_{ex} (J/m)	α	λ_s (ppm)	Y (GPa)	K_{c1} (J/m^3)	K_{c2} (J/m^3)
CoFeB	1.2×10^{6}	1.9×10^{-11}	0.01	50	160	0	0
Ni	4.8×10^{5}	1.05×10^{-11}	0.045	-34	200	0	0
FeGa	1.3×10^{6}	1.4×10^{-11}	0.04	100	140	1.5×10^{4}	-0.7×10^{5}

6.3 Results

Figures 6.2(a)-(c) show strain-induced motion of a monopole defect from the f_o-r_o-q_3 vertex to the f_o-r_3-q_o vertex in a CoFeB ASI. Figures 6.2(a)-(b) show the initial ($t = 0$ ns) and final ($t = 3.5$ ns) stable magnetic states after strain is applied to f_o at $t = 1$ ns. The final state in 6.2(b) shows that the monopole defect was moved from the f_o-r_o-q_3 vertex to the f_o-r_3-q_o vertex, as evidenced by the 180° rotation of f_o from its initial orientation. The figure also shows that f_o's neighboring lattice elements (both near and far) remain magnetized in their initial direction following strain application. Figure 6.2(c) provides the rotation angle (θ) as a function of time for f_o and its nearest neighbors (q_o, r_3, r_o, and q_3) where the magnetization is taken as a volume average over all the magnetic moments of the ellipse. The non-nearest neighbors are excluded because their magnetization angles are perturbed less than $\pm5°$. In particular, Fig 6.2(c) shows f_o's magnetization begins to rotate clockwise at $t = 1.21$ ns. The rotation rate slows slightly at $t = 1.4$ ns, but continues until the magnetization reaches $-180°$ at $t = 1.52$ ns. After $t = 1.53$ ns, f_o overshoots $-180°$ and reaches a maximum rotation angle of $-222°$ at $t = 1.6$ ns before settling along the $-x$ direction of the ellipse. During the same time, f_o's nearest neighbors remain directed along their initial orientations while experiencing oscillations of less than $\sim 22°$. The largest orientation variation for these elements is exhibited by r_3 whose magnetization varies between 71° and 50° before settling back to its equilibrium orientation at 60°. When strain is applied to the central element, f_o, of the CoFeB ASI, precessional magnetic switching from 0° to $-180°$ occurs near the ferromagnetic resonance (FMR) frequency of the ellipse. A Fast Fourier transform of the response produces a FMR value of 3.12 GHz with a switching time of 0.32 ns. This FMR value matches closely to the 3.16 GHz FMR predicted by

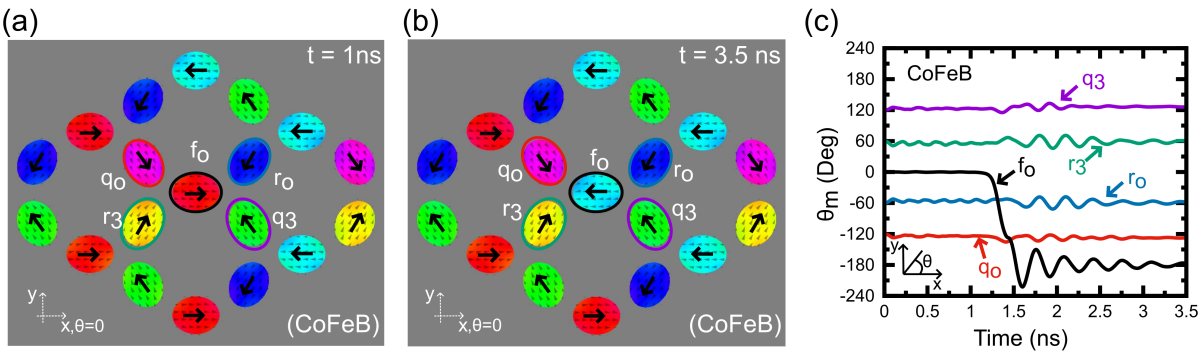

Figure 6.2: (a) Magnetic state of CoFeB ASI after relaxing for 1 ns. (b) Final state of CoFeB ASI after application of strain pulse. (c) Time variation of x-component of magnetization for central magnetic island and nearest neighbors. [41]

Kittel's equation:

$$\omega = \gamma \sqrt{\left(H_{eff} + \mu_0 \left(N_x - N_y\right) M_y\right) \left(H_{eff} + \mu_0 \left(N_z - N_y\right) M_y\right)} \tag{6.1}$$

where the effective field is the sum of the mechanical and demagnetization fields. The small difference between the calculated and simulated resonances are attributed to the spatial non-uniformity of the dipolar interactions between f_o and its nearest neighbors in the numerical simulation. In comparison to an isolated ellipse, the symmetric placement of f_o's nearest neighbors makes its major axis magnetically easier during the first 90° of rotation due to the combination of neighbor-derived dipolar and internal shape effects. This positioning raises the energy barrier to rotate f_o's magnetization because any rotation is met with a restoring torque (back towards $\theta = 0$) resulting from nearest neighbor dipolar interactions and internal shape effects. Despite this, the magnetoelastic effects in CoFeB under strain are sufficient to overcome this restoring torque, and push f_o towards a strain-induced easy axis at $\theta = -90°$, as shown in Figure 2(c). As f_o moves to this new easy axis via precessional motion, it is underdamped, and overshoots $\theta = -90°$. However, once the magnetization rotates past $-90°$, the restoring magnetoelastic torque slows the continued rotation, but this effect vanishes because the timed strain pulse is ramped to zero at $t = 1.4$ ns. At this moment f_o, q_o, and r_3 all align head on resulting in brief slowing of the rotation at $-120°$. Here, the dipole coupling opposes further magnetic reorientation because of the head-head magnetic alignment of the nano islands. Although this

dipolar interaction slows f_o's rotation, the ellipse's shape anisotropy overcomes this, resulting in continued motion and 180° reorientation.

Figures 6.3(a)-(b) show dynamic reorientation of the Ni and FeGa ASI lattices, respectively. As observed with CoFeB, the magnetization orientation of the non-nearest neighboring elements remains relatively unchanged following strain. The magnetization of f_o initially rotates clockwise at $t = 1.16$ ns for the Ni ASI and counterclockwise at $t = 1.10$ ns for the FeGa ASI. The magnetization rotation slows briefly at $t = 1.35$ ns and 1.29 ns for the Ni and FeGa ASI's, respectively. As with the CoFeB ASI, ballistic switching occurs and the momentary head-on alignment of f_o, q_o, and r_3 briefly slows rotation at $t = 1.35$ ns and 1.29 ns for the Ni and FeGa ASI's respectively. However, the rotation continues to -180° at t = 1.53 ns in Ni with 18° of overshoot while the FeGa magnetization rotates to 180° at $t = 1.46$ ns with 9° of overshoot. As observed in the CoFeB lattice, Figures 6.3(a)-(b) show that the magnetization of the nearest neighbor elements remains directed along their initial orientations even after f_o rotates 180o. For the Ni system, the largest deviations from equilibrium are exhibited by r_3 which varies between 66° and 54° during operation. For the FeGa ASI, q_3 experiences the largest shift in magnetic orientation and varies between 110° and 134° during the movement of the monopole. The magnetization rotation of f_o in both the Ni and FeGa ASI's is qualitatively similar to the CoFeB behavior. However, f_o's magnetization rotates 180° in 0.39 ns at 2.56 GHz for the Ni ASI while it takes 0.35 ns at 2.8 GHz for the FeGa. Similar to the CoFeB system, there is good agreement between the model's resonance and the 2.58 GHz predicted using Kittel's equation. However, the analytical prediction for FeGa of 3.9 GHz is 40% larger than the modeled resonance value. This difference is caused by the incoherent rotation present in the FeGa element's magnetization reorientation, as shown in the panel of Figure 6.3(b). This only occurs in FeGa elements because the demagnetization energy is much larger than either the CoFeB or Ni elements resulting in spatially non-uniform magnetization rotation. In addition to the comparison of ferromagnetic resonance frequencies, there are other subtle differences in the dynamics of the three lattices. For example, the FeGa system rotates counterclockwise which is caused by the non-deterministic switching present in precessional switching. Also, the FeGa magnetic

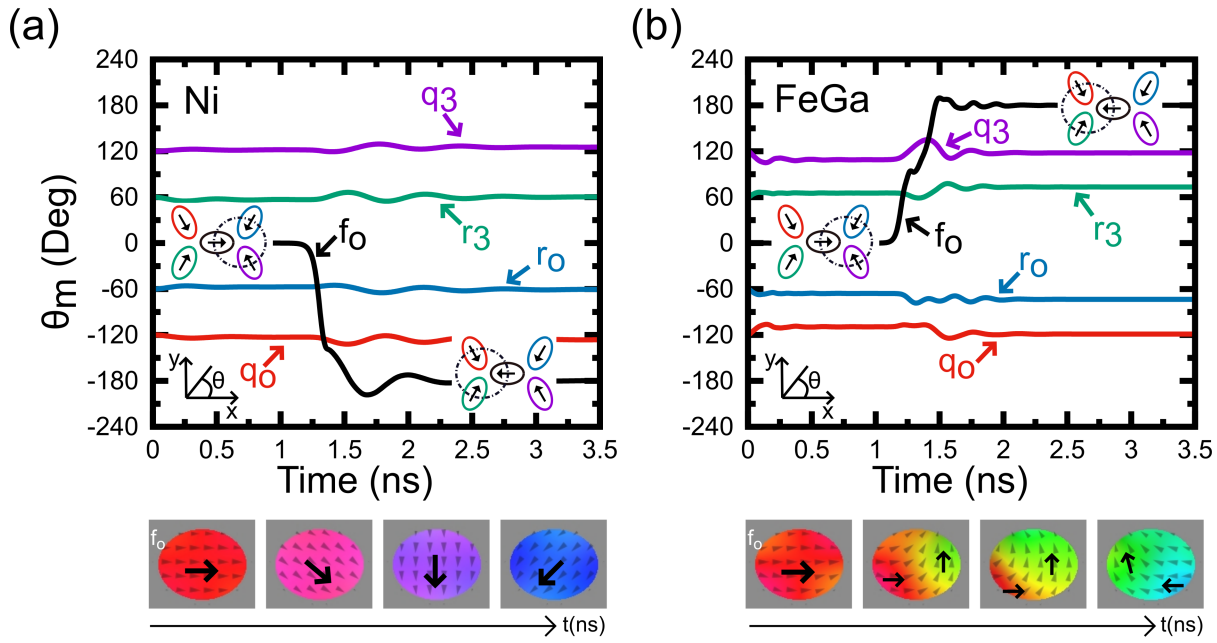

Figure 6.3: Time variation of x-component of magnetization for central magnetic island and nearest neighbors of (a) Ni ASI system and (b) FeGa ASI system. [41]

reorientation slows down at $\sim 95^\circ$ instead of 120° like CoFeB and Ni. This difference is attributed to the incoherent rotation of the FeGa system. Another difference is the decrease in overshoot angle and settling times of the Ni and FeGa systems when compared to the CoFeB ASI. This is caused by CoFeB's relatively smaller Gilbert damping coefficient compared Ni and FeGa.

An important observation of the three ASIs is that the flipping of the strained ellipse's moment perturbs the magnetization direction of the neighboring elements but does not cause them to reorient 180°. Consequently, strain-induced motion of the monopoles does not cause avalanche effects but gives the capability to deterministically place the ASI in specific magnetic configurations. This only lengthens or shortens the relevant Dirac string by one unit (i.e., one ellipse length) and does not nucleate new Dirac strings. As a result, such precise control is useful for ASI's with return point memory because individual limit cycles can be chosen by explicitly defining the initial state. Alternatively, the microwave properties of spin waves in reprogrammable crystals can be tuned using the control scheme. This is achieved by setting specific magnetic configurations of the ASI lattice which alter the spin wave modes of the crystal.

The amount of energy required to reorient the ASI nanodots can be approximated by evaluating the electrical energy delivered to the piezoelectric layer. For a 100 nm PMN-PT layer, 0.48 V, 0.48 V, and 0.72 V represent the voltages required for CoFeB, Ni, and FeGa respectively. The relative dielectric constant of PMN-PT is $\varepsilon = 5880$. Using these values, the amount of electrical energy delivered to the 100 nm x 30 nm electrodes in Figure 6.1 results in 275 aJ, 275 aJ, and 620 aJ to switch CoFeB, Ni and FeGa, respectively. Despite having larger magnetostrictive properties, the FeGa requires the largest energy to rotate the magnetic moment. This occurs because the ASI geometry is optimized for CoFeB rather than FeGa causing larger demagnetization effects in FeGa compared to the other material systems. Also, the FeGa is not isotropic since it contains an additional magnetocrystalline anisotropy (MCA) that is not included in either the CoFeB or Ni models. Additionally, the suboptimal geometry and MCA for FeGa cause incoherent magnetization rotation in contrast to Ni and CoFeB. Thus, these demagnetization and MCA effects represent additional energy barriers to overcome during precessional switching. Lastly, the energy estimates provided in this manuscript neglect substrate clamping effects, which can be substantial with improperly designed systems. However, this issue has been considered by other researchers (e.g., Ref [37]), suggesting values below 275 aJ are feasible if the system is properly designed.

Experimental implementation of the modeled system is possible with modern micro-fabrication techniques and measurement tools. Specifically, the ASI can be defined using electron beam lithography and local strain can be generated by applying voltage to the patterned electrodes of Figure 6.1. Device production, however is non-trivial and considerable attention must be paid to the layout of electrodes, interconnects, and testing interfaces. Simultaneous control of multiple monopoles is necessary for practical device implementation and, although difficult, it is possible with contemporary CMOS control systems/software.

6.4 Conclusion

In this section, a multiferroic artificial spin ice design was proposed for local magnetization control of magnetic monopoles. Strain-mediated monopole movement in a Kagome lattice ASI was demonstrated numerically for CoFeB, Ni, and FeGa systems with motion achieved through precessional magnetization switching near FMR. In contrast to contemporary stochastic control methods, the results demonstrate that ASI monopoles can be efficiently and locally controlled using a strain-mediated multiferroic approach. This demonstration provides a control methodology for future ASI based technologies requiring deterministic manipulation of monopole states.

6.5 Chapter References

[1] L. Pauling, "The Structure and Entropy of Ice and of Other Crystals with Some Randomness of Atomic Arrangement", Journal of the American Chemical Society **57**, 2680 (1935).

[2] J. E. Greedan, "Frustrated rare earth magnetism: Spin glasses, spin liquids and spin ices in pyrochlore oxides", Journal of Alloys and Compounds **408-412**, 444 (2006).

[3] B. C. den Hertog and M. J. P. Gingras, "Dipolar Interactions and Origin of Spin Ice in Ising Pyrochlore Magnets", (2000) 10.1103/PhysRevLett.84.3430.

[4] S. T. Bramwell and M. J. .-.-P. Gingras, "Spin Ice State in Frustrated Magnetic Pyrochlore Materials", **294**, 1495 (2002).

[5] T. Fennell, P. P. Deen, A. R. Wildes, K. Schmalzl, D. Prabhakaran, A. T. Boothroyd, R. J. Aldus, D. F. McMorrow, and S. T. Bramwell, "Magnetic Coulomb phase in the spin ice Ho2Ti2O7", Science **326**, 415 (2009).

[6] D. J. P. Morris, D. A. Tennant, S. A. Grigera, B. Klemke, C. Castelnovo, R. Moessner, C. Czternasty, M. Meissner, K. C. Rule, J.-U. Hoffmann, K. Kiefer, S. Gerischer, D. Slobinsky, and R. S. Perry, "Dirac Strings and Magnetic Monopoles in the Spin Ice Dy2Ti2O7", Science **326**, 411 (2009).

[7] L. D. C. Jaubert and P. C. W. Holdsworth, "Signature of magnetic monopole and Dirac string dynamics in spin ice", Nature Physics **5**, 258 (2009).

[8] C. Castelnovo, R. Moessner, and S. L. Sondhi, "Magnetic monopoles in spin ice", Nature **451**, 42 (2008).

[9] S. R. Giblin, S. T. Bramwell, P. C. W. Holdsworth, D. Prabhakaran, and I. Terry, "Creation and measurement of long-lived magnetic monopole currents in spin ice", Nature Physics **7**, 252 (2011).

[10] S. J. Blundell, “Monopoles, magnetricity, and the stray field from spin ice”, Physical Review Letters **108**, 1 (2012).

[11] S. T. Bramwell, S. R. Giblin, S. Calder, R. Aldus, D. Prabhakaran, and T. Fennell, “Measurement of the charge and current of magnetic monopoles in spin ice”, Nature **461**, 956 (2009).

[12] S. Zhang, “Tuning Geometries and Interactions of Artificial Frustrated Nanomagnets”, (2013).

[13] I. Gilbert, B. R. Ilic, B. Robert Ilic, and B. R. Ilic, “Exploring frustrated magnetism with artificial spin ice”, SPIE 9931, Spintronics IX, 99311P **9931**, 99311P (2016).

[14] K. K. Kohli, A. L. Balk, J. Li, S. Zhang, I. Gilbert, P. E. Lammert, V. H. Crespi, P. Schiffer, and N. Samarth, “Magneto-optical Kerr Effect Studies of Square Artificial Spin Ice”, Physical Review B **84**, 1 (2011).

[15] R. F. Wang, C. Nisoli, R. S. Freitas, J. Li, W. McConville, B. J. Cooley, M. S. Lund, N. Samarth, C. Leighton, V. H. Crespi, and P. Schiffer, “Artificial ‘spin ice’ in a geometrically frustrated lattice of nanoscale ferromagnetic islands”, Nature **439**, 303 (2006).

[16] C. Nisoli, R. Moessner, and P. Schiffer, “Colloquium: Artificial spin ice: Designing and imaging magnetic frustration”, Reviews of Modern Physics **85**, 1473 (2013).

[17] S. Ladak, D. E. Read, W. R. Branford, and L. F. Cohen, “Direct observation and control of magnetic monopole defects in an artificial spin-ice material”, New Journal of Physics **13**, 359 (2011).

[18] K. Zeissler, S. K. Walton, S. Ladak, D. E. Read, T. Tyliszczak, L. F. Cohen, and W. R. Branford, “The non-random walk of chiral magnetic charge carriers in artificial spin ice.”, Scientific Reports **3**, 1252 (2013).

[19] E. Mengotti, L. J. Heyderman, A. F. Rodríguez, F. Nolting, R. V. Hügli, and H.-B. Braun, "Real-space observation of emergent magnetic monopoles and associated Dirac strings in artificial kagome spin ice", Nature Physics **7**, 68 (2011).

[20] R. V. Hügli, G. Duff, B. O'Conchuir, E. Mengotti, L. J. Heyderman, A. F. Rodríguez, F. Nolting, and H. B. Braun, "Emergent magnetic monopoles, disorder, and avalanches in artificial kagome spin ice (invited)", Journal of Applied Physics **111** (2012) 10.1063/1.3670441.

[21] Y. Qi, T. Brintlinger, and J. Cumings, "Direct observation of the ice rule in an artificial kagome spin ice", Physical Review B - Condensed Matter and Materials Physics **77**, 1 (2008).

[22] G. Möller and R. Moessner, "Magnetic multipole analysis of kagome and artificial spin-ice dipolar arrays", Physical Review B - Condensed Matter and Materials Physics **80**, 2 (2009).

[23] Z. Budrikis, P. Politi, and R. L. Stamps, "Disorder regimes and equivalence of disorder types in artificial spin ice", Journal of Applied Physics **111**, 109 (2012).

[24] Z. Budrikis, J. P. Morgan, J. Akerman, A. Stein, P. Politi, S. Langridge, C. H. Marrows, and R. L. Stamps, "Disorder strength and field-driven ground state domain formation in artificial spin ice: Experiment, simulation, and theory", Physical Review Letters **109**, 1 (2012).

[25] G. W. Chern, C. Reichhardt, and C. J. Olson Reichhardt, "Avalanches and disorder-induced criticality in artificial spin ices", New Journal of Physics **16** (2014) 10.1088/1367-2630/16/6/063051.

[26] I. Gilbert, G.-W. Chern, B. Fore, Y. Lao, S. Zhang, C. Nisoli, and P. Schiffer, "Direct visualization of memory effects in artificial spin ice", Physical Review B **92**, 104417 (2015).

[27] A. Bur, T. Wu, J. Hockel, C. J. Hsu, H. K. Kim, T. K. Chung, K. Wong, K. L. Wang, and G. P. Carman, "Strain-induced magnetization change in patterned ferromagnetic nickel nanostructures", Journal of Applied Physics **109** (2011) 10.1063/1.3592344.

[28] C. Y. Liang, S. M. Keller, A. E. Sepulveda, W. Y. Sun, J. Cui, C. S. Lynch, and G. P. Carman, "Electrical control of a single magnetoelastic domain structure on a clamped piezoelectric thin film - Analysis", Journal of Applied Physics **116** (2014) 10.1063/1.4896549.

[29] C.-Y. Liang, S. M. Keller, A. E. Sepulveda, A. Bur, W.-Y. Sun, K. Wetzlar, and G. P. Carman, "Modeling of magnetoelastic nanostructures with a fully coupled mechanical-micromagnetic model", Nanotechnology **25**, 435701 (2014).

[30] J. Cui, C. Y. Liang, E. A. Paisley, A. Sepulveda, J. F. Ihlefeld, G. P. Carman, and C. S. Lynch, "Generation of localized strain in a thin film piezoelectric to control individual magnetoelectric heterostructures", Applied Physics Letters **107** (2015) 10.1063/1.4930071.

[31] J. Cui, J. L. Hockel, P. K. Nordeen, D. M. Pisani, C. Y. Liang, G. P. Carman, and C. S. Lynch, "A method to control magnetism in individual strain-mediated magnetoelectric islands", Applied Physics Letters **103** (2013) 10.1063/1.4838216.

[32] M. S. Fashami, K. Roy, J. Atulasimha, and S. Bandyopadhyay, "Magnetization dynamics, Bennett clocking and associated energy dissipation in multiferroic logic", Nanotechnology **22**, 155201 (2011).

[33] M. Salehi-Fashami, M. Al-Rashid, W.-Y. Sun, P. Nordeen, S. Bandyopadhyay, A. C. Chavez, G. P. Carman, and J. Atulasimha, "Binary information propagation in circular magnetic nanodot arrays using strain induced magnetic anisotropy", Nanotechnology **27**, 43LT01 (2016).

[34] Y. Shiota, T. Nozaki, F. Bonell, S. Murakami, T. Shinjo, and Y. Suzuki, "Induction of coherent magnetization switching in a few atomic layers of FeCo using voltage pulses", Nature Materials **11**, 39 (2011).

[35] R.-C. Peng, J.-M. Hu, K. Momeni, J.-J. Wang, L.-Q. Chen, and C.-W. Nan, "Fast 180° magnetization switching in a strain-mediated multiferroic heterostructure driven by a voltage", Scientific Reports **6**, 27561 (2016).

[36] X. Li, D. Carka, C. Y. Liang, A. E. Sepulveda, S. M. Keller, P. K. Amiri, G. P. Carman, and C. S. Lynch, "Strain-mediated 180° perpendicular magnetization switching of a single domain multiferroic structure", Journal of Applied Physics **118** (2015) 10.1063/1.4923350.

[37] Q. Wang, X. Li, C. Y. Liang, A. Barra, J. Domann, C. Lynch, A. Sepulveda, and G. Carman, "Strain-mediated 180 switching in CoFeB and Terfenol-D nanodots with perpendicular magnetic anisotropy", Applied Physics Letters **110**, 1 (2017).

[38] I. Gilbert, A. C. Chavez, D. T. Pierce, J. Unguris, W. Y. Sun, C. Y. Liang, and G. P. Carman, "Magnetic microscopy and simulation of strain-mediated control of magnetization in PMN-PT/Ni nanostructures", Applied Physics Letters **109** (2016) 10.1063/1.4965028.

[39] S. A. Wolf, J. Lu, M. R. Stan, E. Chen, and D. M. Treger, "The promise of nanomagnetics and spintronics for future logic and universal memory", Proceedings of the IEEE **98**, 2155 (2010).

[40] K. Y. Camsari, R. Faria, B. M. Sutton, and S. Datta, "Stochastic p-bits for invertible logic", Physical Review X **7**, 1 (2017).

[41] A. C. Chavez, A. Barra, and G. Carman, "Voltage control of magnetic monopoles in artificial spin ice", Journal of Physics D: Applied Physics (2018).

[42] C. Burrowes, N. Vernier, J. P. Adam, L. Herrera Diez, K. Garcia, I. Barisic, G. Agnus, S. Eimer, J. V. Kim, T. Devolder, A. Lamperti, R. Mantovan, B. Ockert, E. E. Fullerton, and D. Ravelosona, "Low depinning fields in Ta-CoFeB-MgO ultrathin films with perpendicular magnetic anisotropy", Applied Physics Letters **103** (2013) 10.1063/1.4826439.

[43] R. R. Basantkumar, B. J. Hills Stadler, W. P. Robbins, and E. M. Summers, "Integration of thin-film galfenol with MEMS cantilevers for magnetic actuation", IEEE Transactions on Magnetics **42**, 3102 (2006).

[44] A. E. Clark, M. Wun-Fogle, J. B. Restorff, and T. A. Lograsso, "Magnetostrictive Properties of Galfenol Alloys Under Compressive Stress", Materials Transactions **43**, 881 (2002).

[45] X. Liu, W. Zhang, M. J. Carter, and G. Xiao, "Ferromagnetic resonance and damping properties of CoFeB thin films as free layers in MgO-based magnetic tunnel junctions", Journal of Applied Physics **110** (2011) 10.1063/1.3615961.

[46] TRS-Inc., *PMN-PT31 Material Datasheet*, 2011.

7 Conclusion

In this work, voltage control of magnetism in nanoscale artificial multiferroic structures was demonstrated through numerical simulation and measurement. This efficient and precise control method was used to study the effects of strain on the magnetic states of both isolated and dipole-coupled nanostructures. The studies revealed interesting changes in magnetic states as well as unique coupling phenomena that have potential application for next-generation magnetic memory devices, nanomotors, and nanomanipulation.

In Chapter 2, the modeling techniques used for this dissertation were presented. First, the micromagnetic theory was developed by introducing the Landau-Lifshitz-Gilbert (LLG) equation which describes the dynamics of magnetic systems. Strain was included in this formulation using a uniaxial magnetic anisotropy and the LLG equation was solved using finite difference methods. Second, a method which couples the LLG equation with the elastodynamics and piezoelectric constitutive equations was outlined. Specifically, a weak formulation of the elastodynamics and LLG equations was derived forming a basis for a coupled model that solves the system of PDE's using an iterative finite element method.

In Chapter 3, a novel technique for imaging magnetic nanostructures was introduced and used to validate two numerical models. For this work, colleagues at the National Institute of Standards and Technology (NIST) used Scanning Electron Microscopy with Polarization Analysis (SEMPA) to image strain-induced changes of magnetization in submicron Ni disks. The SEMPA images showed strain-induced changes from vortex to antiparallel bi-domain states in 600 nm Ni disks. Additional measurements on 400 nm Ni disks showed 90° magnetization reorientation with applied strain. The measurements were compared to simulation results from the micromagnetics and fully-coupled formulations of Chapter 2. Both simulation qualitatively capture the response of the magnetization changes produced by the applied strain, with the coupled solution providing more accurate representation. The measurement and modeling techniques of this work are expected to be useful in the future design of strain-mediated

devices.

In Chapter 4, several designs for arrays of dipole coupled Ni nanodots were presented as a method to achieve voltage-induced transitions from artificial ferromagnetic to artificial antiferromagnetic states. The designs involved patterning Ni disks and ellipses on a ferroelectric PMN-PT substrate. Simulation results show that the dipole coupling produces artificial ferromagnetic (parallel magnetization alignment in the nanodot arrays) behavior that can be modified to artificial antiferromagnetic behavior with an applied voltage. The experimental data show the trends in remanence and coercivity predicted by the model, but discrepancies arise from geometric defects present in the fabricated samples. However, including these defects in the models, drastically improves the correlation between simulation and experiment. This demonstration provides a novel functionality of nanodot arrays and provides new insight of the role defects play in strain-mediated nanoscale devices. This understanding can lead to more effective control of magnetism with potential application for nanoscale motors or nanomanipulation.

In Chapter 5, full 360° deterministic magnetization switching was numerically demonstrated with a design that consists of three dipole-coupled magnetoelastic ellipses patterned on a piezoelectric substrate. This design requires only two pairs of simultaneously actuated electrodes thereby simplifying the complex electrical control schemes of other designs. Furthermore, the geometry used is much easier to fabricate than designs that require fewer electrodes. The device was simulated using both the purely micromagnetics and fully-coupled models. Importantly, switching was only achieved in the fully-coupled model. The discrepancy between the two modeling methods is caused by the strain gradients present in the system. Specifically, the micromagnetics model cannot account for these nonuniformities. This work demonstrated a novel method to achieve deterministic magnetization switching and showed the advantages of the fully-coupled model over the purely-micromagnetics simulation.

In Chapter 6, a new artificial spin ice (ASI) design using multiferroic materials was introduced,

thus providing energy-efficient, local lattice control of magnetic monopoles. The system was based on the hexagonal Kagome lattice and the design consisted of magnetoelastic ellipses patterned on a piezoelectric substrate. Specifically, strain-mediated monopole control was numerically demonstrated for CoFeB, Ni, and FeGa based systems. Motion of the magnetic monopole was achieved by precessional magnetization switching near FMR of the strained element. The strain-mediated monopole control scheme was shown to be energy efficient with switching energies less than 620 aJ. In contrast to contemporary stochastic control methods, the results show that strain can be used to efficiently and deterministically control ASI monopoles. This demonstration provides a foundation for future ASI based technologies requiring deterministic manipulation of monopole states.

To summarize, the results presented in this work show that low energy, precision control of magnetism is achievable using multiferroic heterostructures. By leveraging this capability, traditional nanostructures and materials can be combined in interesting ways to produce novel phenomena such as artificial magnetic phases or monopoles. Such results illustrate the power of the strain-mediated control method to provide innovative and complex functionality through the integration of simple multiferroic structures. Ultimately, these material systems show immense potential to provide disruptive technological solutions for problems in a wide range of disciplines.